Measurement of the Decay Constant

f_{D^+} at *BABAR*

A thesis submitted to The University of Manchester for the degree of

Ph.D.

in the Faculty of Engineering and the Physical Sciences.

2010

Graham Jackson

School of Physics and Astronomy

Contents

Total word count: 25819

List of Tables

List of Figures

Abstract

A value for the decay constant of the D^+ meson, f_{D^+}, is obtained by measuring the branching fraction $BF(D^+ \rightarrow \mu^+\nu)$ using $476\ fb^{-1}$ of data collected by the *BABAR* experiment at the SLAC National Accelerator Laboratory in the US. In order to measure $BF(D^+ \rightarrow \mu^+\nu)$, the decay chain: $D^{*+} \rightarrow D^+\pi^0$, $D^+ \rightarrow \mu^+\nu$ is reconstructed, where the four-momentum of the neutrino is estimated from the missing energy and missing momentum of an event. The results obtained for $BF(D^+ \rightarrow \mu^+\nu)$ and f_{D^+} are:

$$BF(D^+ \rightarrow \mu^+\nu) = (5.06 \pm 0.74 \pm 0.41) \times 10^{-4}$$

$$f_{D^+} = (237 \pm 18 \pm 19)\ MeV$$

where, for each result, the first error is statistical and the second is systematic.

Declaration

No portion of the work referred to in the thesis has been submitted in support of an application for another degree or qualification of this or any other university or other institute of learning.

Graham Jackson
School of Physics and Astronomy
The University of Manchester
Oxford Road
Manchester
M13 9PL
September 2010

Copyright

University Library's regulations (see http://www.manchester.ac.uk/library/aboutus/regulations) and in The University's policy on presentation of Theses

The Author

Between 1996 and 2002 the author attended West Denton High School (now All Saints College) and Newcastle College in Newcastle Upon Tyne. In 2002 he began to study physics at The University of Manchester, and in 2006 he was awarded a first class honours degree.

From 2006 to present the author has been a member of the Particle Physics Group at The University of Manchester and a member of the *BABAR* Collaboration, which is based at the SLAC National Accelerator Laboratory in the US. The author's supervisor is Prof. George Lafferty, and his advisor is Dr David Bailey.

Acknowledgements

I would like to thank my family for their support throughout my time in Manchester, both as an undergraduate and as a postgraduate. I would especially like to thank my mother for her love and generosity, and my sister for introducing me to The University of Manchester in the first place.

I would like to thank Fred Loebinger for his charismatic coffee time banter. Like so many other students, Fred was one of the main reasons that I chose to come and study in Manchester. I would especially like to thank George Lafferty for his advice, his patience, and for his sense of humour.

I thank all my friends and colleagues in Manchester and Palo Alto for helping to make my PhD a very enjoyable experience.

Finally, I would like to thank my girlfriend, Mariana, for being the most beautiful (and understanding) woman I've ever met. (And to think I wouldn't have met her at all if it weren't for Particle Physics!)

Dedication

To Guapa.

Chapter 1

Introduction

This thesis presents work that was carried out by the author at the University of Manchester in the UK and at the SLAC National Accelerator Laboratory (SLAC) in the US. SLAC was home to the *BABAR* experiment, which ran from October 1999 to April 2008, and recorded more than $500\ fb^{-1}$ of integrated luminosity. A pair of storage rings, called PEP-II, brought electrons and positrons into collision inside the *BABAR* detector at $\sqrt{s} \approx 10.58\ GeV$. The experiment was one of two so-called *B-factories*, the other being the BELLE facility at KEK in Japan. The B-factories were built primarily to produce $B\bar{B}$ events in order to study Charge Parity violation in the B meson system. However, the cross-sections for $c\bar{c}$ and $\tau^+\tau^-$ production were comparable to that of $b\bar{b}$, and so large numbers of charm mesons and tau leptons were also produced at *BABAR*.

The majority of the work documented in this thesis relates to the measurement of the decay constant of the D^+ meson, f_{D^+}. To obtain a value for f_{D^+}, the branching fraction for the decay $D^+ \to \mu^+\nu$ was measured using $476\ fb^{-1}$ of integrated luminosity.

The main motivation behind the analysis was to test a recent theoretical calculation for f_{D^+}, which was made using a Lattice QCD model. The same model predicted a value for $f_{D_s^+}$ which is 2.4 standard deviations away from the current Particle Data Group average. This deviation could be a sign that the model is incorrect; however it could also be consequence of physics beyond The Standard Model.

A measurement of the branching fraction for $D^+ \to \mu^+\nu$ provides a simple and clean means of obtaining a value for f_{D^+}. At present, the most precise experimental determination of f_{D^+} comes from the only measurement of $BF(D^+ \to \mu^+\nu)$ that is recognised by the Particle Data Group. Therefore, another strong motivation behind the analysis is to obtain a second viable measurement of $BF(D^+ \to \mu^+\nu)$.

To measure the branching fraction for $D^+ \to \mu^+\nu$, the decay chain $D^{*+} \to D^+\pi^0$, $D^+ \to \mu^+\nu$ was reconstructed, where the missing four-momentum of the event was used to estimate the four-momentum of the neutrino. Signal events were searched for using ΔM, which was defined as the mass difference of D^{*+} and D^+ candidates and peaked at around $140\ MeV/c^2$ for signal events. In order to measure $BF(D^+ \to \mu^+\nu)$, it was necessary to estimate the signal mode reconstruction efficiency and to do this two strategies were initially adopted. The first was to use a measurement of the inclusive D^{*+} production cross-section, which was carried out at CLEO at $\sqrt{s} \approx 10.6\ GeV$, as a basis for determining the absolute number of D^{*+} mesons produced at *BABAR*. The second method involved a normalisation mode, $D^+ \to \pi^+K^0_L$, with the aim of obtaining a relative branching fraction, i.e. $BF(D^+ \to \mu^+\nu)/BF(D^+ \to \pi^+K^0_L)$. The first strategy was the most straight forward, but the similar topology of the normalisation mode in the second strategy meant that a number of systematic uncertainties associated with candidate reconstruction would have canceled. Ultimately, the first method was chosen to estimate the signal mode reconstruction efficiency because the final distributions of ΔM for the normalisation mode indicated that there was a large difference in the reconstruction efficiency for $D^+ \to \pi^+K^0_L$ events between data and Monte Carlo. This difference was attributed to poor simulation of K^0_L interactions with the *BABAR* detector.

The thesis is divided into 7 chapters. In chapter 2, the D^+ meson decay constant is discussed, the theoretical background is described and previous measurements of $BF(D^+ \to \mu^+\nu)$ and f_{D^+} are summarised. Chapter 3 describes the subsystems of the *BABAR* detector in detail. Chapter 4 discusses event selection

work that was carried out by the author as part of an analysis which measured the decay constant of the D_s^+ meson. Apart from the overlapping experimental motivations (which are covered in chapter 2), chapter 4 may be regarded as standalone. The event selection and candidate reconstruction procedure that was performed as part of the f_{D^+} measurement is covered in chapter 5. The fit procedure that was used to obtain a final signal yield for the decay chain $D^{*+} \to D^+\pi^0$, $D^+ \to \mu^+\nu$ is described in chapter 6, and final results are calculated. The conclusions of the analysis are discussed in chapter 7.

Chapter 2

The D^+ Meson Decay Constant

2.1 Overview

The aim of the present analysis is to measure the *decay constant* of the D^+ meson, f_{D^+}, using the decay $D^+ \to \mu^+\nu$. (Charge conjugation is implied throughout this chapter, and subsequent chapters, unless otherwise stated.) Decay constants parameterise the overlap of quark wavefunctions within mesons [1]. A measurement of the branching fraction for the decay $D^+ \to \mu^+\nu$ provides a clean way of obtaining a value for f_{D^+}. Leptonic decays of other pseudoscalar mesons like π^+, K^+, D_s^+ and B^+ are also used as a means of finding their decay constants.

In the following sections of this chapter, the motivations behind the analysis are given, and the decay constant is described. A brief description of the weak interaction is given, and the dynamics of leptonic D^+ meson decay are discussed. The main motivations behind the analysis are reviewed in more detail, and previous experimental and theoretical measurements of f_{D^+} are described.

2.2 Motivation

Currently, the charm sector provides the only viable means of accessing decay constant information for heavy mesons. Leptonic decays of charged B mesons are yet to be measured in the $B^+ \to e^+\nu$ and $B^+ \to \mu^+\nu$ channels, and the $B^+ \to \tau^+\nu$ branching fraction measurement has a relative error of 28% [2]. Therefore, a

precise determination of the charged B meson decay constant, f_{B^+}, cannot be made experimentally, and so theoretical predictions for f_{B^+} must be relied upon. Theoretical predictions must also be relied upon for the B_s meson, as purely leptonic decay is virtually impossible due to the suppression of flavour changing neutral currents in the standard model. The same models that predict the decay constants for the B^+ and B_s mesons can also be used to predict the decay constants for charm mesons, like the D^+ and the D_s^+. The ability of these models to make charm sector predictions is important, because such predictions may be compared to the relatively precise experimental results that exist for the decay constants of charm mesons. Thus, the degree to which a model's B meson results may be trusted can be inferred by comparing that model's D meson results to their corresponding experimental values.

The main motivation behind the present analysis is to test the validity of a recent Lattice Quantum Chromodynamics (LQCD) calculation, which has been used to find a value for f_{D^+}. The same LQCD calculation has also been used to determine a value for the decay constant for the D_s^+ meson, $f_{D_s^+}$; however its result does not agree with the current experimental average for $f_{D_s^+}$. This disagreement could be an indication of new physics. Secondary motivations for the present analysis are discussed in sections 2.6, 2.7 and 2.8.

2.3 The Decay Constant

The decay constant of a pseudoscalar meson is a means of parameterising the overlap of the quark wavefunctions within the meson. Some examples of pseudoscalar mesons are B^+,D_s^+,D^+,K^+ and π^+. The following description of the decay constant is based on the example of leptonic pion decay given in references [3] and [4].

The Feynman diagram for the fully leptonic decay, $D^+ \to \mu^+\nu$, is shown in figure 2.1. Using this diagram the amplitude for the process, $\mathcal{M}$, can be found,

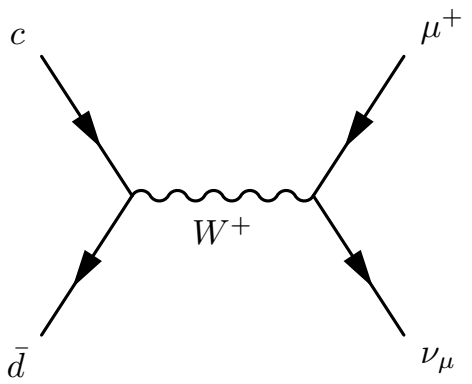

Figure 2.1: The annihilation diagram for the decay $D^+ \to \mu^+\nu_\mu$.

and is given in equation 2.1:

$$\mathcal{M} = \frac{g_w^2}{8(M_W c)^2} \left[\bar{u}\gamma_\mu(1-\gamma^5)v\right] F^\mu \tag{2.1}$$

Here, the term to the left of the square brackets involves the propagator term for the W boson and the weak coupling constant, g_w. It is the propagator term for the W boson that introduces the factor: $1/(M_W c)^2$, where M_W and c represent the mass of the W boson and the speed of light. The term in square brackets represents the leptonic current, where the spinor of the neutrino is represented by $\bar{u}$, and the spinor of the muon is given by v. The terms γ_μ and γ^5 represent the Dirac matrices. The term to the right of the square brackets parameterises the quark current. Naively, F^μ would be interpreted as $\bar{v}\gamma_\mu(1-\gamma^5)u$, where $\bar{v}$ and u would represent the spinors of the $\bar{d}$ and c quarks. However, this assumes that the quarks are free, rather than bound within the meson. The situation is complicated by gluon interactions between the quarks within the meson [5], and it is these strong interactions that the decay constant parameterizes.

Two assumptions lead to the usual interpretation of F^μ. Firstly, F^μ is assumed to be a contravariant four-vector, so that it can contract with the covariant four-vector, γ_μ, to make $\mathcal{M}$ a Lorentz invariant quantity. Secondly, F^μ must be related to the four-momentum of the D^+ meson. These assumptions lead to equation 2.2, where the appropriate CKM matrix element, V_{cd}, has been factored out of

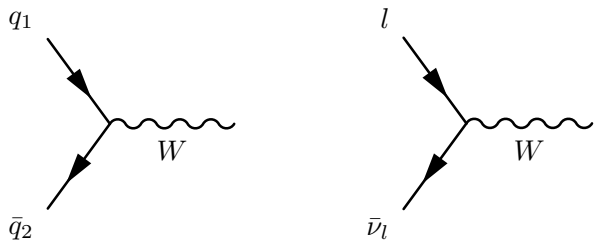

Figure 2.2: Feynman diagrams that show the vertices of charged weak interactions involving quarks (a) and leptons (b).

f_{D^+}, and the matrix element in full is given in 2.3:

$$F^{\mu} = V_{cd} f_{D^+} p^{\mu} \tag{2.2}$$

$$\mathcal{M} = \frac{g_w^2}{8(M_W c)^2} \left[\bar{u}\gamma_{\mu}(1-\gamma^5)v\right] V_{cd} f_{D^+} p^{\mu} \tag{2.3}$$

Calculating the matrix element leads to the formula for the decay rate of $D^+ \to \mu^+\nu$, Γ, which is given in equation 2.4 [2]:

$$\Gamma(D^+ \to \mu^+\nu_{\mu}) = \frac{G_F^2}{8\pi} f_{D^+}^2 m_{\mu^+}^2 M_{D^+} \left(1 - \frac{m_{\mu^+}^2}{M_{D^+}^2}\right)^2 |V_{cd}|^2 \tag{2.4}$$

Here, G_F is the Fermi constant, m_{μ^+} is the μ^+ mass and M_{D^+} is the D^+ mass. Equation 2.4 shows how a measurement of $\Gamma(D^+ \to \mu^+\nu_{\mu})$ can be used to obtain f_{D^+}, since the other quantities given, G_F, V_{cd}, and the masses of the particles involved, are all well known.

2.4 The Weak Interaction and the CKM Matrix

The decay $D^+ \to \mu^+\nu$ is the result of a charged weak interaction, mediated by a virtual W boson. The W boson can couple to both quarks and leptons, as shown in figure 2.2. Figure 2.2a shows how the W boson couples to two quarks, q_1 and $\bar{q}_2$, which may belong to different quark generations. Figure 2.2b shows how the W boson couples to a lepton, l, and a lepton anti-neutrino, $\bar{\nu}_l$, that are always of the same lepton generation. Put in terms of experimental observation, the lepton number is *always* conserved by the weak interaction, while the numbers

for strangeness, charm, beauty and truth are not.

To explain these cross-generational quark transitions, a matrix was proposed by Cabibbo, Kobayashi and Maskawa (CKM) in 1973 [6]. The matrix, V_{CKM}, operates on pure flavour eigenstates of the $down$-type quarks, d, s and b, as shown in equation 2.5. (This is just a convention; the up-type quarks could have been chosen instead.) After the operation, $d \rightarrow d'$, where d' is a linear combination of d, s and b.

$$\begin{pmatrix} d' \\ s' \\ b' \end{pmatrix} = V_{CKM} \begin{pmatrix} d \\ s \\ b \end{pmatrix} = \begin{pmatrix} V_{ud} & V_{us} & V_{ub} \\ V_{cd} & V_{cs} & V_{cb} \\ V_{td} & V_{ts} & V_{tb} \end{pmatrix} \begin{pmatrix} d \\ s \\ b \end{pmatrix} \tag{2.5}$$

The current experimental values of the CKM matrix elements are given in matrix 2.6 [7].

$$\begin{pmatrix} 0.974259(18) & 0.22543(77) & 0.00354(^{+16}_{-14}) \\ 0.22529(77) & 0.97342(^{+21}_{-19}) & 0.04128(^{+58}_{-129}) \\ 0.00858(^{+30}_{-34}) & 0.04054(^{+57}_{-129}) & 0.999141(^{+53}_{-24}) \end{pmatrix} \tag{2.6}$$

It is clear from the values in 2.6 that transitions within the same quark generation are heavily favoured. In the case of the D^+ meson, the c and $\bar{d}$ quarks are not of the same generation, and the decay $D^+ \rightarrow \mu^+\nu$ is said to be *Cabibbo suppressed*.

2.5 Dynamics of Leptonic D^+ Decay

The leptonic decay rates of the D^+ meson are subject to the effects of phase space suppression, helicity suppression and Cabibbo suppression.

The effect of phase space suppression on leptonic D^+ meson decay can be seen in the term: $(1 - m^2_{\mu^+}/M^2_{D^+})^2$, of equation 2.4. The more massive the daughter lepton, the more the phase space suppressed the decay rate is. In the case of the tau, the phase space suppression term is close to zero, since the tau mass is close to that of the D^+ meson. However, for the muon and electron, the term is very close to unity.

Leptonic D^+ decays are also helicity suppressed, which leads to the $m^2_{\mu^+}$ term in equation 2.4. Helicity suppression comes from the fact that the W boson couples to left-handed fermions and right handed anti-fermions, only. In $D^+ \to \mu^+\nu$ decay, this means that in order to retain the initial, spin-0, angular momentum of the D^+ meson, the muon must be produced in its unfavoured helicity state. (For a μ^+ this means left-handed and for a μ^- this means right-handed.) The helicity suppression terms for the decays $D^+ \to e^+\nu$ and $D^+ \to \mu^+\nu$ approach zero, whereas the term for $D^+ \to \tau^+\nu$ decay is close to unity.

The effects of helicity suppression can be negated if a real photon is emitted by the D^+ meson [2]. This would leave a virtual (spin-1) D^{*+} meson behind, which could then decay in the following manner: $D^{*+} \to \mu^+\nu_\mu$. Now, both the μ^+ and ν_μ must have the same helicity in order to conserve the initial unit of spin that came from the D^{*+}. The four lowest order real photon emission diagrams are shown in figure 2.3. Diagram 2.3d is ignored since it is suppressed by (m_c^2/m_W^2), where m_c^2 and m_W^2 are the masses of the charm quark and the W boson.

The contribution of real photon emission to the overall leptonic decay rate for a pseudoscalar meson strongly depends on the pseudoscalar meson involved. Indeed, the $B^+ \to \mu^+\nu_\mu\gamma$ decay rate is potentially larger than that of $B^+ \to \mu^+\nu_\mu$ [8, p332]. The B meson's greater mass leads to a larger amount of helicity suppression, which reduces the leptonic decay rate. This reduction allows the corresponding photonic mode to compete with the non-photonic, even though it itself is suppressed by α [9, p116]. For the present analysis the branching fraction for $D^+ \to \mu^+\nu_\mu\gamma$ is expected to be around two orders of magnitude below the SM expectation.

Using equation 2.4, the relative rates for D^+ meson decay to each of the lepton types are found to be: $(\tau : \mu : e) \approx (2.5 : 1 : 1 \times 10^{-5})$. These relative values are ultimately based upon the D^+ meson mass and that of the lepton involved. While the $D^+ \to \tau^+\nu$ channel does have the highest decay rate of the three leptonic channels, it is also the most difficult channel to reconstruct as it contains a tau lepton. The lifetime of the tau lepton is short and, unlike the muon and elec-

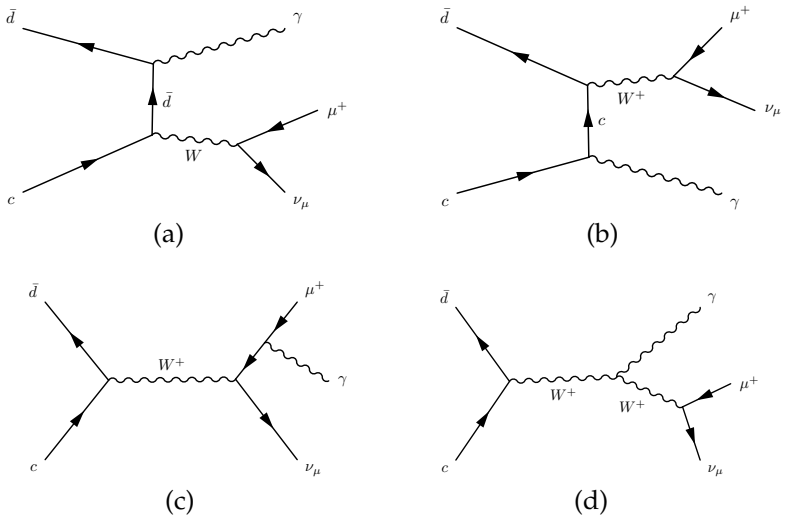

Figure 2.3: Feynman diagrams showing the four kinds of tree-level photon emission in $D^+ \to \mu^+\nu_\mu\gamma$ decay [10].

tron, its presence must be inferred from its decay products. Tau decays involve at least one neutrino, which would mean that each $D^+ \to \tau^+\nu$ reconstruction would contain a minimum of two neutrinos, making good quality signal candidate reconstruction difficult.

Cabibbo suppression has already been touched upon in section 2.4. Leptonic D^+ meson decay rates are an order of magnitude below the equivalent rates for D_s^+ decay because of Cabibbo suppression (using equation 2.6: $|V_{cd}/V_{cs}|^2 \approx 0.05$).

The result of these competing physical effects, coupled with the logistical requirements of reconstructing leptonic D^+ decays at *BABAR*, led to the choice of $D^+ \to \mu^+\nu$ as a means of determining f_{D^+}.

2.6 Lattice QCD

Quantum Chromodynamics is a theory that attempts to explain the strong force that governs the interactions between quarks and gluons. The strong interaction is characterised by a coupling constant α_s, which is a *running coupling* in the sense that the value of α_s is a function of the momentum transfer, q, between the particles involved in a scattering process. One possible definition of the relationship

between α_s and q is given in equation 2.7 [2]:

$$\alpha_s(q^2) = \frac{1}{b_0 ln(q^2/\Lambda^2)} \tag{2.7}$$

Here, the b_0 term is a number that depends on how many of the quark flavours have a mass far below q, and the Λ term is a constant of integration. From equation 2.7, it is clear that as the value of q increases, the α_s value decreases. This feature of QCD is known as *asymmtotic freedom*. More generally, for scattering processes with a high q, α_s can be calculated using a perturbative expansion in powers of $1/ln(q^2/\Lambda^2)$ [11]. However, for values of q that are close to the Λ scale (which is of the order of a few hundred MeV), the perturbative expansion approach breaks down, and an alternative way of calculating α_s is needed. One such alternative approach is to use LQCD, which has been used to study hadron masses and matrix elements. In LQCD, space and time are represented by a regular lattice of points in a four-dimensional *hypercube* [12]. In the hypercube each lattice point is a distance a away from each of the 8 nearest lattice points. Gluons are represented by *link variables* that transport colour between lattice points, and fermion fields are used to represent quarks at each lattice point.

Testing LQCD is important because it indirectly constrains the unitarity triangle by predicting matrix element values in the B system. The present analysis tests a LQCD calculation that predicts a value for the D^+ meson decay constant of $f_{D^+} = (207 \pm 4)\ MeV$ [13]. This result has a 2% relative error, which is a factor of four better than any previous experimental or theoretical value. The increase in precision is due to a reduction in the error caused by discretising the action of the charm quark on the lattice.

The prediction is in good agreement with the most recent experimental measurement, $f_{D^+} = (205.8 \pm 8.5 \pm 2.5)\ MeV$, which was carried out by CLEO-c [5] and is discussed in greater detail in section 2.9.1. While the relative error on this measurement is small at 4.3%, it is still twice the relative error on the LQCD calculation. In the CLEO-c analysis, their branching fraction measurement for the decay $D^+ \to \mu^+\nu$ was used in the calculation of f_{D^+}. They found

Quantity	LQCD based result	Experimental result
$f_{D^+}\ (MeV)$	207 ± 4	$205 \pm 8.5 \pm 2.5$ [5]
$f_{D_s^+}\ (MeV)$	241 ± 3	257.5 ± 6.1 [2]
$(f_{D_s^+}/f_{D^+})$	1.164 ± 0.011	1.257 ± 0.068 [2], [5]
V_{cs}/V_{cd}	$4.43 \pm 4 \pm 0.41$	4.45 ± 0.38 [2]
$M_{D^+}\ (MeV/c^2)$	1868 ± 7	1869.5 ± 0.4 [2]

Table 2.1: A comparison of the LCQD results [13] to the corresponding experimental values. The quantities and errors are described in the text.

$B(D^+ \to \mu^+\nu) = (3.82 \pm 0.32 \pm 0.09) \times 10^{-4}$, which is currently the only high precision $B(D^+ \to \mu^+\nu)$ measurement, and as a result, it is the only one recognised by the PDG. The branching fraction has been corrected by 1% to allow for the $\mu^+\nu_\mu\gamma$ final state, which is discussed in section 2.5. One of the main goals of the present analysis is to provide a second viable $D^+ \to \mu^+\nu$ measurement that has a relative error which is at least comparable to that of the CLEO-c result.

Table 2.1 summarizes the LQCD results that are relevant to this analysis and compares them to current experimental values [2]. Here, $f_{D_s^+}$ and f_{D^+} represent the decay constants of the D_s^+ and D^+ mesons, V_{cs} and V_{cd} are the CKM matrix elements, and the mass of the D^+ meson is M_{D^+}. In the LQCD column, the errors for all values except (V_{cs}/V_{cd}) combine both theoretical and statistical uncertainties. The errors on the ratio (V_{cs}/V_{cd}) are theoretical and experimental, and come from combining theoretical input - i.e. the calculated $f_{D_s^+}$ and $(f_{D_s^+}/f_{D^+})$ values - with experimental results from CLEO-c [14]. In the experimental results column, the errors for the D^+ meson decay constant are statistical followed by systematic, while those for $(f_{D_s^+}/f_{D^+})$ and the ratio of CKM matrix elements have been combined in quadrature. The $f_{D_s^+}$ and M_{D^+} experimental errors were taken from PDG averages.

2.7 Possible New Physics

The search for new physics is another motivation for the present analysis. The same LQCD calculation that was discussed in the previous section predicts a value for the decay constant of the D_s^+ meson of $f_{D_s^+} = (241 \pm 3)\ MeV$ [13],

which is 2.4σ below the experimental average of $f_{D_s^+} = (257.5 \pm 6.1)\ MeV$ [2]. (Note that in August 2010, updated results from this model were published, and the new $f_{D_s^+}$ value was found to be $f_{D_s^+} = (248 \pm 3)\ MeV$ [15].) This discrepancy could be the result of new physics.

One explanation of the discrepancy is provided by the Minimal Supersymmetric extension to the Standard Model (MSSM). In the MSSM, every standard model (SM) boson is linked to a supersymmetric (SUSY) fermion partner and every SM fermion is linked to a SUSY boson partner. The SUSY particles are thought to be very heavy, as they are yet to be observed in the laboratory. In the MSSM, the single SM Higgs doublet is replaced by two Higgs doublets, and the single SM scalar Higgs particle is replaced by five Higgs particles [16]. The five MSSM Higgs bosons comprise two that are charged, two that are neutral and even under CP, and one that is neutral and odd under CP. There are several different kinds of two-Higgs-Doublet model (2HDM), where the differences come from the allowed couplings of each doublet to quarks and leptons.

A particular 2HDM, known as *model II*, does allow the value for $f_{D_s^+}$ to deviate from its SM prediction [17]. In model-II, the up-type quark masses come from one of the Higgs doublets, while both the charged lepton masses and $down$-type quark masses come from the other Higgs doublet. In the model, the SM decay rate for $D_s^+ \to \mu^+\nu$ is multiplied by a factor, r_s, which is given by equation 2.8:

$$r_s = \left[1 - m_{D_s}^2 R^2 \left(\frac{m_s}{m_c + m_s}\right)\right]^2 \tag{2.8}$$

where $R = \tan\beta/m_{H^+}$, β represents the ratio of the two Higgs doublet vacuum expectation values and $m_{H^\pm}$ is the Higgs mass. In principle, the $D^+ \to \mu^+\nu$ branching fraction would be modified in an analogous way by r_d, but the effect would be negligible because $m_c >> m_d$ and therefore the $m_d/(m_c + m_d)$ term would be small. However, a measurement of the branching fraction ratio, R_μ, where $R_\mu = B(D_s^+ \to \mu^+\nu)/B(D^+ \to \mu^+\nu)$, could provide a more sensitive test of the effects of a possible charged Higgs [17]. This is because the relative error on the theoretical prediction for $(f_{D_s^+}/f_{D^+})$ is less than that of either $f_{D_s^+}$ or f_{D^+} [13].

Under the assumption of $m_s/(m_c + m_s) = 0.08$, a distribution of R_μ as a function of R is shown in figure 2.4 for three different $(f_{D_s^+}/f_{D^+})$ values.

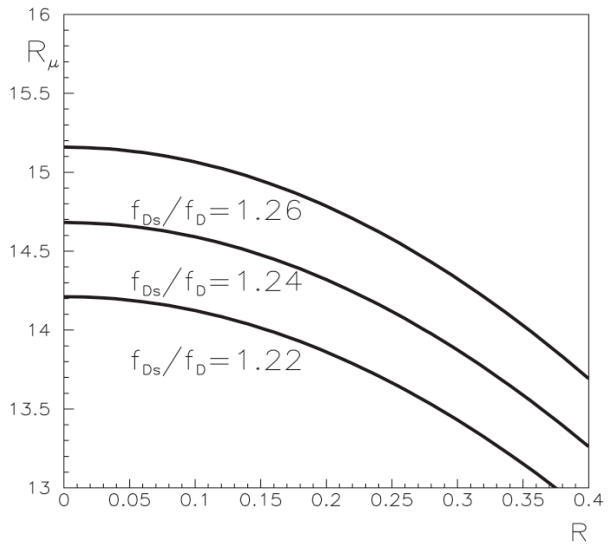

Figure 2.4: The expected variation of R_μ with respect to R for three different $(f_{D_s^+}/f_{D^+})$ values [17].

Figure 2.4 shows that an R value of around 0.4 would correspond to an R_μ value that was typically about 10% below the SM expectation. Such a decrease would be evident in the D_s^+ decay rate. However, this is not consistent with the current $f_{D_s^+}$ experimental average, which is 2.4σ *above* the LQCD prediction. If the experimental average for $f_{D_s^+}$ is taken to be accurate, then there could be several reasons as to why the measured value is higher, rather than lower, than the LQCD prediction. For example, the LQCD calculation might not be correct, or the proposed new physics introduced by the 2HDM might be either incorrect or its effect too small. There could also be a different kind of new physics affecting $D_s^+ \to \mu^+\nu$ decays.

Reference [18] suggests several *beyond the standard model* (BSM) charged particles that could mediate the decay $D_s^+ \to \mu^+\nu$. The amplitudes for such BSM processes would interfere with that of the SM process, and this would lead to a change in the observed $D_s^+ \to \mu^+\nu$ decay rate. The authors of [18] determined that the discrepancy between theory and experiment was not due to radiative corrections, finding the contribution of $D_s^+ \to \mu^+\nu\gamma$ to be $\approx 1\ \%$, a value supported

by reference [10]. Of the new particles suggested in [18], there are two that could explain the disagreement between the theoretical and experimental $f_{D_s^+}$ values [18]. One possibility, consistent with other experimental observations, is a charged Higgs with a mass below $0.5\ TeV$ as part of a 2HDM in which one doublet couples to the charged leptons and the u and c quarks, while the other doublet couples to the d, s, b and t quarks. The other possibility is a *leptoquark* with charge $-1/3$. Diagrams for each of these processes are shown in figure 2.5.

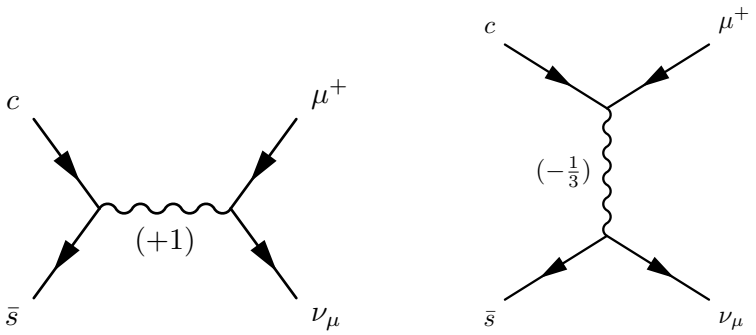

Figure 2.5: Feynman diagrams showing the possible contributions to $D_s^+ \to \mu^+\nu$ decay from new physics in the form of either a Higgs with charge $+1$ in (a) or a leptoquark of charge $-\frac{1}{3}$ in (b) [18].

2.8 Lepton Universality

The idea behind lepton universality is that the weak coupling constant, g_w, has the same value for all leptons. Lepton universality has been verified in several different ways [19]. For example, by comparing the nominal weak coupling constants of the τ^+ and the μ^+, g_τ and g_μ, using the decay modes $\tau^+ \to e^+\nu_e\bar{\nu}_\tau$ and $\mu^+ \to e^+\nu_e\bar{\nu}_\mu$, the fraction g_τ/g_μ can be found using equation 2.9:

$$\frac{g_\tau}{g_\mu} = B(\tau^+ \to e^+\nu_e\bar{\nu}_\tau)\left(\frac{m_\mu}{m_\tau}\right)^5\left(\frac{\tau_\mu}{\tau_\tau}\right) \tag{2.9}$$

Here, the masses of the τ^+ and the μ^+ are given by m_τ and m_μ, and their lifetimes by τ_τ and τ_μ. Inserting the nominal particle masses and lifetimes, and using the branching fraction for the decay $\tau^+ \to e^+\nu_e\bar{\nu}_\tau$ of $B(\tau^+ \to e^+\nu_e\bar{\nu}_\tau) = 0.1785$ [2], leads to the answer: $g_\tau/g_\mu = 1.001 \pm 0.004$. The weak coupling of the muon has also be compared to that of the electron, g_e, using the branching fractions for

$\tau^+ \to \mu^+\nu_\mu\bar{\nu}_\tau$ and $\tau^+ \to e^+\nu_e\bar{\nu}_\tau$. The fraction, g_μ/g_e, was found to be consistent with unity. Also, the values for the partial widths: $Z^0 \to e^+e^-$, $Z^0 \to \mu^+\mu^-$ and $Z^0 \to \tau^+\tau^-$ are all found to be the same, within experimental errors.

In the context of the present analysis, a measurement of $B(D^+ \to \mu^+\nu_\mu)$ could be combined with a measurement of $B(D^+ \to \tau^+\nu_\tau)$ in order to test lepton universality. Any deviation from the expected value for the ratio of branching fractions given in equation 2.10 would violate lepton universality and be a sign of new physics [20]:

$$\frac{B(D^+ \to \mu^+\nu_\nu)}{B(D^+ \to \tau^+\nu_\tau)} = \frac{m_\mu^2(1 - m_\mu^2/m_D^2)^2}{m_\tau^2(1 - m_\tau^2/m_D^2)^2} = 0.38 \tag{2.10}$$

Here, m_μ, m_τ and m_D are the μ^+, τ^+ and D^+ masses.

2.9 Summary of Previous Analyses

Theoretical predictions for f_{D^+} and the ratio $(f_{D_s^+}/f_{D^+})$ are given in figures 2.6a and 2.6b. The corresponding experimental values are also shown for comparison, where the PDG experimental average was used to obtain a value for $f_{D_s^+}$. In both figures, the initial lattice value (i.e. the top entry in each plot) came from the LQCD calculation that was discussed in section 2.6. The figures show how the values for f_{D^+} and $(f_{D_s^+}/f_{D^+})$ that were calculated using this model compare to the other theoretical calculations, and to the values obtained experimentally.

The most recent experimental measurements of the $D^+ \to \mu^+\nu$ decay rate come from analyses performed by two experiments, CLEO [5] and BES [31]. Each of their analysis methods will now be briefly described, along with a summary of their results.

2.9.1 The CLEO-c Analysis

The CLEO-c detector is located at Cornell University in the United States, and it records e^+e^- collision events that were created using the Cornell Electron-positron Storage Ring (CESR). A large fraction of CLEO-c's data has been recorded at a centre-of-mass (cm) energy equal to the mass of the $\psi(3770)$ res-

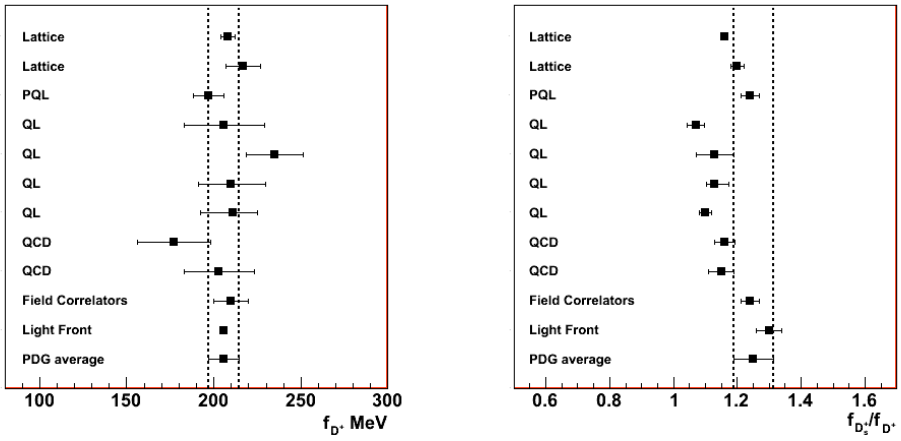

(a) (b)

Figure 2.6: Theoretical predictions for f_{D^+} (a) and the ratio $(f_{D_s^+}/f_{D^+})$ (b) from various sources. The order of the references corresponds to the top-to-bottom order of the points in both figures. The first lattice entry in each plot comes from the LQCD result discussed in section 2.6 [13]. The results of other calculation techniques (not discussed here) are shown for comparison; *quenched lattice* calculations are denoted QL, *partially-quenched* lattice calculations by PQL, and *sum rules* by SR [21–30]. Experimental averages for f_{D^+} and $(f_{D_s^+}/f_{D^+})$ are also given [2].

onance, which decays primarily to $D\bar{D}$. The beam energies of CESR are identical, and so the frame-of-reference of the centre-of-mass (cm) system that is produced in an e^+e^- collision is effectively the same as the laboratory frame-of-reference.

In the CLEO-c analysis, events were looked for in which a single muon candidate, consistent with a $D^+ \to \mu^+\nu$ decay, recoiled against a D^- tag candidate. The muon candidate had to have the opposite charge to the tag candidate. Candidate signal events were tagged in accordance with six D^- tag modes: $K^+\pi^-\pi^-(\pi^0)$, $K_S\pi^-(\pi^-\pi^+)$, $K_S\pi^-\pi^0$ and $K^+K^-\pi^-$. The energy of each tag candidate had to lie within a few tens of MeV of the nominal beam energy. The mass of each suitable tag candidate was then constrained using equation 2.11:

$$m_{BC} = \sqrt{E_{beam}^2 - \left(\sum_i \mathbf{p_i}\right)^2} \tag{2.11}$$

Here, m_{BC} is the beam-constrained mass, E_{beam} is the beam energy and $\mathbf{p_i}$ represents the momentum of the i^{th} final state particle of the tag candidate. This type of mass constraining procedure is analogous to the one used to constrain the

masses of B candidates at *BABAR*. Using this method, rather than using the invariant mass of the summed four-momenta of the tag candidate's daughters, resulted in an improved mass resolution for the tag candidate. This was because the beam energy was known to high precision. In total, over $400,000$ tag candidates were identified. Events that contained a K_S candidate, which was not part of the tag, or any additional charged tracks that had a point of origin which was close to the nominal interaction point were rejected. Events were rejected if they contained an isolated energy deposit, above $250\ MeV$, that looked like it came from a photon. They were also rejected if any neutral energy, which had not already been associated with the tag, was present. The angle, θ, made between the direction of the muon candidate and an axis parallel to the direction of the positron beam, had to satisfy $|cos(\theta)| < 0.9$. The signal variable used was missing-mass squared, MM^2, given by equation 2.12.

$$MM^2 = (E_{beam} - E_{\mu^+})^2 - (-\mathbf{p_{D^-}} - \mathbf{p}_{\mu^+})^{\mathbf{2}} \tag{2.12}$$

Here, $\mathbf{p_{D^-}}$ is the momentum of the tag D^-, and the energy and momentum of the signal candidate muon are given by E_{μ^+} and $\mathbf{p}_{\mu^+}$. The MM^2 distribution for the signal candidates is shown in figure 2.7. The number of $D^+ \rightarrow \mu^+\nu$ candidates was extracted from a fit to the MM^2 distribution and the branching fraction and D^+ meson decay constant values were found to be $B(D^+ \rightarrow \mu^+\nu) = (3.82 \pm 0.32 \pm 0.09) \times 10^{-4}$ and $f_{D^+} = (205.8 \pm 8.5 \pm 2.5)\ MeV$.

2.9.2 The BES Analysis

The Beijing Spectrometer (BES) is a detector housed at the Beijing Electron Positron Collider (BEPC) in China. The storage ring of BEPC brings electrons and positrons into collision within the BES detector. Like CESR, the beam energies of BEPC are identical, meaning that the net momentum of the particles produced in an e^+e^- collision is zero in the laboratory frame.

The BES analysis was performed at a cm energy equal to the mass of the

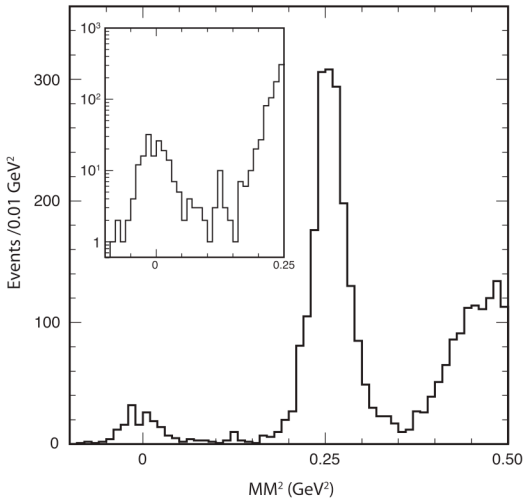

Figure 2.7: The MM^2 distribution for the signal candidates found in the CLEO-c analysis [5]. The majority of the events in the small peak, centred around $0\ MeV/c^2$, were taken to be from signal $D^+ \to \mu^+\nu$ decays. The large peak, centred around $0.25\ MeV/c^2$, came from $D^+ \to \pi^+ K_L^0$ decays, where the K_L had passed straight through the detector. The smaller plot shows the same distribution over a narrower mass range, and with a logarithmic y-axis.

$\psi(3770)$ resonance (i.e. $\sqrt{s} = 3.773\ GeV$), and using $33\ pb^{-1}$ of data, over 5000 D^- tag candidates were found by reconstructing the following nine decay modes: $\pi^+\pi^-\pi^-$, $K^+\pi^+\pi^-\pi^-\pi^-$, $K^+\pi^-\pi^-(\pi^0)$, $K^0\pi^-(\pi^-\pi^+)$, $K^0\pi^-\pi^0$, K^0K^- and $K^+K^-\pi^-$. The polar angle of the D^- tag candidate, θ_D, had to satisfy the condition $|cos(\theta_D)| < 0.8$.

Like in the CLEO analysis, a single charged track that recoiled against the tag D^- was looked for. The track had to be consistent with a muon hypothesis and have the opposite charge to that of the tag. The polar angle of the muon candidate, θ_μ, had to satisfy the condition $|cos(\theta_\mu)| < 0.68$. Candidates were vetoed if they contained additional photons.

The key variable in this analysis was U_{miss}, the difference between the missing energy and missing momentum of the candidate. Like MM^2 in the CLEO analysis, U_{miss} also peaked at zero for signal events. Monte Carlo (MC) studies led to two additional requirements for signal candidates. The momentum of the muon candidate (in the lab frame), P_μ, had to lie in the range $(0.785 < P_\mu < 1.135)\ GeV/c$. A window of $\pm 3\sigma_i$ was also applied to the U_{miss} value of each signal candidate. Here, σ_i is the standard deviation of the U_{miss} distribution for the

i^{th} kind of tag candidate, which was found using dedicated MC samples.

Figure 2.8 shows a two-dimensional plot of muon candidate momentum against U_{miss} that contains reconstructed signal candidates from data, and reconstructed background candidates from MC. After subtracting the estimated background contribution, 2.67 ± 1.74 signal event candidates were found based on their U_{miss} values and muon candidate momenta.

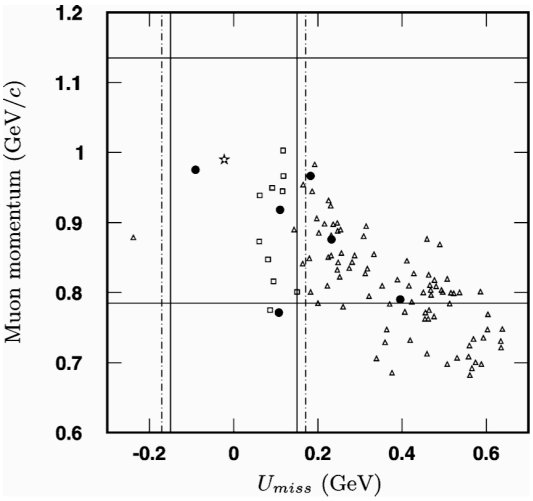

Figure 2.8: Data and MC $D^+ \to \mu^+\nu$ candidates for the BES analysis [31]. Signal candidates from only two of the tag modes survived to this stage. Candidates that came from the tag mode $D^- \to K^+\pi^-\pi^-$ are represented by black dots, and the solid vertical lines indicate their allowed U_{miss} window. Candidates that came from the tag mode $D^- \to K^+\pi^-\pi^-\pi^0$ are represented by stars, and the dashed vertical lines indicate their allowed U_{miss} window. The two solid horizontal lines show the muon candidate momentum cut. The squares and triangles represent background events that came from a of MC sample, which was much larger than the data sample used.

The BES analysis found the $D^+ \to \mu^+\nu$ branching fraction to be $B(D^+ \to \mu^+\nu_\mu) = (0.122^{+0.111}_{-0.053} \pm 0.010) \times 10^{-2}$, which translated into a D^+ meson decay constant of $f_{D+} = (371^{+129}_{-119} \pm 25)\ MeV$, where in each case the first (asymmetric) errors are statistical and the final error is systematic.

Chapter 3

The *BABAR* Detector

3.1 Introduction

The *BABAR* detector was built primarily to investigate charge-parity (CP) violation in neutral B meson decay. However, *BABAR* was also capable of precision studies of the decay modes of other bottom mesons, charm mesons and τ leptons. The detector was housed at the SLAC National Accelerator Laboratory in California. Particle collisions were provided by the storage rings of PEP-II which, during normal operation, circulated a $9.0\ GeV$ electron beam clockwise and a $3.1\ GeV$ positron beam counter-clockwise. The asymmetric energies of the beams meant that the centre-of-mass (cm) system was Lorentz boosted in the lab frame. Table 3.1 shows typical production cross-sections for fermion pairs ($f\bar{f}$) at *BABAR* [32].

Over $500 fb^{-1}$ of integrated luminosity (L) was recorded during the lifetime of *BABAR*. The total number of $f\bar{f}$ events is given by the product σL. For example,

e^+e^-	Cross-section, σ (nb)
$b\bar{b}$	1.05
$c\bar{c}$	1.30
$s\bar{s}$	0.35
$u\bar{u}$	1.39
$d\bar{d}$	0.35
$\tau^+\tau^-$	0.94

Table 3.1: Typical production cross-sections for fermion pairs, in nanobarns, at *BABAR*

.

there were around 700 million $c\bar{c}$ events. With typical $f\bar{f}$ datasets of hundreds of millions of events, branching ratios as low as $\approx 1 \times 10^{-7}$ could, in principle, be measured.

BABAR had to be able to make precise measurements of the position, momentum and energy of the decay products of hadrons and leptons. These requirements dictated many of the design features of *BABAR*'s subsystems. The solid angle of *BABAR* had to be as large as possible and the gaps and inactive regions between the detector and the beam pipe had to be minimized. Photons with as little energy as a few tens of MeV had to be detected with high efficiency. Efficient detection of charged particles with momenta below $\approx 100\ MeV/c$ was also needed, as were accurate particle identification and low mis-identification rates. Robust electronics components had to be able to cope with prolonged radiation exposure, and reliable data acquisition systems, capable of high readout rates, were essential.

The following sections of this chapter introduce the *BABAR* detector in more detail. After an initial overview, *BABAR*'s electronics and computing support are described, as are the PEP-II storage rings, the radiation monitoring systems and the solenoid magnet. The major subsystems of the detector are then discussed in detail, with emphasis on how they worked together to achieve high precision measurements. Unless otherwise stated, all numerical values mentioned in the following sections come from reference [33].

3.2 Detector Outline

Lateral and longitudinal cross-sections of the detector design are shown in figures 3.1 and 3.2. The interaction point (IP) was offset by $370\ mm$, along the z-axis, in the laboratory frame. The shift was in the direction of the low energy positron beam and ensured that the detector acceptance was as large as possible for the moving cm frame. A $1.5\ T$ superconducting solenoid effectively divided the detector into inner and outer sections, where the inner detector held four of the five *BABAR* subsystems. Closest to the beam line was the silicon vertex tracker

(SVT), then came the drift chamber (DCH) and the detector of internally radiated Cerenkov light (DIRC). Finally, the electromagnetic calorimeter (EMC) completed the inner detector. The remaining subsystem, located in the outer layer was the integrated flux return (IFR).

Relative to the beam line, the angular coverage began at $0.35\ rad$ from the forward direction and ended at $(0.4\ rad)$ from the backward direction. The magnets near to the IP (B1 and Q1 on figure 3.2) limited the possible angular coverage of the detector.

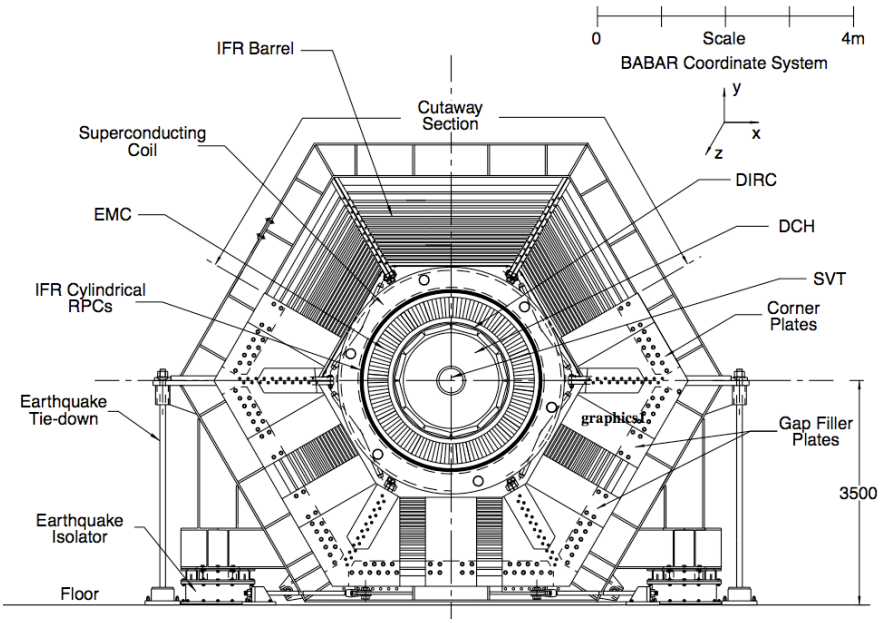

Figure 3.1: Lateral cross-section schematic of the *BABAR* detector, showing the various subsystems [33].

3.2.1 Computing, Data Acquisition, Trigger and Electronics

The trigger and data acquisition (DAQ) systems of *BABAR* formed only part of a larger electronics and computing infrastructure. A brief overview of these systems, and how they were connected to one another, is given below.

Electronics

Common to all of the *BABAR* subsystems, the *front-end-electronics* (FEE) layout is shown in figure 3.3. Attached to the detector itself, the FEE were connected to

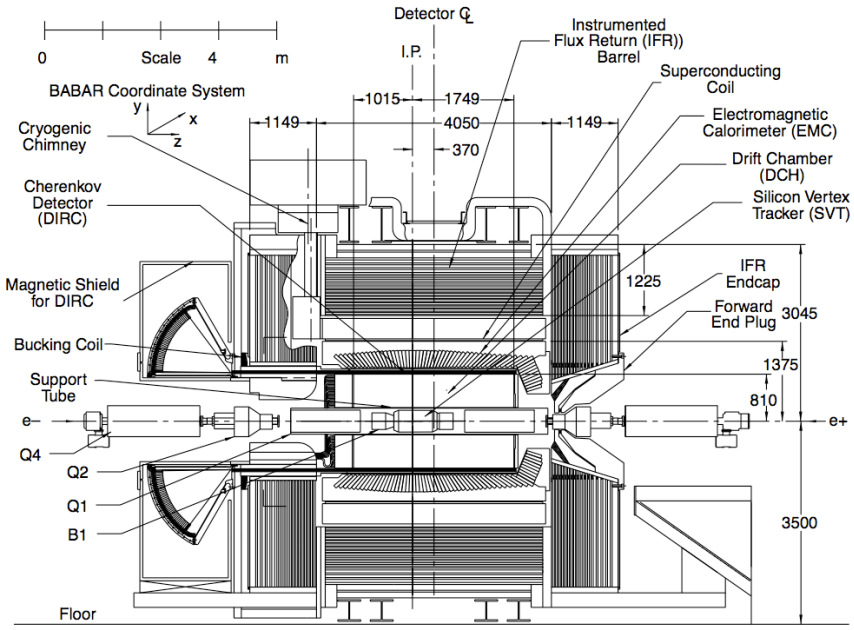

Figure 3.2: Longitudinal cross-section schematic of *BABAR* . All dimension are in millimeters [33].

their respective subsystems via short cables. After amplification and digitization, the signal was sent to the level 1 trigger where it was held in a buffer pending a level 1 trigger accept, before being passed to the event buffer, which was later read by the DAQ system.

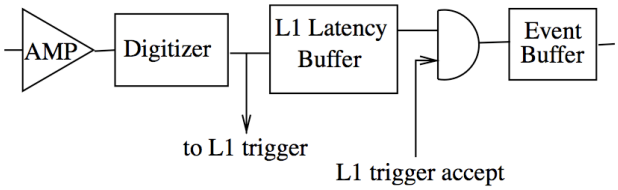

Figure 3.3: Schematic of the front-end-electronics components. Analogue signals entered from the left and, if after digitization they satisfied the L1 trigger, they were stored in the event buffer [33].

Triggers

The two main triggers of *BABAR* were the level 1 (L1) and the level 3 (L3). The L1 trigger used information from the DCH, EMC and DIRC and was designed to remove beam backgrounds and assess crude detector input. The event rate after L1 was below $2\ kHz$. After an event collision, the L1 buffer had a $12\ \mu s$ timing

window, before passing accepted events on to the L3 trigger. The event rate for L3 selection and storage was around an order of magnitude below that of L1 due to processing capabilities and the disk space available.

Computing and the DAQ System

The processing of raw data through the DAQ and on-line computing systems is shown in figure 3.4. There were several elements to the DAQ computing hardware; as well as a farm of Unix machines, there was an Ethernet network, VME crates, read-out modules (ROMs) and a fast control and timing system (FCTS) that controlled the flow of data. Fibre optic cables allowed the ROMs and the FEE to communicate with each other.

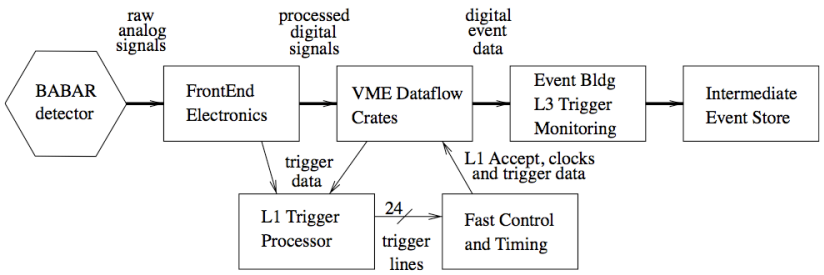

Figure 3.4: Flow chart showing the flow of data from the detector to the temporary event store [33].

On-line software and processing

With the aim of minimizing the dead time, the *on-line data flow* (ODF) software was responsible for coordinating the DAQ throughput. ODF output was passed on to *on-line event processing* (OEP) and after some quality assurance tests and applying the L3 trigger software, the OEP wrote the output to temporary storage. Events written by the OEP underwent a complete reconstruction as part of the *on-line prompt reconstruction* OPR. As well as performing 'rolling' calibrations (i.e. calibrations were performed, and their results were applied to the next set of recorded data), OPR also selected physics events. The OPR output was written to the event store, where it was ready for use in physics analyses.

On-line run control (ORC) provided the user with a simple interface to control the detector, and *on-line detector control* (ODC) monitored the detector environment and electronics.

3.2.2 PEP-II

PEP-II provided the collisions for *BABAR* by producing a centre of mass energy equal to the mass of the $\Upsilon(4S)$ resonance ($10.58\ GeV$) using a $9.0\ GeV$ electron beam that collided head-on with a $3.1\ GeV$ positron beam. To estimate the continuum contribution below the $\Upsilon(4S)$ peak, around 10% of data was recorded at an energy $40\ MeV$ below the resonance energy.

Overview

Bunch crossings occurred every few nanoseconds in PEP-II or, alternatively, there were roughly four bunches every five metres. The number of bunches used, combined with the high beam currents, produced the high instantaneous luminosity needed.

Beam separation after a crossing was achieved using a series of dipole and quadrupole magnets, a schematic for which is shown in figure 3.5. Post-collision, the beams were horizontally parted by the B1 dipoles, then the Q1 quadrupoles focussed the low energy beam in the vertical plane and defocussed it in the horizontal plane. Further focussing of the beams was achieved using the magnets Q2, Q4 and Q5. A deliberate $20\ mrad$ offset of the beam line from the z-axis helped to mitigate the effect of the solenoid on the beams.

The beam pipe containing the IR had two layers, between which water was used as a coolant. At the outer radius, the beam pipe diameter ($55.8\ mm$) contributed just over one radiation length to a particle traveling along a radial trajectory from the IP.

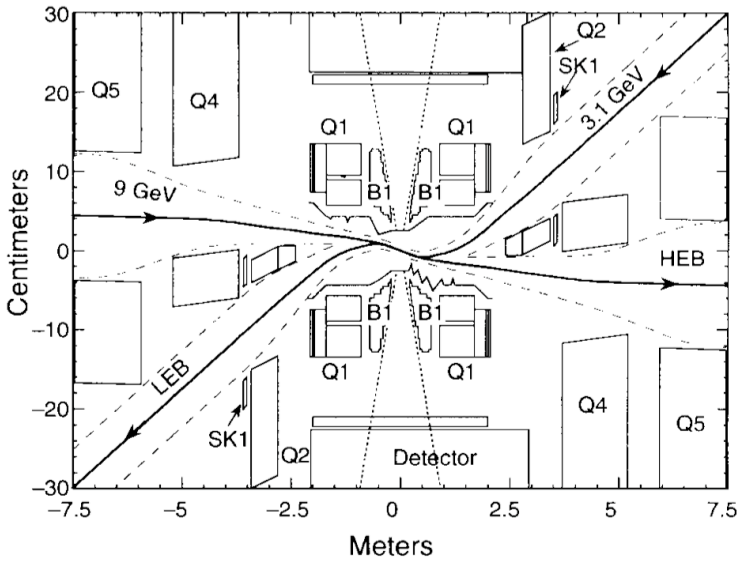

Figure 3.5: A drawing of the magnet arrangement near the IR. Note the relative scales on the horizontal and vertical axes [34]

PEP-II beam parameters

As well as the beam energies and the instantaneous luminosity, the size, position and angle of the beam-spot were monitored. Simple QED events ($e^+e^- \to e^+e^-$ or $e^+e^- \to \mu^+\mu^-$) were used to determine the absolute beam luminosity and direction. The mean frequency deviations of the accelerating electric fields from their nominal values and the total bending strength of the magnets were used to find the beam energies.

Beam backgrounds

There were two main sources of beam background, with the worst being beam-beam interactions. Here, electrons and/or positrons interacted with detector material after having undergone Bhabha scattering, resulting in unwanted electromagnetic showers which were especially problematic for the DIRC. The next largest background came from the beam scattering off what few gas particles remained in the beam pipe, causing coulomb scattering and bremsstrahlung. This background was present in all subsystems and was especially damaging to the SVT.

Beam backgrounds effectively reduced the lifetime of the experiment by dam-

aging the detector subsystems and their FEE. DAQ efficiency was affected by spikes in background that overloaded the bandwidth of the system.

3.2.3 The Solenoid Magnet and Steel Flux Return

The $1.5\ T$ magnetic field provided by the solenoid magnet was augmented by an $870\ tonne$ steel flux return. The magnetic field was important for measuring charged particle momenta, while the flux return aided the identification of muons and also some types of hadron.

The magnetic field produced by the solenoid created potential problems for the flux return. The end door sections of the flux return had to be able to cope with the mechanical stresses produced by the magnetic field. The lack of symmetry between the flux return's forward and backward ends was another source of magnetic stress.

3.3 The Silicon Vertex Tracker

3.3.1 Introduction

The SVT was the innermost layer of the *BABAR* detector and worked alongside the DCH to measure particle momenta and angles. The decay vertices of B mesons, D mesons, and τ leptons were all located close to the IR, which made pairs of vertices difficult to separate. The decays of such particles commonly involved hadrons that were unstable, like the J/ψ, the λ and the ρ. These daughter particles introduced another set of vertices that needed to be resolved.

One of the main goals of the SVT, DCH and DIRC subsystems was to make precise position measurements of decay vertices. In order to make such measurements, high quality reconstructions of the trajectories of the particles involved were required. As the particles traversed the detector, their trajectories were affected by multiple scattering. To minimise the amount of multiple scattering, the SVT, DCH and DIRC subsystems were situated as near to the beam-line as possible.

DCH measurements were more important for low momentum particles, although those tracks with very low momentum (below $\approx 120\ MeV/c$) did not reach the DCH, and so only SVT information was available. A good example of this is the slow pion, π_s^+, coming from the excited D^{*+} decay: $D^{*+} \to D^0\pi_s^+$.

3.3.2 Design

Precision vertex-fitting was a major design consideration for the SVT. The measurement of quantities like the time dependent CP asymmetry present in B decays, required a resolution in z of better than around $90\ \mu m$ [35], while in the $x-y$ plane, a resolution of the order $100\ \mu m$ was needed to resolve a pair of vertices. To achieve such high precision measurements, the SVT had to be as close to the PEP-II interaction region (IR) as possible, meaning that it had to be radiation hard to survive for the duration of the experiment. Robust components were also needed to ensure reliability, because during normal running conditions, the SVT was not accessible.

To satisfy the above requirements, an SVT consisting of five layers of double-sided silicon strip detectors was chosen.

3.3.3 Layout

The three inner SVT layers were made up of 6 silicon strip modules each, and the fourth and fifth layers consisted of 16 and 18 modules respectively. While the strips on one side of each layer were aligned along the beam axis, those on the opposite side were at 90° to it, allowing both z and ϕ in cylindrical co-ordinates to be measured. Complete ϕ angular coverage was achieved by allowing the modules to overlap slightly. Figures 3.6 and 3.7 show longitudinal and lateral cross-sections of the SVT.

The layers were labeled 1 to 5, with layer 1 being the innermost. Layers 1 to 3 ran parallel to the beam line while layers 4 and 5 were angled at the edges, meaning that the same angular coverage could be achieved using less silicon.

For electronics readout, each module was divided in two, with half of the

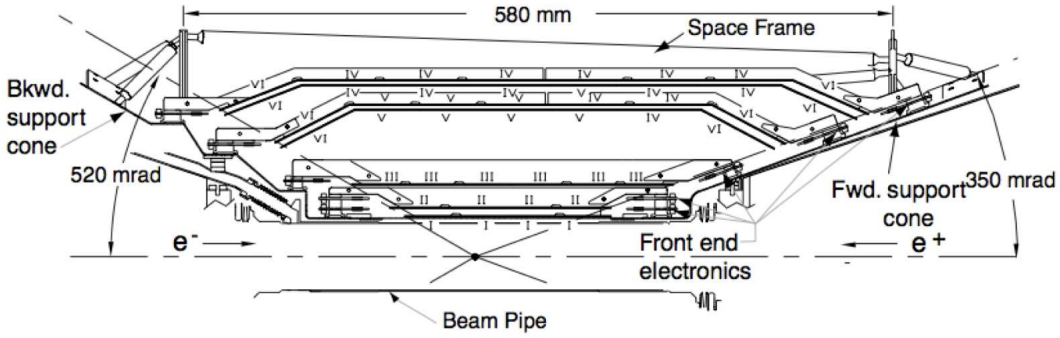

Figure 3.6: Longitudinal cross-section of the SVT. The relative position of the SVT, the support cones (described in the text) and the IP can be seen [33].

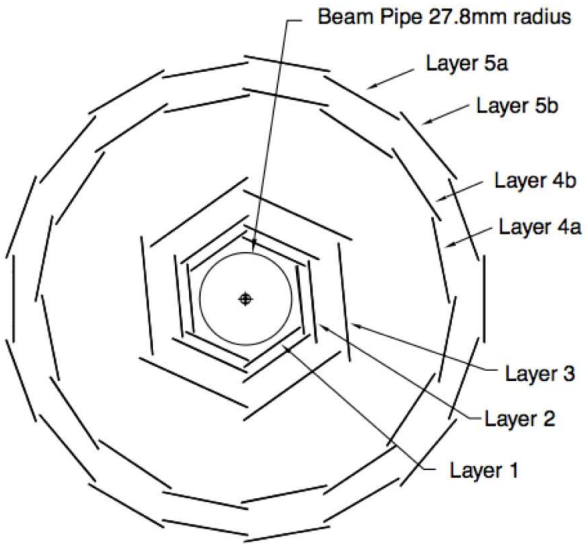

Figure 3.7: Lateral cross-section of the SVT showing the position of each of the five layers in relation to the beam pipe [33].

readings going to each end of the SVT. The readout electronics and associated data cables can be seen toward the edges of the photograph of the SVT shown in figure 3.8. By locating the electronics at the ends of the SVT, the amount of material inside the active region of the detector was kept to a minimum.

The SVT was held in place by forward and backward support cones (see figure 3.6) and the dipoles of the B1 magnets located within the support cones defined an axis upon which the SVT was aligned. The SVT was housed inside a support tube that ran the length of the detector and was connected to the PEP-II support structure in order to maintain the SVT's relative position with respect to the IR.

Overall, the active area of the SVT was about $1\ m^2$ and the acceptance in solid

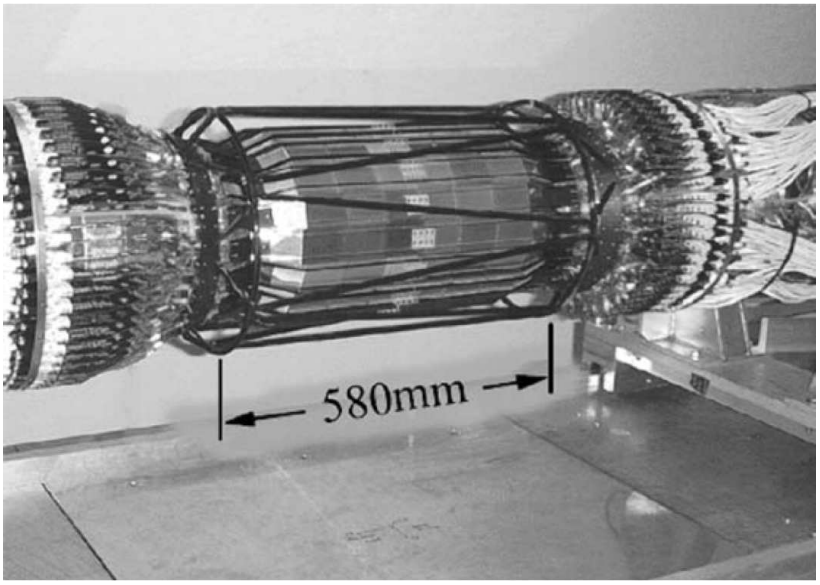

Figure 3.8: A Photo of the assembled SVT. The outer layer of silicon strips can be seen, as can some of the associated readout electronics [33].

angle of the cm frame was 90%. The SVT's polar angle coverage began at 20° from the beam axis in the forward region, and extended to 150°.

3.3.4 Components

The four main components of the SVT were the silicon strip sensors, fanout circuits, the FEE and the data transmission system. The sensors of the SVT were made from double sided silicon. Each sensor consisted of a central n-type substrate that was sandwiched between two strips, one p-type and the other n-type. The depletion voltage for a strip was typically around $30\ V$ and to make the strips radiation hard, resistors were added to both sides. The fanout circuits linked the silicon strips to the FEE and were designed to have a low capacitance and resistance.

3.3.5 Monitoring, Calibration and Alignment

The SVT required constant monitoring of environmental conditions (i.e. temperature and humidity) and radiation damage. The position of the SVT with respect to the B1 magnets was monitored as was that of the support tube to the DCH.

Clean $e^+e^- \to e^+e^-$ and $e^+e^- \to \mu^+\mu^-$ events were used to obtain a mean IP position, which provided a reference point to track relative movements of the SVT.

During downtime (when no beams were circulating in PEP-II), the channels of the SVT were calibrated using test pulses from a set of capacitors. The calibration involved measuring the gain settings and electronic noise for each channel, it also provided a means of finding defective channels.

There were two types of SVT alignment, one global and one local. Local alignment of the SVT's sensors was performed first, using mainly cosmic rays and $e^+e^- \to \mu^+\mu^-$ events. Hits from tracks were combined with optical survey data (taken during the assembly of the SVT) to calculate the local position of the sensors. After local alignment, the SVT was considered to be a rigid object.

The DCH provided the co-ordinate system for global alignment where the relative position of the SVT was updated run-by-run (i.e. every few hours). Suitable tracks were fitted twice; once using only SVT information and once using only DCH information. The relative position and orientation of the SVT within the DCH could then be determined by minimizing the corresponding SVT and DCH parameters. After the alignment parameters for a given run were determined, they could be used as part of the track reconstruction in the following run. Figure 3.9 (a) shows how the relative vertical position of the SVT changed over several hundred days, and figure 3.9 (b) shows the change over a ten day period. Discontinuities in 3.9 (a) were the result of detector access and maintenance. The need for frequent global calibrations, due to day/night temperature fluctuations is apparent.

3.3.6 Analysis of Data and Performance

Using hit information gathered from several strips, space points indicating track trajectories could be inferred. The typical hit occupancy of the three inner (two outer) layers of the SVT, during a $1\ \mu s$ window was about $3\ \%$ ($1\ \%$), although this depended upon the number of beam-induced background tracks.

Reconstruction began with the removal of any channels that were out-of-time

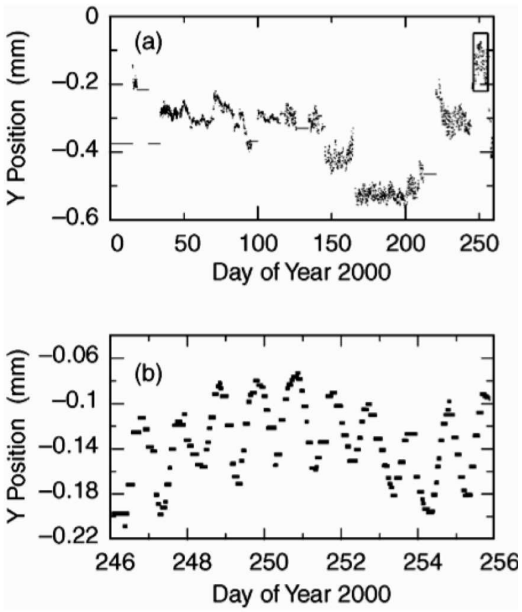

Figure 3.9: The SVT's vertical position shown for a year (a) and over a 10 day period (b) [33].

in accordance with a predefined timing window that was centred on the event time. A cluster-finding algorithm then acted upon the remaining hits, forming clusters by grouping strips containing similar hit times with each other.

Figure 3.10 [33, p42] shows the hit reconstruction efficiency, as a function of half-module number, which was usually greater than $95\ \%$. Figure 3.11 [33, p43] shows the hit resolution, in μm, of the SVT layers as a function of the track entry angle made with respect to the z-axis (a) and ϕ (b). The hit resolution was the distance between the hit location and the point at which the track broke the plane of the sensor.

The measured pulse height of a hit in the SVT was converted into an energy loss measurement, i.e. a dE/dx value. Each SVT layer could make a maximum of ten dE/dx measurements for a track. Using dE/dx measurements, a 2σ separation of kaon tracks from those of pions could be achieved up to a momentum of $500\ MeV/c$, with a similar quality of separation between kaons and protons for tracks above $1\ GeV/c$.

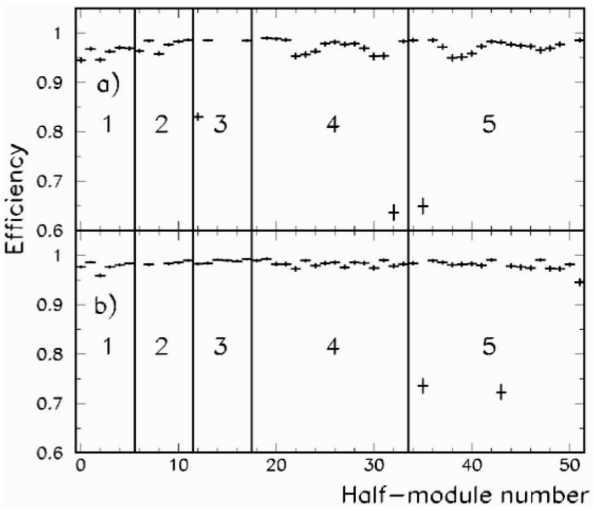

Figure 3.10: Efficiency for reconstructing $e^+e^- \rightarrow \mu^+\mu^-$ events in the forward (a) and backward (b) half-modules of each SVT layer [33].

3.4 Drift Chamber

3.4.1 Overview

The DCH partnered the SVT in charged particle tracking and was designed to measure angles and momenta with high precision, and in the presence of high beam backgrounds. The DCH was frequently the only source of information for the decay of certain types of particle. A prime example was that of K_S^0 decay, as a K_S^0 could travel beyond the layers of the SVT before decaying. A key aspect of the DCH was its ability to differentiate kaon tracks from those of pions. Through measuring the ionization energy loss of a track, the DCH provided K/π separation up to $700\ MeV/c$ with $7\ \%$ resolution. Figure 3.12 shows a schematic of the DCH longitudinal cross-section. The IP was located towards the backward end of the detector in order to reduce the number of particles lost down the beam pipe due to the forward Lorentz boost. The angles, $17.2°$ and $27.4°$, show the respective forward and backward limits for which a particle would have passed through at least half of the layers of the DCH [33, p44].

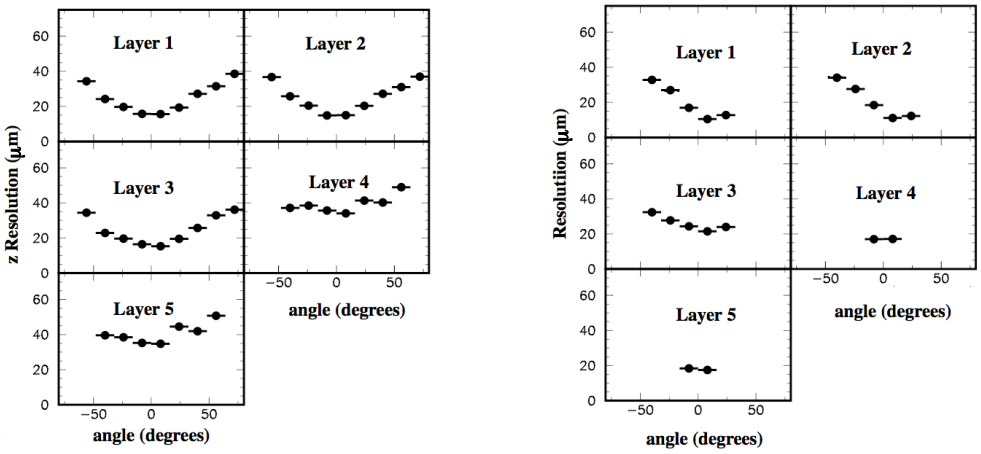

(a) (b)

Figure 3.11: The SVT's hit resolution as a function of the entry angle of the track in (a), the z-direction and in (b), the ϕ angle [33].

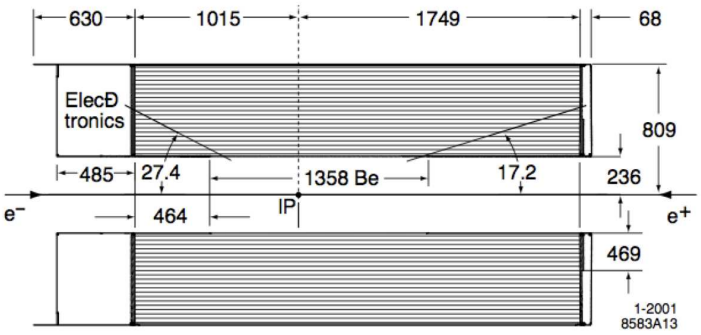

Figure 3.12: Longitudinal cross-section of the DCH showing its position relative to the beam line and the IP [33]. All dimensions are in millimeters.

3.4.2 Design and Assembly

The DCH was cylindrical, approximately $3\ m$ long, over $1.5\ m$ in diameter and comprised 40 concentric layers of cells. Each cell contained several wires and was capable of making both a hit and an ionization energy loss measurement for a track. As well as radial and angular measurements, longitudinal measurements were also possible because over half of the wires were set at an angle to the beam line.

To reduce the amount of multiple scattering, low mass aluminium field wires were used, and a gas mixture of 80% helium, 20% isobutane resulted in a relatively large radiation length. The inner and outer walls of the DCH were as low in mass as possible, which helped to reduce track matching ambiguities across

the SVT/DCH and DCH/DIRC boundaries. The power supplies and readout electronics of the DCH were placed on its backward end-plate to further reduce unnecessary material between subsystem layers.

3.4.3 The Cells

The 7104 cells of the DCH were divided into layers, with four layers forming a super-layer and ten super-layers in total. Within each super-layer, every cell wire was aligned the same way. Figure 3.13 shows the cell arrangement for the first four super-layers. The first and fourth super-layers were axial *A*, while the second and third super-layers, *U* and *V*, formed a pair of stereo layers. Thus, the ten super-layers were arranged in the following manner; *AUVAUVAUVA*.

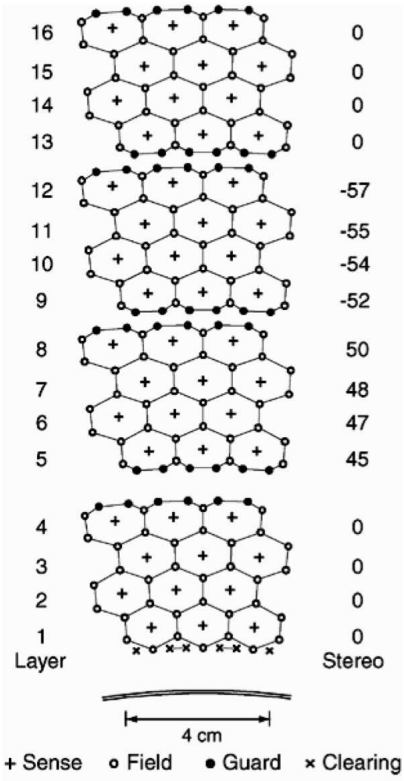

Figure 3.13: The typical DCH cell arrangement for the first four super-layers [33]. The Stereo numbers down the right hand side show the angle made between the sense wire of the cell and the beam axis.

The hexagonal cell structure can be seen in figure 3.13, where the short and long axes of the cell were approximately $12\ mm$ and $19\ mm$ respectively. At

the centre of the cell was a positive voltage sense wire that was operated at $\approx 2\ kV$. It was made from high resistivity tungsten-rhenium and surrounded by six grounded aluminium field wires that formed the hexagonal shape.The overall avalanche gain of the cell was around 5×10^4.

The super-layers were bounded by additional 'guard' wires (see figure 3.13) that were used to help keep the gain constant for those cells near to the edges of the super-layers. Two 'clearing' wires were also present for every cell of the first and last DCH boundaries to collect the charges produced by photon conversions that were more frequent at the layer boundaries due to the increase in material.

3.4.4 Electronics

The DCH electronics measured two signal attributes, the accumulated avalanche charge and the drift time. For a typical charged particle traversing $1\ cm$ of the DCH, around 22 primary 44 secondary ionizations occurred. Using the signal timing, the primary ionization position was deduced with a mean cell resolution of $\approx 140\ \mu m$.

The electronics front-end assembly (FEA) readout components were attached to the backward endplate inside compact readout modules. Water-carrying brass bars radially segmented the DCH sections and provided both cooling to the FEAs and structural support.

The front-end assemblies (FEAs) contained a number of amplifier/digitizer boards (ADBs) that catered for the cell channels within each superlayer and passed signals to the readout modules. Within the ADBs were amplifier ICs that processed incoming signals to find drift time and energy loss information. After digitization these signals were held in a latency buffer, pending a decision from the L1 trigger.

3.4.5 Monitoring and the Gas System

A calibration of the FEE to find constants and scaling factors for each of the DCH channels was carried out every 24 hours. Cell wire voltages and currents were

monitored, and the radiation dose experienced by the DCH was recorded, as were readings for humidity and temperature.

The DCH was filled with a gas mixture of four parts helium to one part isobutane that was held at around $4\ mbar$ over-pressure inside the DCH's $5.2\ m^3$ volume. The mixture was recirculated constantly and the flow rate, temperature and pressure of the mixture were monitored, as was its gain.

3.4.6 Performance

Clean leptonic events allowed the relationship between drift distance and drift time to be measured. The relationship between drift distance and position resolution for a single layer can be seen in figure 3.14.

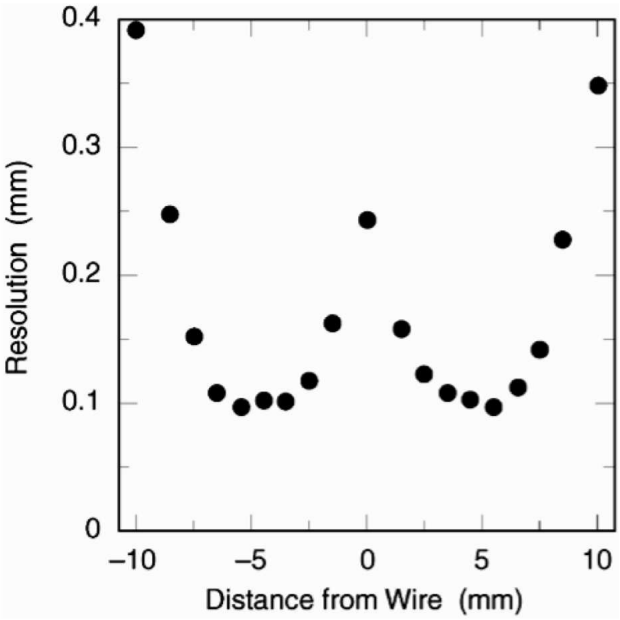

Figure 3.14: The DCH position resolution as a function of distance from the sense wire [33].

The level of ionization energy loss could be inferred from the amount of charge collected by cells over a given time period. Figure 3.15 shows the energy loss curve as a function of momentum for various particles.

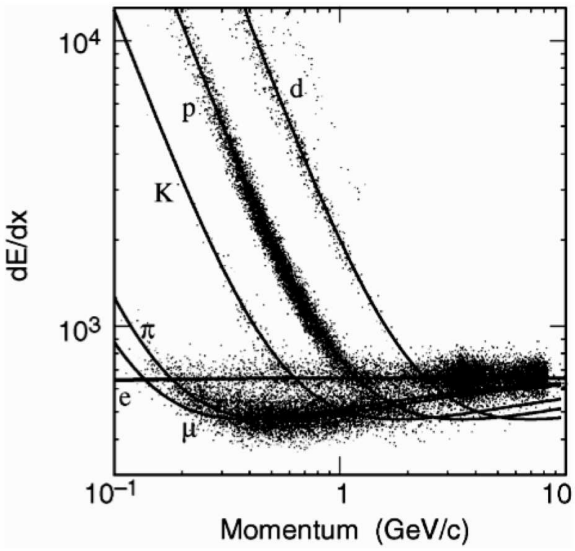

Figure 3.15: Energy loss curves for different types of particle interacting with the DCH; dE/dx as a function of momentum [33].

3.5 Charged Particle Tracking

3.5.1 Reconstruction of Charged Particles

The tracks of charged particles were reconstructed using both the SVT and the DCH and parameterized using five variables; d_0, z_0, ϕ_0, ω and $\tan\lambda$. Taken in the x-y plane and along the z-axis, respectively, d_0 and z_0 were the distances from the nominal point of origin ($x = 0$, $y = 0$, $z = 0$). The angle, ϕ_0, was the azimuthal angle, and the angle made between the track and the transverse plane was λ, which was also known as the 'dip-angle'. The track's curvature, ω, was proportional to the reciprocal of its transverse momentum. Tracks were initially parameterized using DCH measurements to define a trajectory. To obtain the final parameter values, this trajectory was extended into the SVT region where consistent SVT hits were added and a complete fit was performed using both SVT and DCH information.

3.5.2 Track Detection Efficiency

The detection efficiency of the DCH was given by the fraction of tracks detected by the DCH that were first detected in the SVT (provided that the DCH accep-

tance requirements were satisfied). The results of a typical efficiency study, performed using hadronic decays, are given in figure 3.16, where the drop in efficiency at a polar angle of $\pi/2$ illustrates the effect of lowering the sense wire voltage from the design value. While the DCH detection efficiency tailed off for transverse momenta below $\approx 500\ MeV/c$, as can be seen in figure 3.17, the SVT maintained a high efficiency down to around $50\ MeV/c$.

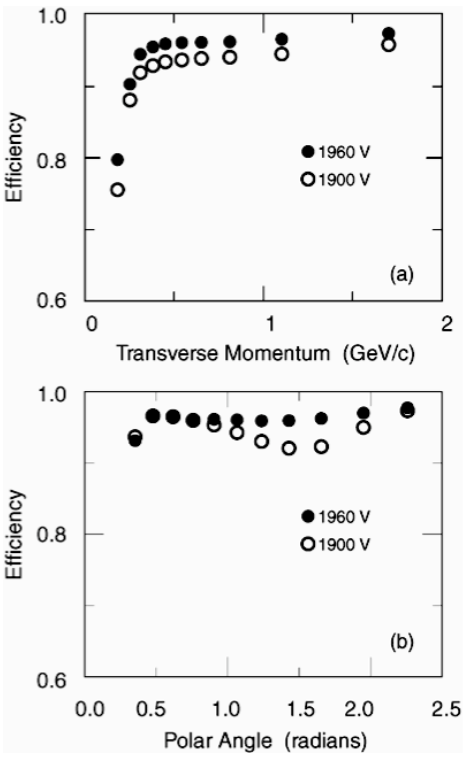

Figure 3.16: Charged particle tracking efficiency as a function of momentum (a) and angle (b) [33].

3.5.3 Resolution on Track Parameters

The resolution on each of the track parameters was obtained using hits from tracks produced by cosmic rays that passed through both the DCH and SVT. The hits were divided into two groups. Those in the top half of the detector were fitted as one track, while those in the bottom half of the detector were fitted as a different track. Parameter resolutions were obtained from the difference between each set of the track's parameters. For a given track (with momentum greater than $3\ GeV/c$), the resolutions of four of the five track parameters were as follows;

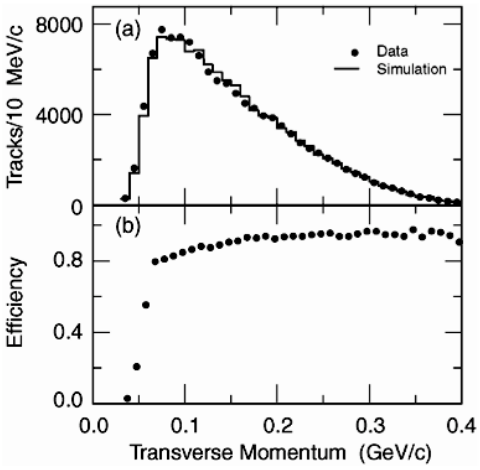

Figure 3.17: Number of tracks (a) and detection efficiency (b) as functions of transverse momentum [33].

- $\sigma_{d_0} = 23\ \mu m$

- $\sigma_{\phi_0} = 0.43\ mrad$

- $\sigma_{z_0} = 29\ \mu m$

- $\sigma_{tan\lambda} = 0.53 \times 10^{-4}\ \mu m$

The resolution of the fifth parameter, ω, is related the the transverse momentum resolution, σ_{p_t} and shown in figure 3.18.

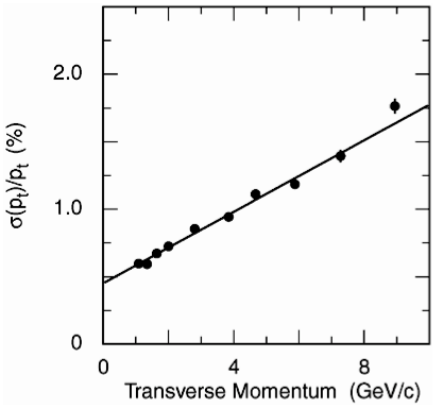

Figure 3.18: Transverse momentum resolution of the tracking system as a function of transverse momentum [33].

3.6 The DIRC

3.6.1 Overview

Figure 3.19 illustrates how the DIRC operated. It shows the passage of Cerenkov light from a charged track that has passed through the detector. Cerenkov photons were radiated from rectangular bars made of synthetic fused silica that had a high refractive index, a long attenuation length and were radiation hard. Total internal reflection ensured that radiated light stayed within the bar and any photons that moved towards the forward end were reflected off a mirror, back towards the instrumented end of the DIRC (i.e. the right hand side of figure 3.19).

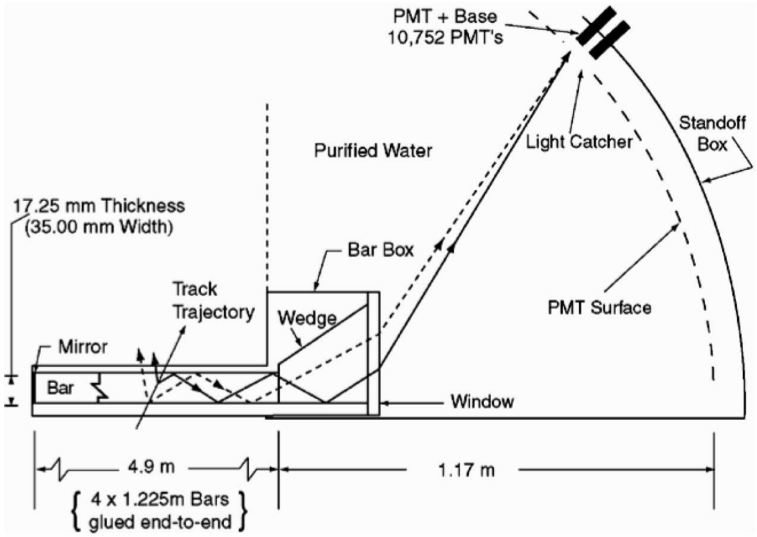

Figure 3.19: The DIRC System [33].

The nature of the initial light cone that was produced in the bar by the track was preserved until the photons were detected using photomultiplier tubes (PMTs) that were located toward the backward end of the detector. To represent the photon's trajectory, a vector was taken from the centre of the end of the bar to the centre of the PMT. Using this vector, along with SVT and DCH information about the original track the Cerenkov angle, θ_C, was found. The Cerenkov angle could then be used to find the speed of the charged track via the relation $cos(\theta_C) = 1/n\beta$, where n and β represent the refractive index of the silica bar and the speed of the particle relative to the speed of light. By combining

the hit location on the PMT surface with timing information, the DIRC became a three-dimensional detector that was able to discriminate against out of time background events.

3.6.2 Design

The DIRC barrel consisted of 12 segments, with each segment containing a bar box that held 12 fused silica bars. Figure 3.20 shows a diagram of a bar box. Housed in an aluminium skin, the 12 bars were capped at the forward end by a mirror, while at the backward end the bars were covered by a reflective wedge and a window. The reflective wedge was used to angle any light that was close to perpendicular to the beam axis towards the PMTs and the fused silica window provided a sealed interface to the 'Standoff Box' (SOB).

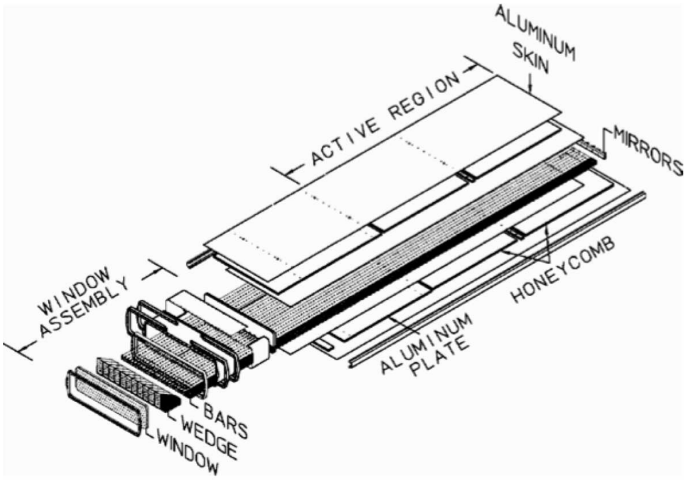

Figure 3.20: DIRC bar box components [33].

The SOB was filled with $6000\ l$ of water, and housed the PMTs. De-ionized and purified, the water within the SOB helped to mitigate the attenuation of light down to wavelengths of $\approx 300\ nm$. Water was chosen due to its similar refractive index to the fused silica, which maximized the light transmission from the bar box window. The SOB, and the rest of the DIRC geometry, can be seen in figure 3.21.

There were 10752 PMTs in the SOB, divided equally between the 12 sectors.

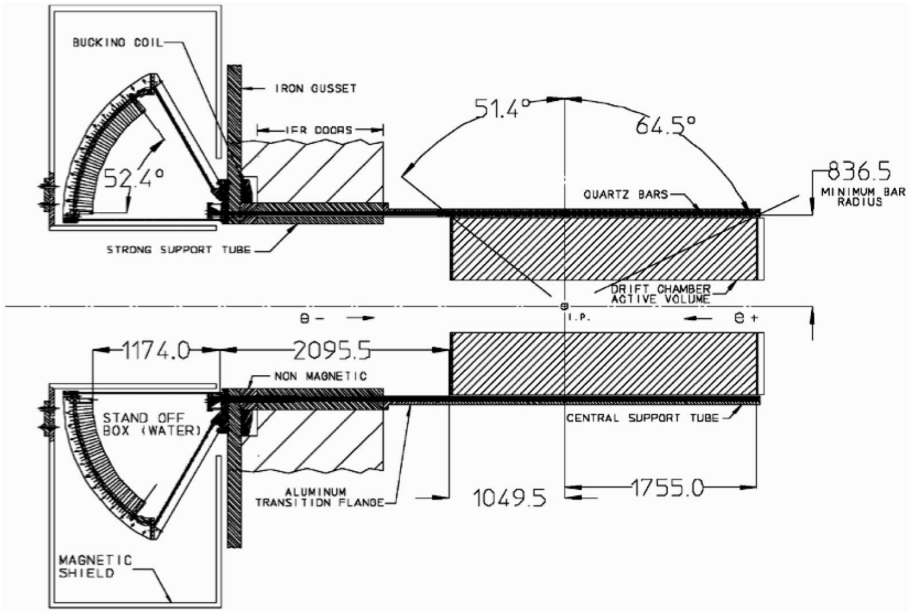

Figure 3.21: The DIRC Standoff box (left) in relation to other DIRC components, as well as the DCH (right) [33]. All dimensions are in millimeters.

The catchment area of each PMT was increased by using a reflective cone that was mounted upon it, which resulted in $\approx 90\ \%$ coverage of the active surface area.

3.6.3 Electronics, Calibration and Monitoring

The arrival time of a Cerenkov photon at a PMT was recorded by the FEE of the DIRC. The PMT timing had an intrinsic precision of $\approx 1.5\ ns$, which limited the timing resolution. Amplified DIRC signals were sent via fiber-optics to ROMs where they were analyzed using a feature extraction algorithm.

Calibration of the PMT response time and other delays due to the electronics was carried out using two different calibration methods, although they both produced similar results. In the first method, each of the 12 sectors was subjected to $1\ ns$ long pulses of light from an LED light pulser. Using tens of thousands of pulses, the resolution on the time delay of each PMT was measured and the analogue-to-digital conversion (ADC) output from the pulses was also used to measure the gain of each PMT. For the second method, each PMT recorded

$\approx 100,000$ actual events whose readings were used to find Δt_γ, where Δt_γ represented how far the measured photon hit time was from a nominal value.

3.6.4 Performance and Candidate Reconstruction

DIRC measurements for a typical di-muon event are shown in figure 3.22, where the right-hand image shows the reduction of background photons as the size of the trigger window is reduced from $300\ ns$ to $8\ ns$. Cerenkov photons from typical tracks arrived inside a window of $\approx 50\ ns$.

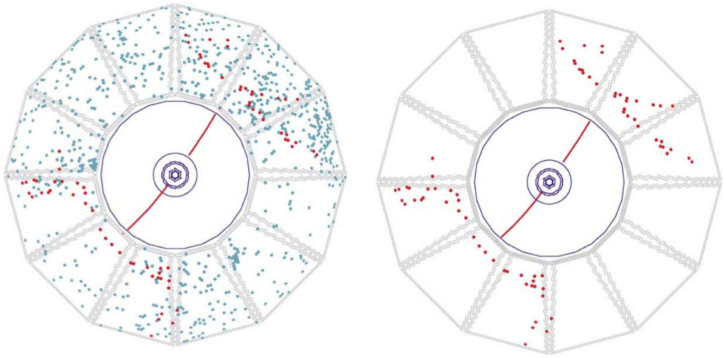

Figure 3.22: Images of the DIRC event display for a typical di-muon event [33]. The same event is shown in each picture, however the right-hand side display was obtained using a narrower timing window.

The passage of the photon, taken to be from the centre of the end of the bar to the PMT that detected it, defined a vector. Using Snell's law, the vector could be extended back along the radiator bar, and ultimately used to find θ_C and the azimuthal angle, ϕ_C, of the photon. As well as removing beam-background photons, the timing information of the DIRC was used to veto tracks that would otherwise be consistent with photon hits. After suitable candidates were found, they underwent a reconstruction algorithm in which each track was assigned a likelihood of being either an electron, muon, pion, kaon or proton.

The track Cerenkov angular resolution, σ_{θ_C}, was found to be around $10.2\ mrad$, depending on both the number of Cerenkov photons detected, and the resolution on the single photon Cerenkov angle.

For tracks with momenta up to around $3.5\ GeV/c$, an efficiency of $\approx 96\%$ was

achieved for kaon detection, while the probability of mis-identifying a pion as a kaon was $\approx 2\%$.

3.7 The Electromagnetic Calorimeter

3.7.1 Overview

The EMC detected electrons and photons via the electromagnetic showers they caused as they passed through the calorimeter. High resolution measurements of both the energy and angle of the shower were required. In principle, energy and angular resolutions of a few percent and several mrads were possible.

The energy range of the EMC spanned from $\approx$ 20 MeV to $\approx$ 9 GeV. The low limit came from the need to detect low energy photons, either from neutral particle decays or from other electromagnetic processes. The upper limit allowed the detection of clean QED processes like $e^+e^- \to e^+e^-(\gamma)$ and $e^+e^- \to \gamma\gamma$, which were useful in calibrating the EMC.

3.7.2 Design

Thalium doped, caesium iodide crystals (CsI(Tl)) were chosen to be the calorimeter material because they have a high light yield (50,000 photons / MeV) and a small Molière radius ($3.8\ cm$) and radiation length ($1.85cm$). It is possible to empirically describe the energy resolution (σ_E/E) of an homogeneous crystal calorimeter using equation 3.1 where E, the energy of a photon, and its RMS error, σ_E, are both in GeV:

$$\frac{\sigma_E}{E} = \frac{a}{\sqrt[4]{E}} \oplus b \tag{3.1}$$

At low energy, the a term, which accounts for fluctuations in photon statistics and electronics noise, dominates. At energies greater than $\approx 1GeV$ the b term dominates. It contains information about light leakage from the crystal, inhomogeneous light collection and calibration uncertainty. Under ideal conditions both a and b approached a few percent for *BABAR*.

Another empirical formula, this time for the angular resolution of the EMC, is given in equation 3.2:

$$\sigma_\theta = \sigma_\phi = \frac{c}{\sqrt{E}} + d \tag{3.2}$$

Here, σ_θ and σ_ϕ refer to the resolution in polar and azimuthal coordinates, E is in GeV, and the lowest values of c and d were $\approx 3\ mrad$ and $\approx 1\ mrad$.

3.7.3 Layout

The EMC was composed of two sections, a barrel and an endcap. The barrel had 5760 crystals, equally distributed over 48 rings and the endcap held 820 crystals spread over 8 rings and together they gave, in the cm frame, a solid angle coverage of $\approx 90\ \%$. Figure 3.23 shows a cross section of the crystal arrangement of the EMC.

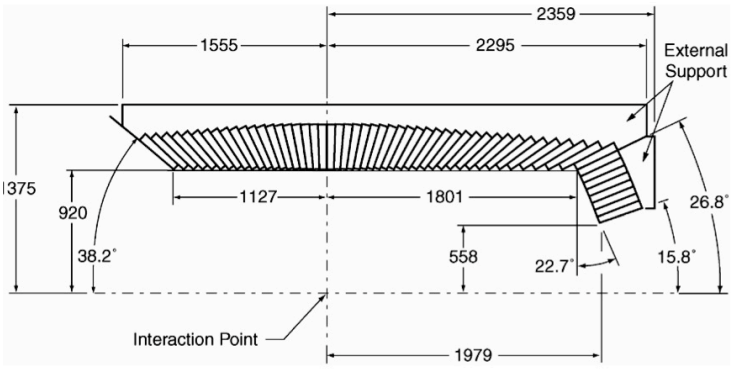

Figure 3.23: Longitudinal cross-section of the EMC's 56 crystal rings (48 in the barrel and 8 in the endcap) [33]. All dimensions are in millimeters.

3.7.4 Crystals and Photodiodes

The crystals were shaped in a way that guided light towards photodiodes that were mounted on their rear surface. They were also reflective at their internal surfaces in order to retain as much light as possible. Crystals were covered with a Faraday shield in the form of aluminium foil and electrically isolated from the EMC's support structure by a layer of mylar.

The photodiode and preamplifier setup is shown in figure 3.24. The two silicon photodiodes, shown in black, are visible at the rear of the crystal.

Photodiode output was amplified using a low-noise preamplifier before being processed by the rest of the readout electronics. Each assembly was designed to allow the heat generated by its preamplifier to dissipate out through an aluminium frame to the support structure.

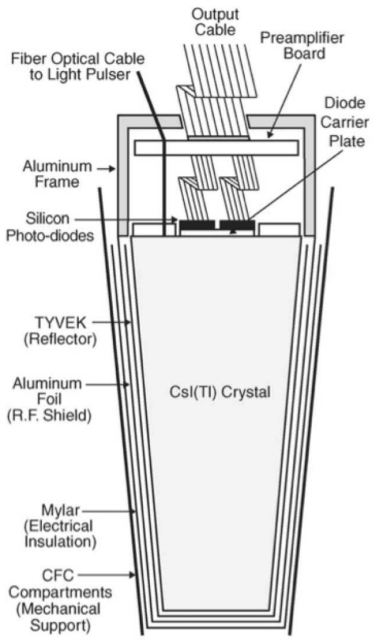

Figure 3.24: Crystal and electronics assembly [33].

3.7.5 Support structure

The barrel section of the external aluminium support structure that held modules of crystals in place is shown in figure 3.25. The load of the support structure was borne by four supports that were capable of flexing and bending as required in order to dampen any movements caused by earthquakes.

Every crystal was held in place using a carbon-fibre-epoxy composite (CFC) tube, meaning that the greatest force that a crystal could experience was that of its own weight. This helped to minimize crystal deformations and maintain the level of crystal performance. To minimize the amount of material in front of the crystals, the crystal modules themselves were supported by rear-mounted

aluminium frames called *strongbacks*.

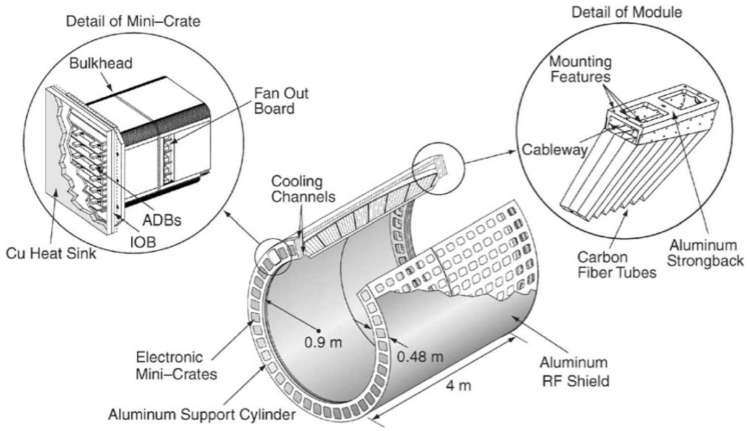

Figure 3.25: A schematic of the barrel section of the EMC support structure [33]. The left-hand closeup shows a typical FEE crate and it's associated boards. The right-hand image shows how a module of crystals was mounted and the central image is a schematic of the support structure itself.

3.7.6 Cooling system

It was important to keep the electronics and crystals of the EMC at a constant temperature, as a relatively sudden change in temperature could have damaged the glue that held the diodes to the crystals, and photodiode leakage was also exponentially linked to temperature. Heat came primarily from the preamplifiers and the EMC electronics crates that were mounted on the ends of the barrel support structure. Heat from the barrel and endcap preamplifiers was conducted up through the strongbacks and cooled by pipes containing Fluorinert (polychlorotrifluoro-ethylene). The FEE crates of the barrel were cooled by water, while those of the endcap were again cooled by Fluorinert.

3.7.7 Electronics Readout and Calibration

After installation, it became impossible to access any crystals, photodiodes or preamplifiers. Having two photodiodes for each crystal, each with its own preamplifier, provided a means of redundancy. In general, the average of the

two signals from the photodiodes was taken, but, if one diode failed, then the other could be used as a standalone.

Figure 3.26 shows the relationship between the various EMC electronics components. Preamplification of $\times 1$ and $\times 32$ was performed on signals that came from the crystal, before a *custom auto-range encoding* (CARE) circuit, located on the detector, further amplified the signal. This resulted in the following gains for a given energy range; $\times 256$ for $0.50\ MeV$, $\times 32$ for $50 - 400\ MeV$, $\times 4$ for $0.4 - 3.2\ GeV$ and $\times 1$ for $3.2 - 13.0\ GeV$.

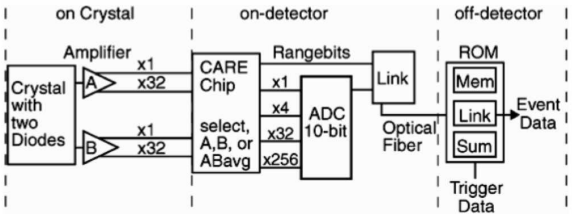

Figure 3.26: Components of the readout electronics [33] .

The various gains were subject to non-linearities, some of which came from cross-talk, where energy readings read by one amplification channel could induce small false readings in adjacent channels. These readings were small, typically less than around $1\ \%$ of that from the original channel.

To calibrate each EMC crystal, the measured pulse heights were converted into equivalent shower energies, which were then associated with incoming particles. Using two measurements as reference points, one at each end of the EMC's nominal range, energy measurements could be calibrated. The low energy point involved measuring the energy deposited in the calorimeter from photons produced in ${}^{16}O^{*} \rightarrow {}^{16}\ O\gamma$ decays, while at high energies Bhabha events were used.

3.7.8 Monitoring

The temperature of the EMC was maintained at $\approx\ 20^{o}C$, and nitrogen gas was pumped throughout it to keep it dry. To monitor the effects of the radiation, dosimeters were placed in front of some of the crystals in the barrel and endcap. During operation, the endcap, and to a lesser extent the forward barrel, received

a greater integrated luminosity, and a corresponding decrease in the crystal light yield was observed.

3.7.9 Reconstruction and Performance

Electromagnetic showers were usually spread over a small group of crystals. Software was used to identify different types of group depending upon the number of energy maxima observed, and whether the incident particle had been charged or neutral. If only one maximum was found in a group, the group was called a *cluster*. On the other hand, if a group contained several maxima, it was called a *bump*. Whether or not a cluster/bump was associated with a track was dictated by the difference in position between the centre of the cluster/bump and the point where the track met with the calorimeter. A cluster/bump was deemed to have come from a neutral particle if there was no track that could be associated with it.

The energy resolution, $\frac{\sigma_E}{E}$, at $6.13\ MeV$ (using the $^{16}O^*$ source) was $5.0 \pm 0.8\%$, while at high energy (using Bhabha events) it was $1.9 \pm 0.07\%$. More generally, the energy resolution was given by equation 3.3:

$$\frac{\sigma_E}{E} = \frac{(2.32 \pm 0.30)\%}{\sqrt[4]{E(GeV)}} \oplus (1.85 \pm 0.12\%) \tag{3.3}$$

Measurement of the angular resolution was based upon the two-photon decay of π^0 and η particles. In mrad, the angular resolution as a function of energy was given by equation 3.4:

$$\sigma_\theta = \sigma_\phi = \left(\frac{3.87 \pm 0.07}{\sqrt{E(GeV)}} + 0.00 \pm 0.04 \right) \tag{3.4}$$

3.8 The Integrated Flux Return

3.8.1 Overview

Muon detection, needed for leptonic and semi-leptonic decays, and neutral hadron detection, important when measuring exclusive meson decay modes, were the goals of the Integrated Flux Return. To achieve these goals, the steel flux return of the solenoid magnet was used to absorb neutral hadrons, and detect muons. A prime example of a decay that could not have been measured without the IFR is $B^0 \rightarrow J/\Psi K_L$, where the J/Ψ can decay into $\mu^+\mu^-$, and the K_L can travel for many metres before decaying. Like all of *BABAR*'s subsystems, a reasonable efficiency over large angles was important. Also, the nature of the IFR construction made access difficult, so the components had to be reliable.

3.8.2 Resistive Plate Chambers

Muons and neutral hadrons interacted with the IFR, and were detected by resistive plate chambers (RPCs) that were positioned between the layers of the IFR's barrel and end-door sections. Figure 3.27 shows a diagram of the sections of the IFR. Of the 19 barrel and 18 endcap layers, the innermost nine layers were $2\ cm$ thick while the remaining layers were $10\ cm$ thick, and between each layer there was a $3.2\ cm$ gap ($3.5\ cm$ for the layers of the inner barrel). There were also a pair of cylindrical layers around the EMC to detect particles before they passed through the superconducting coil.

The RPC design is shown in figure 3.28. A particle passing through an RPC could ionize atoms in the gas layer that was bounded by two high resistance bakelite sheets. This produced a stream of particles that, through capacitive coupling, produced a signal in the readout strips. The strips (X and Y on figure 3.28) provided two-dimensional measurements because they were orthogonal to one another.

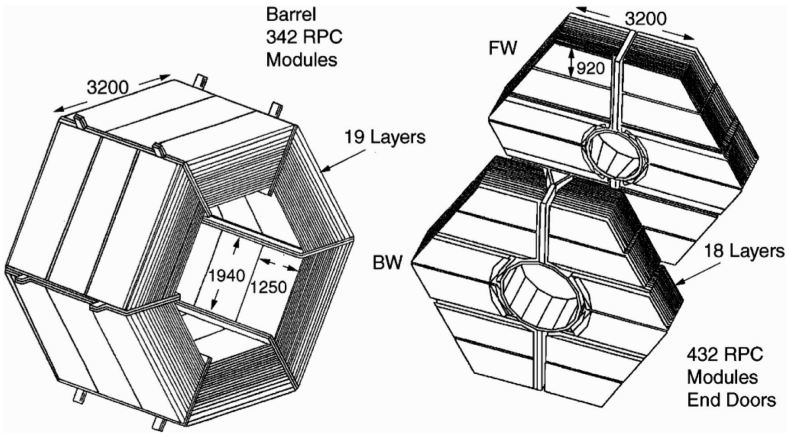

Figure 3.27: The IFR barrel and endcap sections [33].

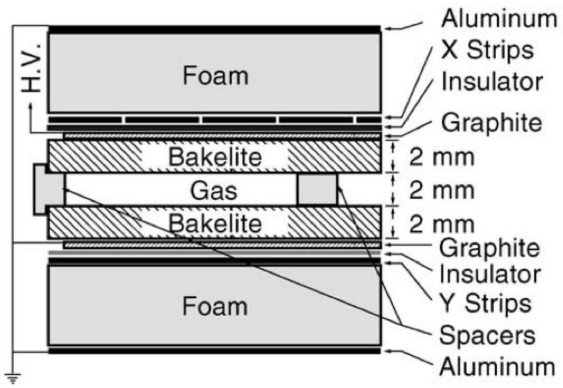

Figure 3.28: RPC schematic showing the gas layer, bakelite insulators and readout strips [33]. The foam layers were used to help strengthen the structure.

3.8.3 Design of RPCs

The barrel, end door and cylindrical layers of the IFR held 342, 432 and 32 RPCs, respectively. RPCs modules were joined to form a larger chambers, as required, in order to meet a given layer geometry. In each barrel sector there were three modules per layer, and to measure the z coordinate, each of these modules contained 32 strips orientated at 90° to the z axis. Similarly, the azimuthal (or ϕ) coordinate was measured using 96 strips aligned along the z direction. Three pairs of RPC modules, equipped with both horizontal and vertical strips, made up the chambers in each end-door half. The cylindrical RPC had an outer layer containing orthogonal sets of readout strips to measure θ and z, while diagonal readout strips u and v were used in an inner layer, set at an angle to the z-axis.

A typical event resulted in signals from around 100 readout strips. The readout strips carried their signals to the IFR's front-end cards (FECs), where they were processed before being passed, via the FEE, to ROMs.

3.8.4 Efficiencies and Performance

Weekly cosmic ray muon data were taken to find the RPC efficiency. The resulting RPC efficiencies from an early period of running are shown in figure 3.29. Most modules were better than $90\ \%$ efficient, although there was clear evidence of a degradation in performance with time for some of the modules. (The source of this decrease in performance was never fully understood.)

Testing showed a relationship between the dark current of the RPCs and their temperature. A $1°C$ increase in temperature resulted in around a $14 - 20\%$ rise in the amount of dark current. A water cooling system was introduced in an attempt to rectify this problem. After installation, the temperature throughout the IFR was maintained between roughly $20°C$ and $24°C$.

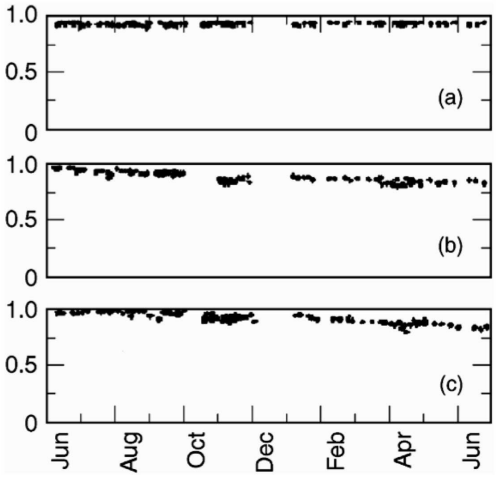

Figure 3.29: The efficiency levels of the RPC modules over a year [33, p88]. The plots (a), (b) and (c) represent three categories of RPC; stable, unstable and very unstable, respectively.

3.8.5 Identification of Muons

The IFR worked with the other sub-systems to identify muons. Using the SVT and DCH, a track was extended into the IFR region and, when passing through the EMC, the track had to be consistent with a minimum ionising particle (MIP). The effects of multiple scattering, energy loss due to ionization and the magnetic field on the path of the particle were all taken into consideration. Hits within the IFR were grouped into *clusters*, and those clusters that were consistent with the extended track trajectory were deemed to have originated from the incident particle.

A number of variables were used to differentiate muon clusters from those of hadrons. One variable used was the distance from the IP to the last RPC associated with the track, which could be used to determine the number of interaction lengths for the track. Another variable used was the difference between the number of interaction lengths that were expected and the number of interaction lengths that were observed. The expected number of interaction lengths was found using the momentum and angle of the track, and assuming that the track had been produced by a muon. A fit of the extrapolated trajectory to the centroids of the clusters of the track produced a χ^2 value that could also be used as a variable.

The muon efficiency along with the pion fake-rate as functions of both momentum and angle can be seen in figure 3.30. (For the polar angle plot, the momentum, p, of the particles involved lay in the range $1.5 < p < 3.0 GeV/c$.)

3.8.6 Detecting K_L^0 and Neutral Particles

Neutral particles, like K_L^0s, produced signatures in the IFR that could not be related to any charged track coming from the IR. By aggregating these signatures, a composite cluster could be formed, and using the centroid of this cluster and the vertex of the event, the flight path of the neutral particle was found. The angular resolution on clusters coming from K_L^0 decay was estimated to be $\approx 60\ mrad$ using a sample of $e^+e^- \to \phi\gamma \to K_L^0 K_S^0 \gamma$ events, where the missing momentum

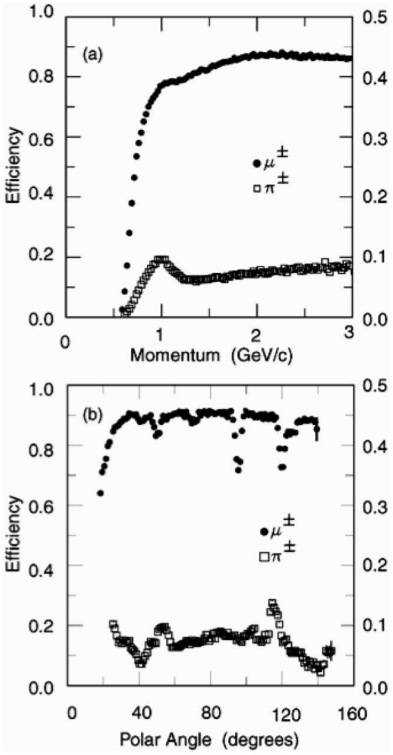

Figure 3.30: The muon detection efficiency and the pion fake-rate are shown as functions of both momentum (a) and polar angle (b) [33].

of the event was used to define the K_L^0.

Measurements could also be supplemented with the cylindrical RPC and EMC information. Using the IFR with the EMC, around a $20 - 40\%$ detection efficiency was achieved for K_L^0s with momenta between 1 and $4\ GeV/c$.

3.8.7 Upgrade

The decrease in efficiency seen in figure 3.29 ultimately led to an upgrade to the IFR barrel where the RPCs were replaced with *limited streamer tubes* (LSTs) [36]. One LST cell consisted of an HV sense wire that was inside a gas-filled tube, which was kept at a lower voltage. Groups of either 7 or 8 cells formed the LST modules that replaced the RPCs. Cylindrical coordinates were recorded for a particle that traversed the LST. The azimuthal angle, or ϕ coordinate, was determined using the readout from the sense wires in the LST cells. The beam-axis, or z coordinate, was found using readout strips that were mounted close to the LST cells, and at right angles to them. The resulting improvement in muon

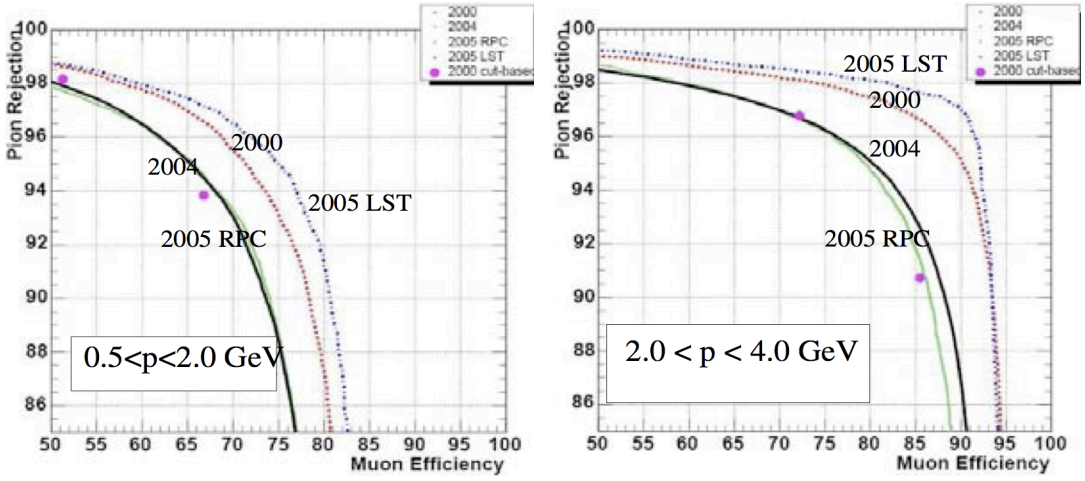

(a) (b)

Figure 3.31: The effect of the IFR upgrade [36]. The plots show the changing muon detection efficiency and pion rejection probability over different years of detector operation. The momentum, p, of each particle had to satisfy $(0.5 < p < 2.0)\ GeV$ in plot (a) and $(2.0 < p < 4.0)\ GeV$ in plot (b). The improvement due to the introduction of the LSTs is clear.

detection efficiency and pion rejection rates is shown in figure 3.31.

Chapter 4

Event Selection for an $f_{D_s^+}$ Measurement

4.1 Overview

This chapter documents work that was carried out by the author as part of an analysis to obtain a value for the decay constant of the D_s^+ meson, $f_{D_s^+}$, by measuring the absolute branching fractions $D_s^+ \to l^+\nu$, where $l^+ = e^+$, μ^+ or τ^+. The motivation behind the analysis has already been described in chapter 2. This chapter may be regarded as standalone; it is not related to the f_{D^+} analysis, apart from the fact that the motivations are similar.

The analysis strategy was based upon that of a previous BELLE analysis [37]. The basic method was to infer the presence of a D^{*+} meson by reconstructing all particles in an event, except those that came from the decay of the D^{*+} itself. In this way, an inclusive set of D^{*+} meson candidates could be obtained.

The reconstruction procedure that was used to find a D_s^{*+} candidate consisted of four main stages. The first stage involved the identification of a charm-flavoured *tag* within an event (the concept of a tag is discussed in section 4.4). In the second stage, a group of fragmentation particles was created using particles which were not related to the tag. Note that for a typical event there were many possible groups of fragmentation particles, which led to high candidate multiplicities. The third stage involved forming a nominal D_s^{*+} candidate, which

decayed via $D_s^{*+} \rightarrow D_s^+\gamma$, using the recoil four-momentum of the event. The recoil four-momentum was defined from the four-momentum of all particles in the event that were not associated with either the tag or fragmentation systems. In the final stage, leptonic D_s^+ decays were reconstructed by finding a suitable lepton candidate. The author was responsible for all aspects of the analysis that related to tag reconstruction.

In the following sections of this chapter, the $f_{D_s^+}$ analysis method is described in greater detail, followed by a discussion of the various stages of the tagging process. The datasets used in the analysis are presented, and an initial level of data processing, called *skimming*, is described. The various tag modes are then introduced and discussed. Finally, the optimisation procedure that was performed on the tag modes is described.

4.2 Analysis Strategy

The signal mode decay chain: $D_s^{*+} \rightarrow D_s^+\gamma$, $D_s^+ \rightarrow l^+\nu$, was not reconstructed explicitly. Instead, D_s^{*+} candidates were inferred by first performing a partial event reconstruction, and then assuming that the particles which had not been included were from the decay of the D_s^{*+}; this was known as the *whole event* method. The whole event method suffered from a lower signal efficiency than other methods that reconstructed only part of the event. However, the advantage of using the whole event method was that it resulted in an inclusive set of D_s^+ candidates. This meant that the branching fraction for the signal mode could be measured directly, without the need for a normalisation mode (like $D_s^+ \rightarrow \phi\pi^+$ [38]).

Event reconstruction involved three steps; first a *tag-side* was created, then a set of fragmentation particles was formed, and finally a nominal D_s^{*+} meson was defined. The *tag-side*, which could be either charged or neutral, contained either a: D^0; D^+; D_s^+ meson and a kaon; or a Λ_c baryon and an anti-proton. The kaon and anti-proton were required in order to balance strangeness and baryon number, respectively. Full details of the hadronic tags are given in section 4.4. The set of fragmentation particles, X, could contain up to three pions, where at most one

of the three could be a π^0. The D_s^{*+} was not reconstructed explicitly; instead, the recoil four-momentum of the event, $p_{D_s^{*+}}$, was attributed to a nominal D_s^{*+} candidate, where $p_{D_s^{*+}}$ was found using equation 4.1:

$$p_{D_s^{*+}} = p_{beams} - p_{ROE} \tag{4.1}$$

Here, p_{beams} and p_{ROE} represent the four-momentum of the beams and the combined four-momentum of the rest of the event (ROE), i.e. the tag-side and X systems. Candidate D_s^+ mesons were found by searching for a photon, consistent with $D_s^{*+} \rightarrow D_s^+\gamma$ decay, which was not already associated with either the tag-side or the X system. Thus, a set of D_s^+ candidates were found.

The four momentum of each D_s^+ candidate, $p_{D_s^+}$, was found using equation 4.2:

$$p_{D_s^+} = p_{beams} - (p_{ROE} + p_\gamma) \tag{4.2}$$

where p_γ represents the four-momentum of the photon from the $D_s^{*+} \rightarrow D_s^+\gamma$ decay. Events that contained a D_s^+ candidate and only one additional charged track, which was consistent with a muon hypothesis, were identified as signal candidates. Additional energy was also permitted in the event, provided that the total was below $1\ GeV$. The four-momentum of the neutrino candidate, p_ν, was then estimated using equation 4.3:

$$p_\nu = p_{beams} - (p_{ROE} + p_\gamma + p_\mu) \tag{4.3}$$

where p_μ represents the four-momentum of the signal muon candidate. The signal variable used in this analysis was M_{rec}^2, which was given by the magnitude of the four-momentum of the neutrino candidate, and peaked at $0\ GeV/c^2$ for signal events.

Data/MC Sample	Integrated Luminosity (fb^{-1})	Luminosity Scaling Factor
Data	521	-
$c\bar{c}$	1060	2.03
B^+B^-	1350	1.04
$B^0\overline{B}^0$	1370	1.05
$\tau^+\tau^-$	851	1.63
uds	935	0.90

Table 4.1: Datasets used in the $f_{D_s^+}$ analysis [39]. The entire dataset of *BABAR* was used; i.e. runs $1-7$, on- and off-peak, data and generic MC. The integrated luminosities for data and the generic MC samples are given, in fb^{-1}. The luminosity scaling factor relates the number of events in the generic MC sample to the number expected in data. For example, the $c\bar{c}$ MC sample contained around twice the number of $c\bar{c}$ events as expected in data.

4.3 Datasets

During the lifetime of the *BABAR* experiment there were a number of data taking periods, called *runs*, in which data from events produced by e^+e^- collisions were recorded. The majority of these collisions were *on-peak*, meaning that they were at a centre-of-mass energy of $10.58\ GeV$, which is equal to the rest mass of the $\Upsilon(4S)$ resonance. The $\Upsilon(4S)$ contains a b quark and a $\bar{b}$ quark and decays to a B meson and a $\bar{B}$ meson. Around 10% of the data recorded came from *off-peak* collisions in which the centre-of-mass energy was lowered to $10.54\ GeV/c^2$ (i.e. just below the threshold for $\Upsilon(4S)$ production). At this energy, only *continuum* events were produced, i.e: $c\bar{c}$, $s\bar{s}$, $u\bar{u}$, $d\bar{d}$, $\tau^+\tau^-$, $\mu^+\mu^-$, e^+e^- and $\gamma\gamma$. In the present analysis, both on- and off-peak data for runs 1 to 7 were used, which represented the entire dataset of *BABAR*.

For each data on- and off-peak run, a corresponding set of five generic Monte Carlo (MC) samples were used: $c\bar{c}$, $B^0\overline{B}^0$, B^+B^-, $\tau^+\tau^-$ and uds. Here, uds refers to a MC sample that contained $u\bar{u}$, $d\bar{d}$ and $s\bar{s}$ events, in the correct proportions. The luminosity of each of the datasets used in the analysis is listed in table 4.1. The luminosity scaling factor for each of the generic MC samples (i.e. the ratio of the number of events in data to the number in the sample) is also given.

4.4 Skimming and Tagging

In the context of *BABAR* analyses, the term *skimming* was used to describe what was normally a fast event selection procedure. Every event in a dataset was analysed, and only those events that contained, for example, a certain topology, or the signature of a particular decay, were retained in a new, reduced dataset, called a *skim*. A more intensive analysis, which was usually more time consuming, could then be performed on the events of the reduced dataset.

For this analysis, a skim that consisted of 26 charm *tag* modes was used. *Tagging* is a standard analysis technique in which a predetermined set of tag decay modes for a particle are searched for in an event. Tag modes are usually chosen based on their branching fraction, decay topology, and the types of background they are susceptible to. Once a tag mode has been reconstructed, it is assumed that a corresponding anti-particle is also present in the event. In this way, a relatively pure sample of events that contain the anti-particle can be found, and one may search for the decay mode of interest within them. In the case of the present analysis, the particles used for tagging were the D^0, D^+ and D_s^+ mesons and the Λ_c baryon. In total, there were 6, 5, 7 and 8 D^0, D^+, D_s^+ and Λ_c tag modes, respectively; and they are listed in table 4.2.

D^0 Modes	D^+ Modes	D_s^+ Modes	Λ_c Modes
$D^0 \to K^-\pi^+$	$D^+ \to K^-\pi^+\pi^+$	$D_s^+ \to K^+K_S^0$	$\Lambda_c \to pK^-\pi^+$
$D^0 \to K^-\pi^+\pi^0$	$D^+ \to K^-\pi^+\pi^+\pi^0$	$D_s^+ \to \phi\pi^+$	$\Lambda_c \to pK^-\pi^+\pi^0$
$D^0 \to K^-\pi^+\pi^-\pi^+$	$D^+ \to K_S^0\pi^+$	$D_s^+ \to \phi\rho^+$	$\Lambda_c \to pK_S^0$
$D^0 \to K_S^0\pi^+\pi^-$	$D^+ \to K_S^0\pi^+\pi^0$	$D_s^+ \to K^-K_S^0\pi^+\pi^+$	$\Lambda_c \to pK_S^0\pi^+\pi^-$
$D^0 \to K^-\pi^+\pi^-\pi^+\pi^0$	$D^+ \to K_S^0\pi^+\pi^+\pi^-$	$D_s^+ \to \eta'\pi^+$	$\Lambda_c \to \Lambda\pi^+$
$D^0 \to K_S^0\pi^+\pi^-\pi^0$		$D_s^+ \to \phi\rho^0\pi^+$	$\Lambda_c \to \Lambda\pi^+\pi^0$
		$D_s^+ \to K^{*0}K^+$	$\Lambda_c \to \Lambda\pi^+\pi^+\pi^-$
			$\Lambda_c \to \Sigma\pi^+$

Table 4.2: Tag modes used as part of event reconstruction.

The reconstruction procedure for a tag candidate was essentially the same for all modes, and so only a summary of the procedure is given here.

Within an event, lists of candidates were created for each type of final state particle that was detected. These lists could then be used to create tag candi-

Dataset	Number of Events Pre-skim ($\times 10^6$)	Number of Events Post-skim ($\times 10^6$)	Skim Fraction (%)
Data	8630	1635	18.9
$c\bar{c}$	1380	965	70.0
B^+B^-	708	156	22.0
$B^0\overline{B}^0$	718	148	20.6
$\tau^+\tau^-$	800	32	4.0
uds	1950	1213	62.2

Table 4.3: The sizes of the skimmed datasets [39]. The numbers of data and generic MC events used in the analysis are given, before and after skimming. The fraction of events which passed the skim are also shown.

dates, which were subject to basic selection requirements. The mass of the tag candidate, which was found using simple four-momentum addition, had to be within around $160\ MeV/c^2$ of the nominal particle mass for the D^0, D^+ and D_s^+ modes, and within $\approx 350\ MeV/c^2$ of the nominal mass of the Λ_c. A vertex fit, in which the daughters were constrained to have the same point of origin, was performed on the candidate, and the probability of the χ^2 result of the fit had to be above 10^{-5} for all modes. After the fit, the mass of the tag candidate had to be within $\approx 100\ MeV/c^2$ of the nominal particle mass for the D^0, D^+ and D_s^+ modes, and within $\approx 50\ MeV/c^2$ of the nominal mass of the Λ_c. A minimum cm momentum cut of $2.0\ GeV/c$ was also applied to all candidates in order to remove background candidates from $B^0\overline{B}^0$ or B^+B^- events.

If any of the 26 tag modes were found in an event then the pointer to that event was stored in the skim. The initial numbers of events for each dataset used are given in table 4.3, along with the numbers of events which passed the skimming stage.

4.5 Optimisation of Tag Modes

After the skimming stage, optimised selection criteria, or *cuts*, were determined for each of the tag modes. The optimisation procedure was carried out using $\approx 8fb^{-1}$ of data luminosity (i.e. $\approx 1.5\%$ of all data events). The procedure was designed to maximise the significance, $S/\sqrt{S+B}$, of each tag mode, where S and

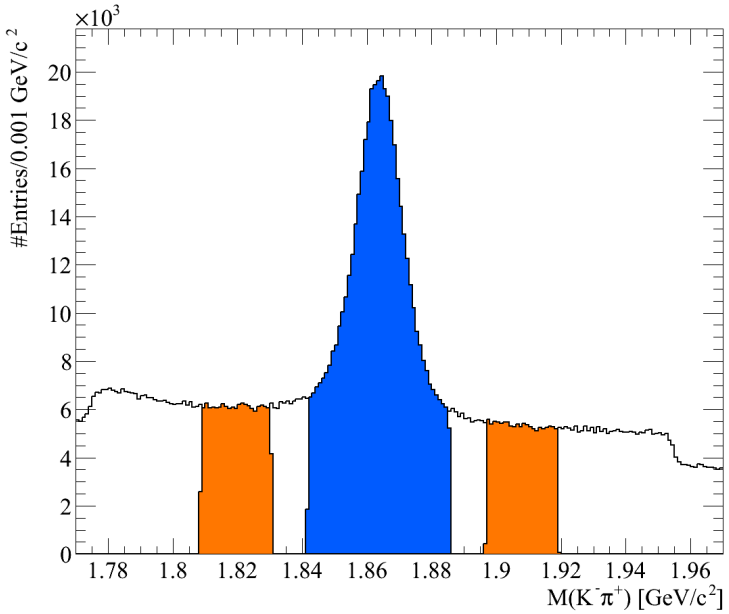

Figure 4.1: The mass distribution for $D^0 \to K^-\pi^+$ tag candidates, after the initial skim. The peak and sideband regions, which were used to estimate the numbers of signal and background candidates, are shown in blue and orange.

B represent the numbers of signal and background candidates for the mode. To determine S and B for a mode, the shape of its mass distribution was fitted with a function that contained a straight line component that represented the background shape, and a gaussian component that represented the shape of the peak. After the fit, the mean, μ, and standard deviation, σ, of the gaussian component were used to define a peak region, and two sideband regions in the mass distribution for the mode. Figure 4.1 shows these regions for the $D^0 \to K^-\pi^+$ tag mode.

The respective mass ranges of the peak region, M_{Peak}, and the lower and upper sideband regions, M_{Lower} and M_{Upper}, are given in 4.4, 4.5 and 4.6:

$$(\mu - 3\sigma) < M_{Peak} < (\mu + 3\sigma) \tag{4.4}$$

$$(\mu - 7.5\sigma) < M_{Lower} < (\mu - 4.5\sigma) \tag{4.5}$$

$$(\mu + 4.5\sigma) < M_{Upper} < (\mu + 7.5\sigma) \tag{4.6}$$

The total number of candidates in the sideband regions was used to estimate the number of background entries in the peak region, B, and S was defined as the

difference between the total number of entries in the peak region and B.

The optimisation procedure involved 8 variables in total. For each variable, cut values were defined using regularly spaced intervals, or *steps*, between a minimum cut value and a maximum cut value. For a given tag mode, the optimisation procedure calculated the $S/\sqrt{S+B}$ value for all possible combinations of cut values. The set of cuts which produced the highest $S/\sqrt{S+B}$ value was used for final tag candidate selection.

Three of the optimisation variables were related to the identification of charged particles as either kaons, pions or protons. For those modes that contained a K^+ candidate, a *Bagger Decision Tree* selector was applied to the track of the nominal K^+ (see section 5.4.1 for more information about Bagger Decision Tree selectors). The output of the BDT selector was a real number, between 0 and 1, where a value close to 0 indicated that the track was probably not produced by a K^+, while a value close to 1 indicated the opposite. A set of 5 cut variables for K^+ candidates were defined based upon the minimum allowed value for the output of the BDT selector. A set of 7 cuts for π^+ and p candidates were defined in a similar manner, based on a *Kalanand Mishra* selector (see section 5.4.2 for more information about Kalanand Mishra selectors). The cut ranges and step sizes of the remaining 5 optimisation variables are shown in table 4.4. For each variable, the minimum and maximum cut values are listed, as is the step size. The log of the probability of the χ^2 value for the vertex fit is given by $log(P(\chi^2))$. The centre-of-mass momentum and mass of the tag are represented by $P_{Tag}^{\rm cm}$ and M_{Tag}. The energies of the photon daughters of π^0 and η candidates are represented by $E^{\gamma}_{\pi^0}$ and E^{γ}_{η}.

Figures 4.2, 4.3, 4.4 and 4.5 show mass distributions for each set of tag modes: D^0, D^+, D_s^+ and Λ_c, respectively. In each figure, the mass distribution prior to optimisation is shown as a dashed line. The mass distribution after all optimised cuts have been applied, except the cut on the mass of the tag, is shown as a solid line. The final mass distribution, obtained after all of the optimised cuts had been applied, is shown in blue. Table 4.6 summarises the information relat-

Optimisation Variable	Minimum Value	Maximum Value	Step Size
$log(P(\chi^2))$	-5	-1	0.2
$P_{Tag}^{\rm cm}\ [GeV/c]$	2	3	0.1
$M_{Tag}\ [MeV/c^2]$	1.5σ	3.0σ	1
$E_{\pi^0}^{\gamma}\ [MeV]$	100	200	10
$E_{\eta}^{\gamma}\ [MeV]$	100	200	10

Table 4.4: Variables used in the optimisation of tag candidates. The optimisation procedure tested all possible cut value combinations, within the allowed minimum and maximum bounds, and in accordance with the step size for each variable. The definition of each variable is given in the text. The σ factor, used as part of the definition of the minimum and maximum values for M_{Tag}, refers to the standard deviation of the gaussian component of the function which was used to fit the mass distribution for the tag mode.

Decay Mode	Branching Fraction	$f_{D_s^+}$ Value (MeV)
$D_s^+ \to e^+\nu$	$< 2.3 \times 10^{-4}$	-
$D_s^+ \to \mu^+\nu$	$(6.02 \pm 0.38 \pm 0.34) \times 10^{-3}$	$265.7 \pm 8.4 \pm 7.7$
$D_s^+ \to \tau^+\nu\ (\tau^+ \to e^+\nu\bar{\nu})$	$(5.07 \pm 0.52 \pm 0.68) \times 10^{-2}$	$247 \pm 13 \pm 17$
$D_s^+ \to \tau^+\nu\ (\tau^+ \to \mu^+\nu\bar{\nu})$	$(4.91 \pm 0.47 \pm 0.54) \times 10^{-2}$	$243 \pm 12 \pm 14$

Table 4.5: Summary of results from the $f_{D_s^+}$ analysis. The branching fractions for the various $D_s^+ \to l^+\nu$ modes are given, where $l = e$, μ or τ. For each branching fraction, apart from $D_s^+ \to e^+\nu$ where only a 90% confidence limit was found, the corresponding $f_{D_s^+}$ value is shown. The uncertainties given for all values are statistical followed by systematic.

ing to the mass distributions for each of the tag modes, after optimisation. For almost all modes, there was, as expected, a considerable reduction in the fraction of background candidates in the peak region. The majority of tag candidates came from reconstructions of D^0 and D^+ decays.

Based on the optimised tag selection criteria that were found in this study, a high quality dataset that contained charm candidates was created. This dataset formed the basis of the rest of the $f_{D_s^+}$ analysis chain. The final results for the $f_{D_s^+}$ analysis are listed in table 4.5 [40]. Based on the values given in table 4.5 the decay constant for the D_s^+ meson was found to be:

$$f_{D_s^+} = (258.6 \pm 6.4 \pm 7.5)\ MeV \tag{4.7}$$

Here, the first and second uncertainties are statistical and systematic. A detailed

description of the $f_{D_s^+}$ analysis is given in reference [40].

Tag Mode	Mean (GeV/c^2)	Standard Deviation (MeV/c^2)	Fitted Number of Tag Candidates	Significance ($S/\sqrt{S+B}$)	Tag Yield (%)
$D^0 \to K^-\pi^+$	1.8638	7.4	248996	350.1	15.42
$D^0 \to K^-\pi^+\pi^0$	1.8626	12.9	312741	240.2	19.37
$D^0 \to K^-\pi^+\pi^-\pi^+$	1.8637	5.9	410438	136.9	25.42
$D^0 \to K_S\pi^+\pi^-$	1.8639	5.7	79578	167.0	4.93
$D^0 \to K^-\pi^+\pi^-\pi^+\pi^0$	1.8631	9.2	53864	50.8	3.34
$D^0 \to K_S\pi^+\pi^-\pi^0$	1.8627	10.9	45247	76.5	2.80
$D^+ \to K^-\pi^+\pi^+$	1.8685	6.0	218352	235.1	13.52
$D^+ \to K^-\pi^+\pi^+\pi^0$	1.8672	11.9	46206	35.1	2.86
$D^+ \to K_S\pi^+$	1.8689	6.5	24303	92.2	1.51
$D^+ \to K_S\pi^+\pi^0$	1.8678	13.2	33354	56.9	2.07
$D^+ \to K_S\pi^+\pi^+\pi^-$	1.8687	5.5	29685	48.1	1.84
$D_s^+ \to K^+K_S$	1.9676	6.5	7171	49.9	0.44
$D_s^+ \to \phi\pi^+$	1.9672	7.0	10402	72.4	0.64
$D_s^+ \to \phi\rho^+$	1.9662	11.3	6888	36.7	0.43
$D_s^+ \to K_SK^-\pi^+\pi^+$	1.9674	5.4	9594	24.1	0.59
$D_s^+ \to \eta'\pi^+$	1.9677	7.3	2521	20.1	0.16
$D_s^+ \to \phi\rho^0\pi^+$	1.9679	3.8	1400	17.4	0.09
$D_s^+ \to K^{*0}K^+$	1.9674	6.2	18663	60.9	1.16
$\Lambda_c \to p^+K^-\pi^+$	2.2857	5.0	35031	103.3	2.17
$\Lambda_c \to p^+K^-\pi^+\pi^0$	2.2843	9.5	7895	22.6	0.49
$\Lambda_c \to p^+K_S$	2.2859	5.7	5776	62.1	0.36
$\Lambda_c \to p^+K_S\pi^+\pi^-$	2.2856	4.1	3639	30.1	0.23
$\Lambda_c \to \Lambda\pi^+$	2.2863	5.1	415	14.5	0.03
$\Lambda_c \to \Lambda\pi^+\pi^0$	2.2837	17.1	1040	13.8	0.06
$\Lambda_c \to \Lambda\pi^+\pi^+\pi^-$	2.2856	5.0	1172	18.0	0.07
$\Lambda_c \to \Sigma\pi^+$	2.2859	3.7	142	9.0	0.01

Table 4.6: Optimisation results for each tag mode [39]. The means and standard deviations of the gaussian component of the fit function that was used to fit the mass distribution of each tag are given. The fitted number of tag candidates was found by integrating the gaussian component of the fit function. The tag yield represents the number of tag candidates for a given mode as a percentage of the total number of tag candidates.

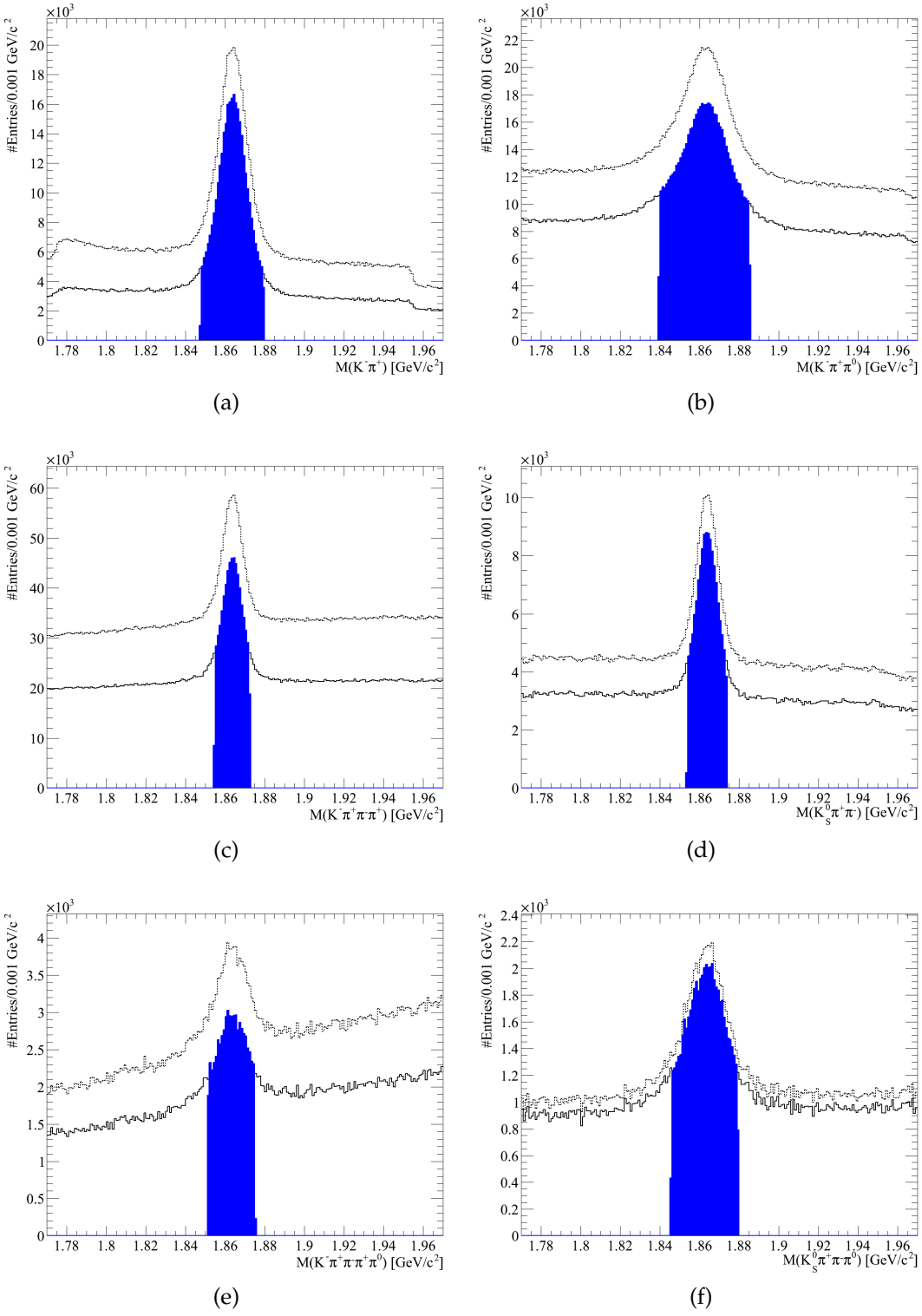

Figure 4.2: Mass distributions for the 6 D^0 tag modes. The dashed line represents the distribution after the initial skim. The solid line represents the distribution with all optimised cuts, apart from the mass window cut, applied. The final mass distribution is shown in blue, after all optimised cuts had been applied.

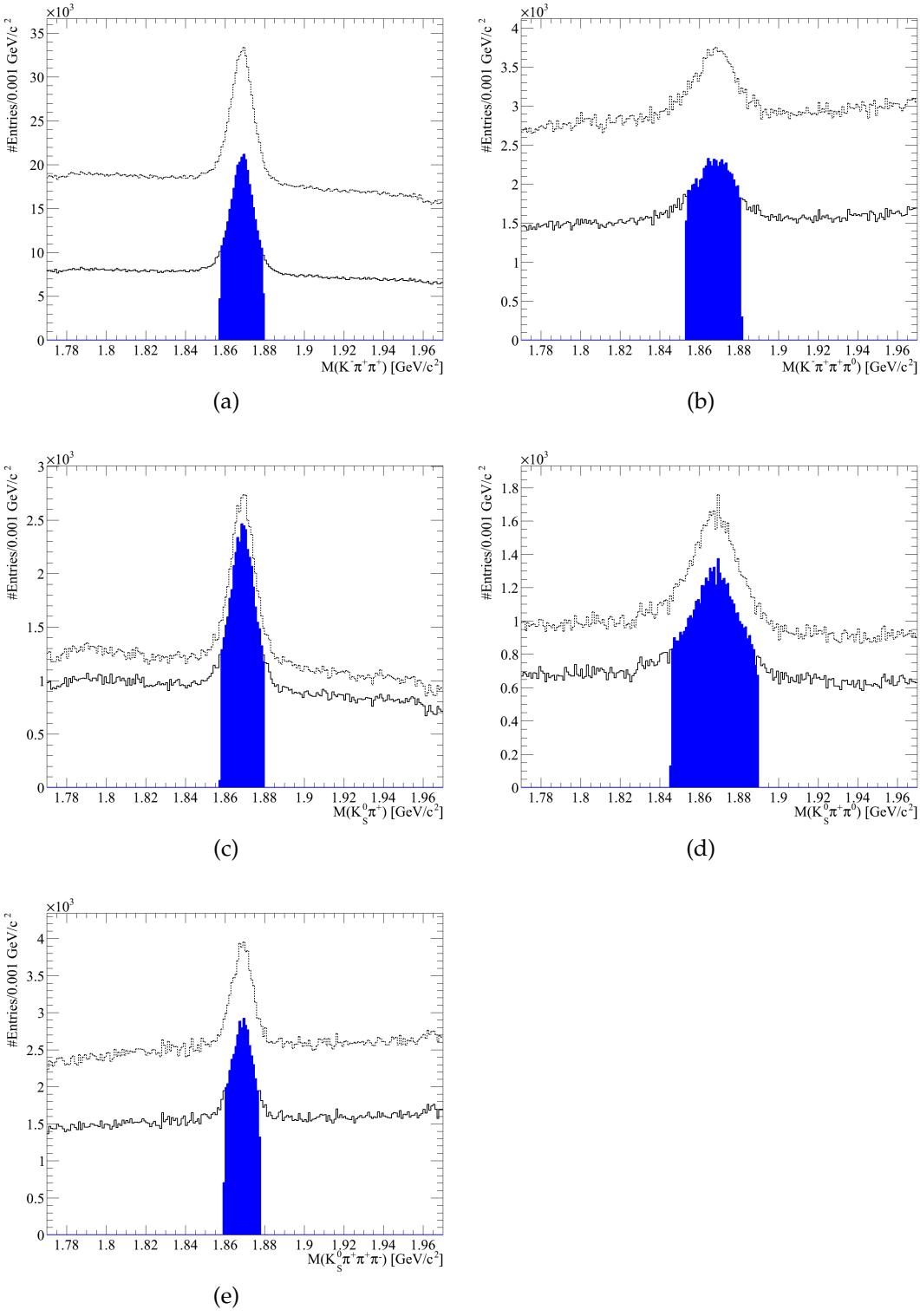

Figure 4.3: Mass distributions for the 5 D^+ tag modes. The dashed line represents the distribution after the initial skim. The solid line represents the distribution with all optimised cuts, apart from the mass window cut, applied. The final mass distribution is shown in blue, after all optimised cuts had been applied.

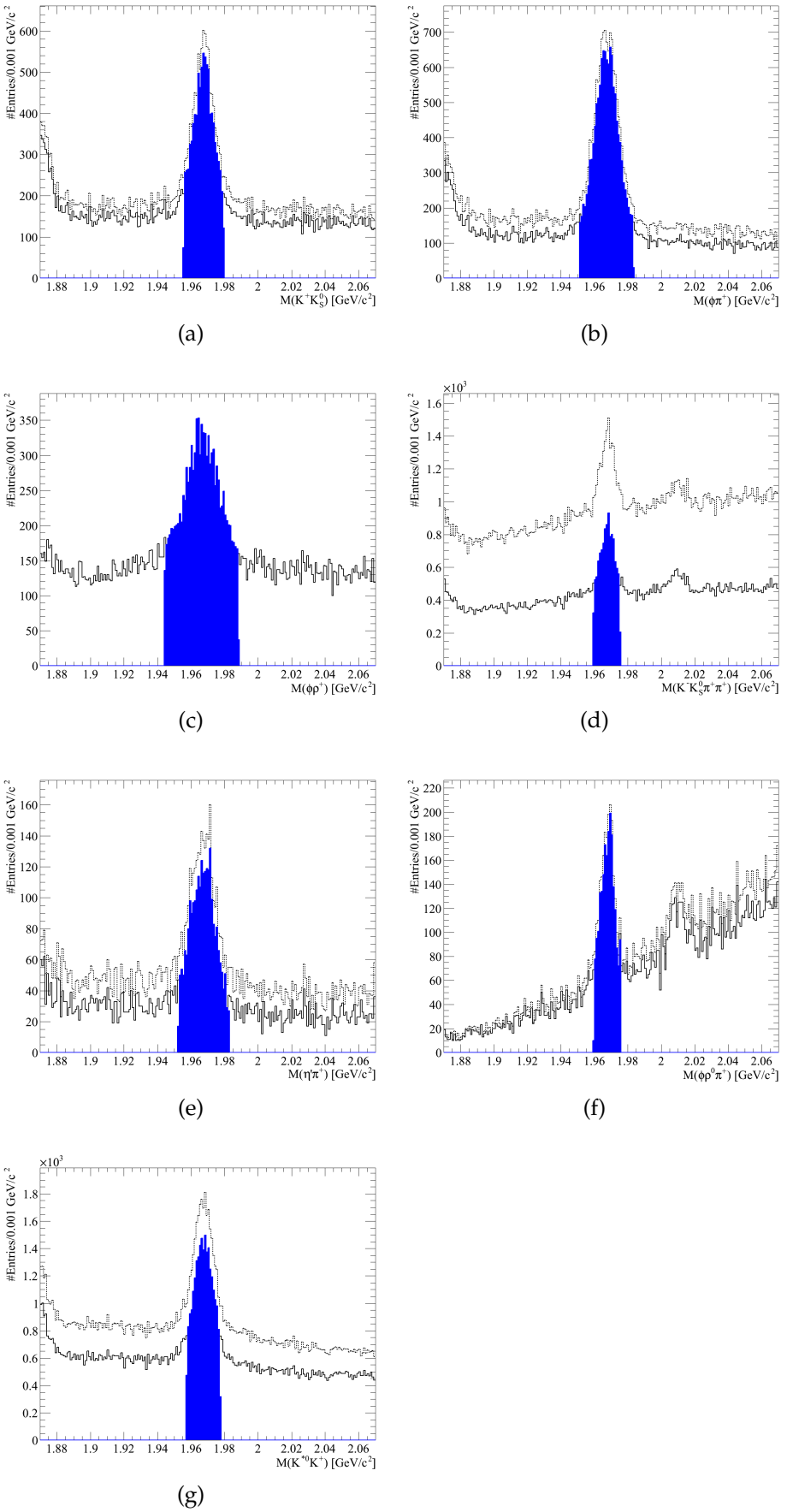

Figure 4.4: Mass distributions for the 7 D_s^+ tag modes. The dashed line represents the distribution after the initial skim. The solid line represents the distribution with all optimised cuts, apart from the mass window cut, applied. The final mass distribution is shown in blue, after all optimised cuts had been applied.

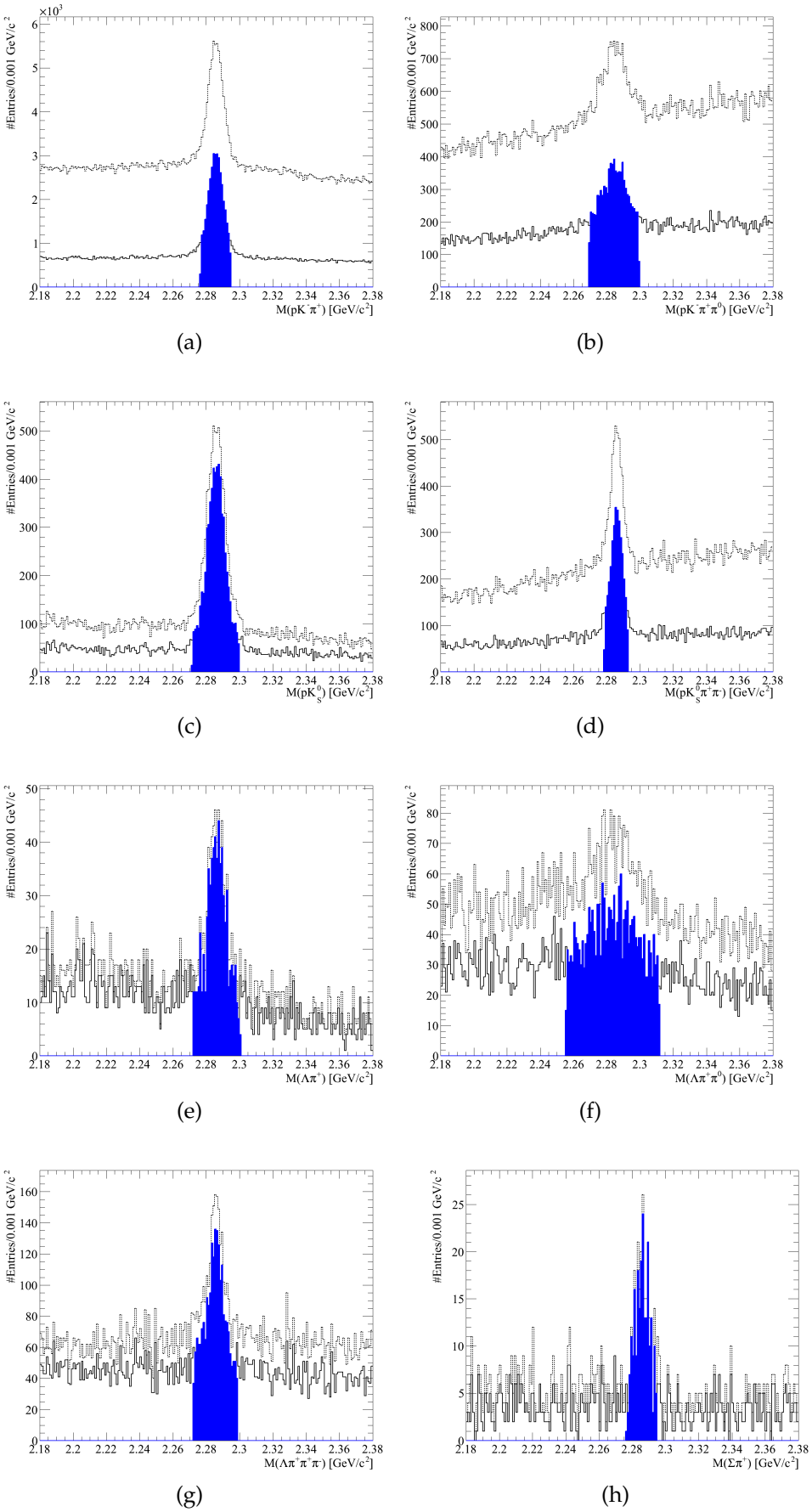

Figure 4.5: Mass distributions for the 8 Λ_c tag modes. The dashed line represents the distribution after the initial skim. The solid line represents the distribution with all optimised cuts, apart from the mass window cut, applied. The final mass distribution is shown in blue, after all optimised cuts had been applied.

Chapter 5

Analysis Method

5.1 Overview

The aim of the analysis was to obtain a value for the decay constant of the D^+ meson (f_{D^+}) by measuring the $D^+ \to \mu^+\nu$ decay rate. The decay chain $D^{*+} \to D^+\pi^0$, where $D^+ \to \mu^+\nu$, was reconstructed. The signal variable used was ΔM, the mass difference between the reconstructed D^{*+} and D^+ candidates, i.e. $\Delta M = M_{D^{*+}} - M_{D^+}$. Correctly reconstructed signal candidates produced a peak at $\approx 0.140\ GeV/c^2$ in ΔM, whereas background candidates produced a relatively flat and smooth distribution over the same region. The normalisation decay mode $D^{*+} \to D^+ \to \pi^+ K_L^0$ was also measured in order to test the reconstruction procedure. This normalisation mode was chosen because its branching fraction has been measured to relatively high precision: $BF(D^+ \to \pi^+ K_L^0) = (1.46 \pm 0.05) \times 10^{-2}$ [2]. The detection efficiency for K_L^0 mesons at *BABAR* is low, therefore the topology of the normalisation decay mode can be considered to be analogous to that of signal decay mode. The muon and neutrino in the signal decay mode are replaced by the pion and the K_L^0 in the normalisation decay mode.

Three possible methods could have been chosen to reconstruct the signal decay chain. The options were: a tagging approach, a *whole-event approach* [41], and a *half-hemisphere approach* [42].

The concept of tagging has already been introduced in section 4.4, and so will not be discussed here.

In the whole-event method, the four-momentum of all the particles in the event is used to determine the missing momentum of the event. All charged particles, neutral particles, and particles that can travel a measurable distance from the IR before decaying, are taken into account. The missing momentum and missing energy of the event can then be defined using:

$$\mathbf{p}_{miss} = -\sum \mathbf{p}_i \tag{5.1}$$

and

$$E_{miss} = 2E_{beam} - \sum E_i \tag{5.2}$$

where $\mathbf{p_i}$ and E_i indicate the momentum and energy of the i^{th} particle in the event, and E_{beam} represents the beam energy.

In the half-hemisphere method, each event is divided into two hemispheres, where the boundary between the hemispheres is defined by the plane perpendicular to the thrust axis of the event. The four-momentum of the neutrino candidate is then estimated using the missing four-momentum of the hemisphere that contains the muon candidate.

The half-hemisphere method was used by a CLEO analysis that reconstructed the decay chain $D_s^{*+} \rightarrow D_s^+\gamma$, $D_s^+ \rightarrow \mu^+\nu$ [42]. The missing momentum, $\mathbf{p}_{miss}$, and missing energy, E_{miss}, for the half-hemisphere were defined as:

$$\mathbf{p}_{miss} = \mathbf{p}_{thrust} - \sum \mathbf{p}_i \tag{5.3}$$

and

$$E_{miss} = E_{beam} - \sum E_i \tag{5.4}$$

where, again, E_{beam} represented the beam energy, the sums over E_i and $\mathbf{p}_i$ represented the total energy and total momentum of all pions, kaons and protons in the event, and the thrust momentum was given by $\mathbf{p}_{thrust}$. The thrust axis of the event was used to determine the direction of $\mathbf{p}_{thrust}$. The magnitude of $\mathbf{p}_{thrust}$ was found using $|\mathbf{p}_{thrust}^2| = E_{beam}^2 - m_{jet}^2$, where m_{jet} represented the *average charm-jet mass*. To

determine m_{jet}, a MC sample that contained $D^{*+} \to \pi^+ D^0$, $D^0 \to K^-\pi^+$ decays was used, where, to mimic the neutrino from the D_s^+ decay, all momentum and energy measurements for the pion from the D^0 decay were ignored during candidate reconstruction. Using this D^{*+} sample, m_{jet} was found to be $3.2\ GeV/c^2$. A muon candidate was combined with the neutrino candidate to form a D_s^+ candidate, and the D_s^+ candidate was then combined with a γ candidate to make a D_s^{*+} candidate. Signal events were searched for in ΔM, which was defined as: $\Delta M = M(\gamma\mu^+\nu) - M(\mu^+\nu)$. The analysis found that the half-hemisphere method resulted in around a factor of two increase in signal efficiency compared to the whole event method. Such an increase is not surprising because the whole event method is more affected by particle losses.

The tagging approach was not chosen for the present analysis because of its cost in terms of the $D^+ \to \mu^+\nu$ signal efficiency. A study of the whole- and half-hempishpere methods, in the context of $D^{*+} \to D^+\pi^0$, $D^+ \to \mu^+\nu$ decays, has been performed at CLEO [41]. In the study, the cm energy was (like the present analysis) equal to the mass of the $\Upsilon(4S)$. The study showed that the half-hemisphere method was more efficient than the whole event method. However, it also showed that the whole-event method resulted in a more accurate estimate of the missing momentum and a much better missing momentum resolution. It was for these reasons that the whole-event method was chosen for the present analysis.

This chapter discusses the various datasets used in the present analysis. The D^{*+} candidate reconstruction is described in detail, followed by the requirements placed upon the μ^+ candidate in the signal mode and the π^+ candidate in the normalisation mode. The requirements used to define the rest of the particles in the event are then described. Preliminary selection, and the most significant background contributions that survive it, are discussed. To reduce these background contributions several additional cuts were applied, some of which were optimised. These additional cuts, along with the optimisation procedure used, are described, and the final ΔM distributions are shown for the signal and nor-

malisation modes.

5.2 Datasets

In the present analysis, on- and off-peak data and on- and off-peak generic MC for runs 1 to 6 were used. (For more information regarding the on- and off-peak datasets, see section 4.3.) Dedicated MC samples were also used that contained $c\bar{c}$ events that were similar to those of the generic sample, except that the c quark was forced to become part of D^{*+}, which then decayed via either the signal mode or the normalisation mode. Thus, the dedicated samples were of the form $e^+e^- \rightarrow c\bar{c} \rightarrow D^{*+}X$, where X represented the rest of the event. The rest of the event contained a charm hadron and, usually, several fragmentation particles. The D^{*+} meson was then forced to decay $D^{*+} \rightarrow D^+\pi^0$, and the D^+ was forced to decay into either $D^+ \rightarrow \mu^+\nu$ or $D^+ \rightarrow \pi^+K^0_L$.

Tables 5.1 and 5.2 show the numbers of data and MC events, and for data the integrated luminosities, for each on and off-peak dataset and run period. The luminosity scaling factor for the i^{th} generic MC sample, $\mathcal{L}_i^{SF}$, can be calculated for each on and off-peak dataset and run period using the relation $\mathcal{L}_i^{SF} = \frac{N_i^{MC}}{N_i^{Data}}$, where N_i^{Data} and N_i^{MC} are the numbers of data and MC events. Each N_i^{Data} is given by $N_i^{Data} = \mathcal{L}\sigma_i$, where $\mathcal{L}$ is either the on or off-peak run luminosity, and σ_i is the cross-section for the i^{th} generic $f\bar{f}$ process, listed in table 3.1. The luminosity scaling factors for each MC dataset and run are given in table 5.3, where the combined $B^0\overline{B}^0$ and B^+B^- cross-section is taken to be equal to that of $b\bar{b}$.

5.3 D^{*+} Candidate Reconstruction

The signal decay chain that was reconstructed in this analysis was: $D^{*+} \rightarrow D^+\pi^0$, where $D^+ \rightarrow \mu^+\nu$. The normalisation decay mode of $D^{*+} \rightarrow D^+\pi^0$, where $D^+ \rightarrow \pi^+K^0_L$, was reconstructed in an analogous manner. Thus, the description of the signal mode reconstruction also serves to describe that of the normalisation mode, and any exceptions are stated explicitly.

Data	Peak Type	Run1	Run2	Run3	Run4	Run5	Run6	Total
Events	On	0.293	0.959	0.501	1.59	2.10	1.26	6.71
$\times 10^9$	Off	0.0338	0.101	0.0352	0.149	0.208	0.115	0.643
	Both	0.327	1.06	0.536	1.74	2.31	1.38	7.36
Lumi.	On	20.8	61.6	32.5	102	135	79.5	432
fb^{-1}	Off	2.65	6.99	2.49	10.3	14.7	7.94	45.0
	Both	23.4	68.6	35.0	112	150	87.4	476

Table 5.1: The number of data events and the integrated luminosities recorded by *BABAR* and used in the present analysis. The numbers have been organised by peak type and run period.

MC Type	Peak Type	Run1	Run2	Run3	Run4	Run5	Run6	Total
$c\bar{c}$	On	55.3	164	88.3	267	344	209	1130
	Off	5.58	17.6	6.53	21.3	37.8	20.5	109
	Both	60.9	182	94.8	288	382	230	1240
B^+B^-	On	34.9	105	56.0	167	214	130	707
$B^0\overline{B}^0$	On	34.9	103	57.9	170	215	135	716
uds	On	161	452	276	422	554	327	2190
	Off	20.6	53.3	21.1	34.0	60.3	33.0	222
	Both	182	505	297	456	614	360	2410
$\tau^+\tau^-$	On	49.3	157	59.3	180	237	140	822
	Off	6.86	21.4	4.50	14.5	25.8	14.1	87.1
	Both	56.2	178	63.8	194	263	154	909
$D^+ \to \mu^+\nu$	On	0.0400	0.113	0.0530	0.203	0.267	0.156	0.832
$D^- \to \mu^-\bar{\nu}$	On	0.0400	0.113	0.0660	0.203	0.267	0.156	0.845
$D^+ \to \pi^+K_L^0$	On	0.0430	0.121	0.0660	0.203	0.267	0.156	0.856
$D^- \to \pi^-K_L^0$	On	0.0430	0.121	0.0660	0.203	0.259	0.156	0.848

Table 5.2: The number of MC events, in millions, that were used in the present analysis. The numbers have been organised by peak type and run period.

MC Type	Peak Type	Run1	Run2	Run3	Run4	Run5	Run6	Total
$c\bar{c}$	On	2.04	2.05	2.09	2.02	1.96	2.02	2.01
	Off	1.62	1.93	2.02	1.59	1.98	1.99	1.87
	Both	2.00	2.04	2.08	1.98	1.96	2.02	2.00
B^+B^-	On	3.19	3.24	3.28	3.13	3.03	3.12	3.13
	Off	0.00	0.00	0.00	0.00	0.00	0.00	0.00
	Both	2.83	2.91	3.05	2.84	2.73	2.84	2.83
$B^0\overline{B}^0$	On	3.20	3.19	3.39	3.18	3.04	3.24	3.17
	Off	0.00	0.00	0.00	0.00	0.00	0.00	0.00
	Both	2.84	2.87	3.15	2.89	2.74	2.94	2.87
uds	On	3.69	3.51	4.06	1.98	1.96	1.97	2.43
	Off	3.72	3.65	4.06	1.58	1.97	1.98	2.36
	Both	3.70	3.52	4.06	1.95	1.96	1.97	2.42
$\tau^+\tau^-$	On	2.52	2.70	1.94	1.88	1.87	1.87	2.03
	Off	2.75	3.26	1.92	1.50	1.87	1.88	2.06
	Both	2.55	2.76	1.94	1.85	1.87	1.87	2.03

Table 5.3: The luminosity scaling factors for the various generic MC sub-samples used in the present analysis. The numbers have been arranged by peak type and run period.

.

Reconstruction of a D^{*+} candidate began by taking a suitable μ^+ candidate from the event. The neutrino passed straight through the *BABAR* detector, and so its presence had to be inferred using a *missing-mass*, MM, candidate, whose four-momentum, P_{miss}, was equal to the missing four-momentum of the event. The missing four-momentum was determined using the equation: $P_{miss} = P_{beams} - P_{visible}$, where P_{beams} was the combined four-momentum of the e^+e^- beams and $P_{visible}$ was the combined four-momentum of all the particles detected in the event.

To find $P_{visible}$, the four-momentum of all particles in the event were added together according to a simple prescription. The prescription was necessary because, in the computing framework of *BABAR*, a particle could be consistent with the requirements of several particle type hypotheses, and so be used many times. For example, in a given event, the same particle could be listed as a pion, a proton, a pion that was the daughter of one (or many) K^0_S candidates, etc. All manifestations of the same particle in an event were said to *overlap* with one another. In order to avoid adding the four-momentum of the same particle more than once, candidate four-momenta were added in a specific order, and a check was performed before adding the four-momentum of a candidate to make sure that that candidate did not overlap with any candidate whose four-momentum had already been added. Starting with the four-momentum of the μ^+candidate, or, for the nor-

malisation decay mode, the π^+ candidate, the four-momentum of each K^0_S candidate in the event was added. Then, the four-momenta of all Λ candidates were added, followed by that of all photon conversion (i.e. $\gamma \to e^+e^-$) candidates, charged track candidates, π^0 candidates, and finally photon candidates. The selection criteria that were used for each type of candidate particle are given in section 5.4.

After P_{miss} had been determined, the μ^+ candidate was combined with the MM candidate to create a D^+ candidate, and a D^{*+} candidate was formed by combining the D^+ candidate with a π^0 candidate. A *rest-of-event* (ROE) candidate was then created by summing over the visible four-momenta of all the candidates in the event that were not part of the D^{*+} candidate.

The ROE and D^{*+} candidates were combined to form a nominal $\Upsilon(4S)$ candidate, which was fitted, subject to several constraints, using a standard *BABAR* fitting algorithm (called `TreeFitter`). The missing mass was constrained to $0\ GeV/c^2$ for the signal mode, and to the nominal mass of the K^0_L for the normalisation mode. The mass of the D^+ candidate was also constrained to its nominal value. The overall energy of the event was constrained to the energy of the beams, and the position of the $\Upsilon(4S)$ candidate's point of origin was constrained to lie within a region defined by the beam-spot. After the fit, the information pertaining to the D^{*+} candidate was stored, and the entire candidate reconstruction was repeated for all suitable (μ^+, π^0) candidate combinations that remained within the event. This method of reconstruction led to high candidate multiplicities in events because, in general, many π^0 candidates were found.

5.4 Particle Selection Requirements

5.4.1 The Signal Muon

Signal muon candidates were identified using a data classification technique based upon *decision trees*. A decision tree is a data classification algorithm that uses successive binary cuts to split a dataset into signal and background components based on a *figure of merit* (FOM). The algorithm takes an input dataset containing unknown fractions of signal and background events, which can be viewed in N dimensions. An initial binary cut, or *decision node*, is chosen based upon the dimension that, when probed, produces the best FOM result. The initial decision node produces two subsets of the data. The procedure

is then repeated to find a decision node for each of the data subsets by searching in the remaining $N - 1$ dimensions, and so on. If the FOM result of a parent decision node cannot be bettered by both of its daughter nodes, then the parent node becomes a either a *terminal signal node* or a *terminal background node*, depending on whether it contains more signal or background events. Ultimately, the algorithm creates a tree-like structure of decision nodes and terminal nodes. There are many different FOM possibilities to chose from, but the one chosen for muon identification was the *Gini index*, G, where $G = -2p(1-p)$, and p is the fraction of events within the node that were identified correctly.

The selector used to identify signal muon candidates was `muBDTVeryTightFakeRate`. This selector was created using *Bagger Decision Trees* (BDTs) [43] that were trained using a dataset that comprised muon signal events and pion background events. The muon sample came from $e^+e^- \to \mu^+\mu^-\gamma$ events, and the pion events were taken from $e^+e^- \to \tau^+\tau^-$ decays, in which one τ decayed leptonically while the other decayed to 3 pions and a neutrino. Using a number of decision trees that had each been trained using a random subset of events from the main dataset, an unidentified track was deemed to be either a muon or a pion by using the most common classification outcome. A total of 30 classification variables were used during the training of each decision tree: 3 from the DCH, 5 from the DIRC, 10 from the EMC and 8 from the IFR. The remaining 4 variables were the date on which the track was recorded, as well as its charge, momentum and polar angle.

Figures 5.1 and 5.2 show the muon identification efficiency and the probability of mis-identifying a pion as a muon, both as a function of momentum, for run 6 data and MC. The mis-identification probabilities for kaons and protons were very low, and so are not shown. The figures show a good agreement between data and MC from around $1.5\ GeV/c$ to $4.0\ GeV/c$. In the same momentum range, the muon selection efficiency is stable at around 80%, and the rate of pion mis-identification is around 1%. Also, the shapes of the distributions are unaffected by the charge of the particle involved.

5.4.2 The Normalisation Mode Pion

A KM selector was used to identify π^+ candidates as part of the normalisation mode reconstruction. Named after its original developer, Kalanand Mishra, the selector was

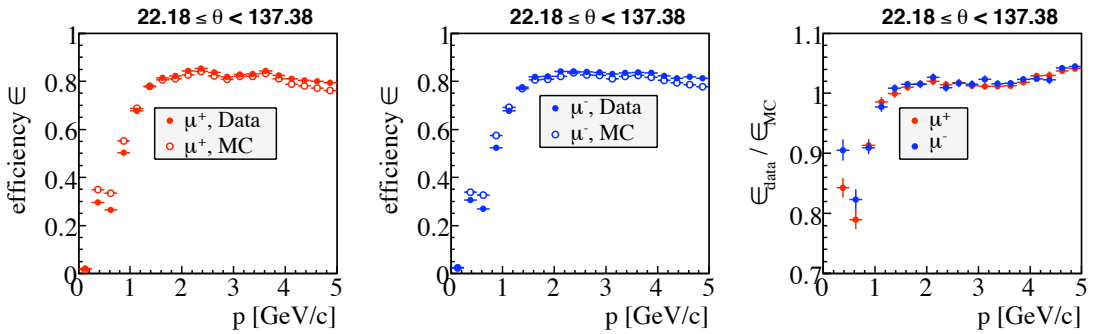

Figure 5.1: Muon selection efficiency as a function of momentum for the `muBDTVeryTightFakeRate` selector [44]. The left-hand and centre graphs show distributions of MC overlaid with data for positively charged and negatively charged muons. The right-hand distribution shows the ratio of data to MC efficiencies. The polar angle for each track, θ, had to lie within the range indicated.

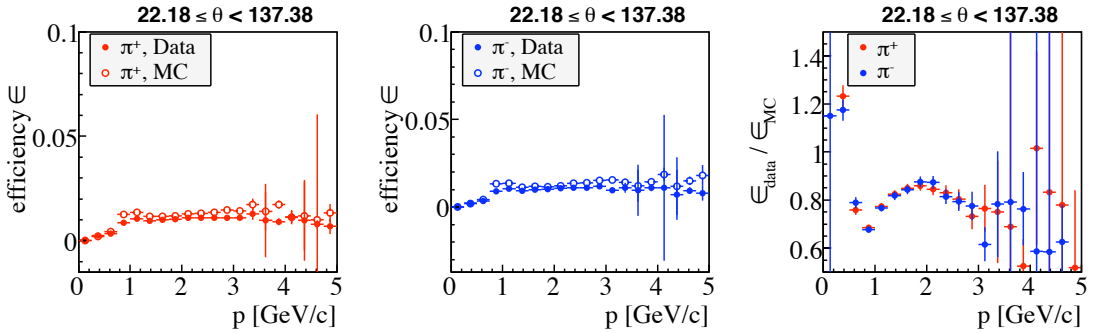

Figure 5.2: Pion mis-identification rate as a function of momentum for the `muBDTVeryTightFakeRate` selector [44]. The left-hand and centre graphs show distributions of MC overlaid with data for positively charged and negatively charged pions. The right-hand distribution shows the ratio of data and MC efficiencies. The polar angle for each track, θ, had to lie within the range indicated.

based on an Error Correction Output Code (ECOC) Multiclass classifier [45] that combined the results of 7 different BDT classifiers. For a given track, the multiclass classifier produced a numerical result between 0 and 1 which indicated how compatible that track was with each of the following hypotheses: kaon, pion, proton and electron. (The muon particle hypothesis was not considered because only variables that related to the inner detector, and not the IFR, were used during the training of the BDTs.) Table 5.4 [46] shows the link between each of the 7 BDT classifiers and each of the charged particle hypotheses. In each column of the table, the numbers 1 and -1 show whether the corresponding particle type was regarded as either signal or background during the training of that BDT. Given an unidentified charged track, the multiclass classifier would produce

Class	BDT 0	BDT 1	BDT 2	BDT 3	BDT 4	BDT 5	BDT 6
K	1	1	1	1	1	1	1
π	-1	1	-1	1	-1	1	-1
p	1	-1	-1	1	1	-1	-1
e	1	1	1	-1	-1	-1	-1

Table 5.4: This table shows how each of the 7 BDT classifiers, labelled from 0 to 6, regarded each type of particle during training. The numbers 1 and -1 indicate whether that particle class was treated as either signal or background.

Class	BDT 0	BDT 1	BDT 2	BDT 3	BDT 4	BDT 5	BDT 6	Distance
$Track$	1.0	0.0	0.0	0.5	0.0	0.0	-0.5	-
K	1	1	1	1	1	1	1	6.5
π	-1	1	-1	1	-1	1	-1	8.5
p	1	-1	-1	1	1	-1	-1	4.5
e	1	1	1	-1	-1	-1	-1	6.5

Table 5.5: This table is an extension of table 5.4, and shows the distance results for an unidentified track. The track's BDT results are shown on the first row. By combining these results with training values of each particle class in turn, a distance result can be calculated using the method described in the text.

a string of 7 BDT results, all of which were real numbers between -1 and 1. How compatible the track was with each of the particle hypotheses was determined by finding the *distance* of the track from each of the hypotheses. For a given particle hypothesis, the distance was found by summing the squares of the differences between each BDT result and its corresponding training value. For example, if the string of results from each of the 7 classifiers was (1.0,0.0,0.0,0.5,0.0,0.0,-0.5), then table 5.5 shows the distance results for the track. Of the four distance results for the track, the shortest is 4.5, which suggests that the track was probably made by a proton.

Selection criteria were formed based upon the distance values from each of the four particle hypotheses, labeled: D_π, D_K, D_p and D_e. Using the pion hypothesis as an example, selection criteria could be loosened or tightened based upon the following quantities: D_π, D_K/D_π, D_p/D_π and D_e/D_π [46].

The classifier was trained to identify pions using a sample of events that contained $D^{*+} \to D^0\pi_s^+$, $D^0 \to \pi^+K^-$ candidates, where π_s^+ indicates a *slow* pion. (Slow pions were only used in the D^{*+} candidate reconstruction; they were not used for training.) Each of the 7 BDT classifiers had 36 input variables which included the track's momentum, charge and azimuthal and polar angles, and the Gini index was used as the FOM.

Figures 5.3 and 5.4 show the pion identification efficiency and the rate of mis-identifying a muon as a pion, both as a function of momentum, for run 6 data and MC. The mis-identification rates for kaons and protons were very low, and so are not shown. Figure 5.3 shows a good agreement between shapes of the data and MC momentum distributions; however the efficiency for data is slightly greater than that of the MC. Conversely, figure 5.4 shows that the mis-identification probability for muons as pions is slightly lower for data than for MC, although again, the shapes of the distributions are similar. While the selection efficiency for pions shows relatively large variations across the entire momentum range, the rate of muon mis-identification remains stable above 1 GeV/c at around 35%. The shapes of the distributions are unaffected by the charge of the particle involved.

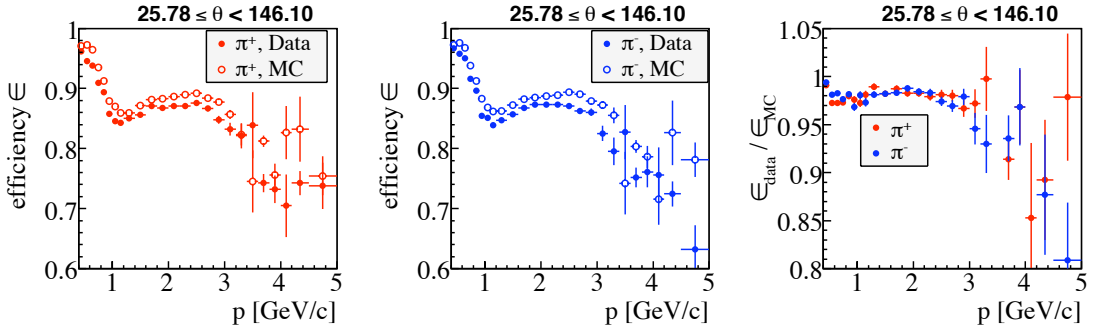

Figure 5.3: Pion selection efficiency as a function of momentum for the `piKMSuperTight` selector [44]. The left-hand and centre graphs show distributions of MC overlaid with data for positively charged and negatively charged pions. The right-hand distribution shows the ratio of data and MC efficiencies. The polar angle for each track, θ, had to lie within the range indicated.

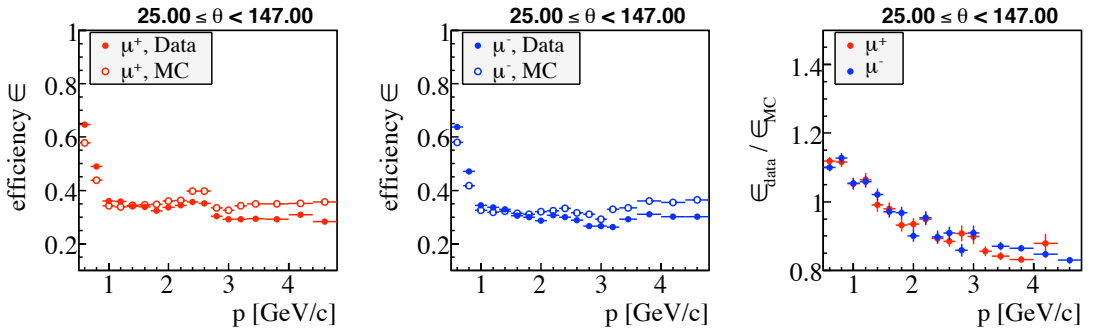

Figure 5.4: Muon mis-identification probability as a function of momentum for the `piKMSuperTight` selector [44]. The left-hand and centre graphs show distributions of MC overlaid with data for positively charged and negatively charged muons. The right-hand distribution shows the ratio of data and MC efficiencies. The polar angle for each track, θ, had to lie within the range indicated.

5.4.3 Other Particles

This section describes how candidates, other than the signal mode muon or the normalisation mode pion, were defined in an event. All charged tracks and neutral clusters were used in an event. Every charged track underwent some form of particle identification to see which type of charged particle it was most compatible with (i.e. proton, kaon, muon, electron or pion). Three types of particle that could have had decay vertices an appreciable distance from the IP were considered: the K^0_S, the Λ and photon conversions (i.e. $\gamma \to e^+e^-$). The remaining particles that were looked for were the π^0 and the photon. The criteria that were used to define candidates for each of the particle types are discussed in detail below. Unless otherwise stated, all of the numerical values given below were taken from reference [47].

Each candidate π^0 came from the `pi0Loose` list, and was created by adding the four-momenta of a pair of photons. Each of the photons had to have a lab energy between $30\,MeV$ and $10\,GeV$, and the electromagnetic shower of each photon had to have a lateral moment between 0 and 0.8. The lateral moment, LAT, was a way of parameterising the shape of the electromagnetic shower that the photon produced, in the transverse plane. Equation 5.5 defines the LAT [48]:

$$LAT = \frac{\sum_{i=3}^{N} E_i r_i^2}{\sum_{i=1}^{N} E_i r^2} \tag{5.5}$$

Here, E_i is the energy deposit of the i^{th} crystal in the cluster, r_i is the distance of that crystal from the centre of the cluster and r is the characteristic length of a calorimeter crystal ($\approx 5cm$). In equation 5.5, the sum in the numerator ignored the two crystals that contained the highest energy deposits, while the sum in the denominator did not. The LAT variable provided an means of separating showers caused by photons and electrons, which tended to deposit most of their energy in one or two crystals, from those caused by hadrons, which tended to deposit their energy more evenly throughout the crystals. The π^0 candidate had to have a mass, $M_{\gamma\gamma}$, in the range $(110 < M_{\gamma\gamma} < 160)\ MeV/c^2$, and a lab energy between $200\,MeV$ and $10\,GeV$

The list that provided K_S meson candidates was `KsTight`, and it held $K_S \to \pi^+\pi^-$ candidates that were formed by combining the four-momenta of pairs of charged tracks.

Each track was given the pion mass hypothesis, and (at the point of closest approach for the tracks) the invariant mass of the pair, $M_{\pi^+\pi^-}$, had to lie in the range $(450.0 < M_{\pi^+\pi^-} < 550.0)\ MeV/c^2$. Using both the position and momentum information of the tracks, a fit was performed to create the K_S candidate. A standard *BABAR* fitting algorithm called `TreeFitter` was used, and after the fit $M_{\pi^+\pi^-}$ had to lie in the narrower mass range $(473 < M_{\pi^+\pi^-} < 523)\ MeV/c^2$. The fit was then performed again, this time with an additional constraint that forced the point of origin of the K_S candidate to be the beam-spot. The probability of χ^2 result from both fits had to be greater than or equal to 10^{-3}. A cut was also placed on the minimum flight significance, FS, of the K_S candidate of 3, where FS was measured from the beam-spot, and given by $FS = FL/\sigma_{FL}$, and FL and σ_{FL} were the measured flight length and flight length error for the particle.

The Λ list, `LambdaTight`, held $\Lambda \to p\pi^-$ candidates formed by combining pairs of charged tracks that were used as p and π^- candidates. For suitable candidates, the invariant mass of the Λ candidate had to lie within $10\ MeV/c^2$ of the nominal Λ mass. Candidates also had to have an invariant mass (when measured at the point of closest approach for the tracks) that lay within $30\ MeV/c^2$ of the nominal Λ mass. A fit using the candidates position and momentum was made, and the resulting probability of the χ^2 for the fit had to be above 10^{-3}. This fit was performed again, with an additional beam-spot constraint placed on the Λ candidate's point of origin, and again the resulting probability of the χ^2 for the fit had to be above 10^{-3}. Candidate Λs also had to have a minimum flight significance of 3.

A photon conversion list called `gammaConversionDefault` held $\gamma \to e^+e^-$ candidates, which were, again, formed using pairs of charged tracks. The full reconstruction, which is given in reference [47], was quite involved, and so only the basic procedure is given here. Pairs of electron candidates were combined to form a photon candidate, which was then fitted, and only those fits that returned a successful vertex result were kept. Prior to the fit, the photon candidate had to have a mass below $500\ MeV$, and following the fit it had to have a mass below $30\ MeV$.

All charged track candidates came from the list `ChargedTracks` and were subject only to the requirement that they have a non-zero charge. The mass of each charged track candidate was decided based on the outcome of a set of particle identification selectors, listed in table 5.6. If a candidate passed multiple selectors then the selector with the

Priority	Particle Type	Selector Name
5	e	`eKMVeryTight`
4	p	`pKMVeryTight`
3	μ	`muBDTVeryTight`
2	K	`kaonBDTVeryTight`
1	π	*None*

Table 5.6: This table shows the selectors that were used in the identification of charged particles in an event. If a charged track satisfied two or more selectors, then the selector with the highest priority value was chosen. The KM and BDT selectors are described in sections 5.4.1 and 5.4.2.

highest priority value would be chosen. The order of priority was chosen based upon the mis-identification probabilities of each of the selectors. For example, the election selector was given the highest priority because it was far less likely to mis-identify a charged particle than any of the other selectors.

Neutral candidates were supplied by the `GoodPhotonLoose` list, which contained neutral candidates that were not associated with any track candidate and had a single EMC bump. The candidates were assigned a mass hypothesis of $0\ MeV/c^2$, had to have a minimum lab energy of $30\ MeV$, and a maximum associated lateral moment of 0.8. Each candidate was also checked to make sure that it was at least $15\ cm$ away from any other EMC hit. This isolation check helped to reject fake neutral candidates that came coming from *split-offs*, i.e. hits caused by particles that had interacted with either the calorimeter or any material in front of the calorimeter.

5.5 Preliminary Selection of D^{*+} Candidates

Preliminary selection comprised a set of basic, loose cuts that were aimed at reducing background candidate reconstructions. The cuts chosen were either reasonable physics cuts, or cuts based on the kinematic properties of the signal decay mode, $D^+ \to \mu^+\nu$. Preliminary candidate selection helped to speed up the event processing time, as well as reduce the amount of disk space used for the analysis. Each of the preliminary cuts is introduced below, in the context of the signal decay chain; $D^{*+} \to D^+\pi^0$, where $D^+ \to \mu^+\nu$. The normalisation mode decay chain, $D^{*+} \to D^+\pi^0$, where $D^+ \to \pi^+K^0_L$, was subject to the analogous cuts (i.e. the K_L took the place of the ν and the π^+ took the place of the μ^+), unless otherwise stated.

There were two cuts on properties of the event itself. The first event requirement was

that the event had to pass a preliminary background filter, called `BGFMultiHadron`. (The `BGFMultiHadron` cut was a standard cut used in *BABAR* analyses and was actually implemented before the pre-selection stage.) To pass the filter, the event had to contain a minimum number of two charged tracks and have an $R2$ value below 0.98, where $R2$ was equal to the ratio of the second Fox-Wolfram moment, H_2, to the zeroth, H_0. The Fox-Wolfram moments, H_l, are defined in equation 5.6 [49]:

$$H_l = \sum_{i,j} \frac{|\mathbf{p_i}||\mathbf{p}_j|}{E_{cm}^2} P_l(cos\phi_{ij}) \tag{5.6}$$

Here, the subscripts i and j run over all hadrons in an event, E_{cm} is the centre-of-mass energy, P_l are the Legendre polynomials and ϕ_{ij} represents the angle between the i^{th} and j^{th} hadrons. The cut was designed to remove high momentum, back-to-back, leptonic events, for which $R2$ approached 1. The second event requirement was that the sum of the charges of all the particles in the event was zero, i.e. the event was charge neutral. While this requirement did not guarantee that every charged particle had been detected, it was useful in removing those events in which one or more charged particles were missing, which would lead to an incorrect missing mass for each candidate in the event.

All of the remaining preliminary cuts applied to the signal candidates within the event, rather than to the event itself. For the signal mode, every muon candidate had to satisfy the selector `muBDTVeryTightFakeRate`, and for the normalisation mode every pion had to satisfy `piKMSuperTight`. Of the recommended selectors for muons and pions, these were the most stringent, and were chosen to help reduce the high numbers of potential signal tracks in an event.

Signal muon candidates had to have a cm momentum, $P_{\mu cm}$, prior to the vertex fit, in the range $(1.3 < P_{\mu^+ cm} < 4.0)\ GeV/c$. This requirement was taken from a $D^+ \to \mu^+\nu$ analysis performed at CLEO [41]. The low $P_{\mu^+ cm}$ limit came from requiring that the muon candidate had penetrated a minimum of 5 interaction lengths of material, and the high $P_{\mu^+ cm}$ limit came from the phase-space suppression of $D^+ \to \mu^+\nu$ decay. The pre-fit momentum of the D^+ candidate had to be at least $2.6\ GeV/c$. This is a standard cut in charm analyses, used to remove background D^+ candidates coming from B meson decays. The pre-fit D^+ candidate mass, M_{D^+}, had to lie in the range $(1.0 < M_{D^+} < 3.0)\ GeV/c^2$. The invariant mass of the photon pairs that formed the π^0 candidates, $M_{\gamma\gamma}$, was limited to the range $(120 < M_{\gamma\gamma} < 145)\ MeV/c^2$. The invariant mass of the system

formed by the μ^+ and π^0 candidates, $M_{\mu^+\pi^0}$, had to lie within the range $(450 < M_{\mu^+\pi^0} < 650)\ MeV/c^2$. This kinematic constraint came from the fact that signal decay chain is composed of one two-bodied decay, followed by another. The calculation of the nominal kinematic limits, based upon particle masses given in reference [2], is given in appendix A for both the signal and normalisation decay modes. The kinematic fit applied to each candidate had to be successful, and have a resulting chi-square probability, $P(\chi^2)$, that satisfied $log(P(\chi^2)) > -5$.

Of the numbers of events in the initial input datasets, the numbers of data and MC candidates passing all the above selection criteria and their respective selection efficiencies are given in table 5.7.

After the preliminary selection criteria had been applied to the candidates, several properties of the $D^+ \to \mu^+\nu$ and $D^+ \to \pi^+K^0_L$ candidates were investigated using the dedicated signal MC samples. The resulting plots are shown in figures 5.5 and 5.6, where the left- and right-hand columns show distributions for the $D^+ \to \mu^+\nu$ and $D^+ \to \pi^+K^0_L$ candidates, respectively. The plots are directly analogous to those found in reference [41]. Note that those distributions that are labeled *raw* show the output obtained without using the fit to the D^{*+} candidate. Figures 5.5a and 5.5b show the *raw* missing mass squared, MM^2, distributions for the candidates. As expected, the peaks of the MM^2 distributions are centred around the nominal masses of the undetected particles; i.e. $\approx 0\ GeV^2/c^4$ for $D^+ \to \mu^+\nu$ candidates and $\approx 0.25\ GeV^2/c^4$ for $D^+ \to \pi^+K^0_L$ candidates. The distributions for the raw mass of the D^+ candidate, M_{D^+}, are given in figures 5.5c and 5.5d. For both the signal and normalisation modes, the distribution is broad and centred around the nominal D^+ mass. In each case, the large spread in M_{D^+} comes from assuming that the missing four-momentum of the event is equal to the four-momentum of the missing particle. Note, however, that ΔM is equal to the *difference* between two masses, and so the effect of this broad spread in M_{D^+} is somewhat mitigated. Figures 5.6a to 5.6f each show a pair of distributions; in all cases, the solid line represents the raw distribution and the dashed line represents the distribution after the D^{*+} candidate had been fitted. Figures 5.6a and 5.6b show the ΔM distributions. Distributions that show the angle made between the momentum vectors of the generated neutrino and the reconstructed neutrino candidate, $Angle(\nu_{Gen.}, \nu_{Reco.})$, are given in figures 5.6c and 5.6d. Figures 5.6e and 5.6f show the magnitude of the difference between the generated and

MC Type	Peak Type	Run1	Run2	Run3	Run4	Run5	Run6	Total
Data	On	0.293 245	0.959 753	0.501 407	1.59 1305	2.1 2163	1.26 1527	6.71 6400
	Off	0.0338 26	0.101 79	0.0352 26	0.149 135	0.208 227	0.115 166	0.643 659
	Both	0.327 271	1.06 832	0.536 433	1.74 1440	2.31 2390	1.38 1693	7.36 7059
$c\bar{c}$	On	55.3 249	164 744	88.3 487	267 1315	344 1648	209 1131	1130 5574
	Off	5.58 19	17.6 84	6.53 34	21.3 114	37.8 171	20.5 121	109 543
	Both	60.8 268	182 828	94.9 521	289 1429	381 1819	229 1252	1240 6117
B^+B^-	On	34.9 29	105 87	56 31	167 162	214 164	130 122	707 595
$B^0\overline{B}^0$	On	34.9 13	103 45	57.9 20	170 79	215 88	135 70	716 315
uds	On	161 585	452 1897	276 1187	422 1797	554 2293	327 1251	2190 9010
	Off	20.6 76	53.3 235	21.1 70	34 155	60.3 223	33 129	222 888
	Both	181 661	505 2132	297 1257	456 1952	614 2516	360 1380	2410 9898
$\tau^+\tau^-$	On	49.3 37	157 177	59.3 59	180 245	237 330	140 237	822 1085
	Off	6.86 4	21.4 33	4.5 5	14.5 20	25.8 19	14.1 21	87.1 102
	Both	56.2 41	178 210	63.8 64	195 265	263 349	154 258	909 1187
$D^+ \to \mu^+\nu$	On	0.04 189	0.113 623	0.053 319	0.203 1114	0.267 1573	0.156 942	0.832 4760
$D^- \to \mu^-\bar{\nu}$	On	0.04 223	0.113 541	0.066 397	0.203 1135	0.267 1423	0.156 973	0.845 4692
$D^+ \to \pi^+K^0_L$	On	0.043 170	0.121 527	0.066 260	0.203 907	0.267 1079	0.156 655	0.856 3598
$D^- \to \pi^-K^0_L$	On	0.043 186	0.121 551	0.066 278	0.203 853	0.259 1041	0.156 589	0.848 3498

Table 5.7: Each entry in this table shows, for the various event samples, the initial number of either data events, $\times 10^9$, or MC events, $\times 10^6$, followed by the number of D^{*+} candidates that passed the preliminary selection requirements. The numbers have been arranged by peak type and run period.

.

reconstructed momentum of the D^+ candidate.

After the fit, there is a clear improvement in the resolution of ΔM for both the signal and normalisation modes. The fit improves the angular resolution of the reconstructed ν and K_L^0 candidates. The fit also improves the momentum resolution of the reconstructed D^+ candidate.

5.6 Signal and Background Contributions

Figures 5.7a and 5.7b show the ΔM distributions for the signal and normalisation decay modes after the preliminary candidate selection. The different colours indicate the various contributions from each of the MC samples, and for the $c\bar{c}$, $B^0\overline{B}^0$ and B^+B^- samples, those events that contained either the signal decay or the normalisation decay have been separated from the rest of the generic events. The number of candidates in each of the MC samples has been scaled to luminosity. Reconstructed data candidates, represented by crosses, have also been plotted.

For both the $D^+ \to \mu^+\nu$ and the $D^+ \to \pi^+K_L^0$ channels, figures 5.7a and 5.7b show that most of the signal and normalisation reconstructions came from $c\bar{c}$ events, although there were also a small number from $B^0\overline{B}^0$ and B^+B^- events in which one the daughters of the B meson was a D^+.

The ΔM distribution for both the signal and normalisation decay modes shows a large, peaking background contribution from $c\bar{c}$ events. Figures 5.8a and 5.8b show the various components of the $c\bar{c}$ background. For both decay channels, mis-reconstructed D^0, D^+ and D_s^+ decays provide the majority of the background candidates. For the $D^+ \to \mu^+\nu$ channel, the dominant background contribution came from hadronic D^0 decays, and a significant fraction of background candidates came from semi-leptonic decays of the D^+ and D^0. Leptonic decays of the D_s^+ and hadronic decays of the D^+ also contributed.

For the $D^+ \to \pi^+K_L^0$ channel the main background components came from mis-reconstructed D^0 and D^+ decays. Small contributions from hadronic D_s^+ decays, as well as mis-reconstructed fragmentation particles are also present, most of which were found to be either pions or ρ mesons.

The *other* category in figures 5.8a and 5.8b contains the sum of all of the smaller $c\bar{c}$ background contributions.

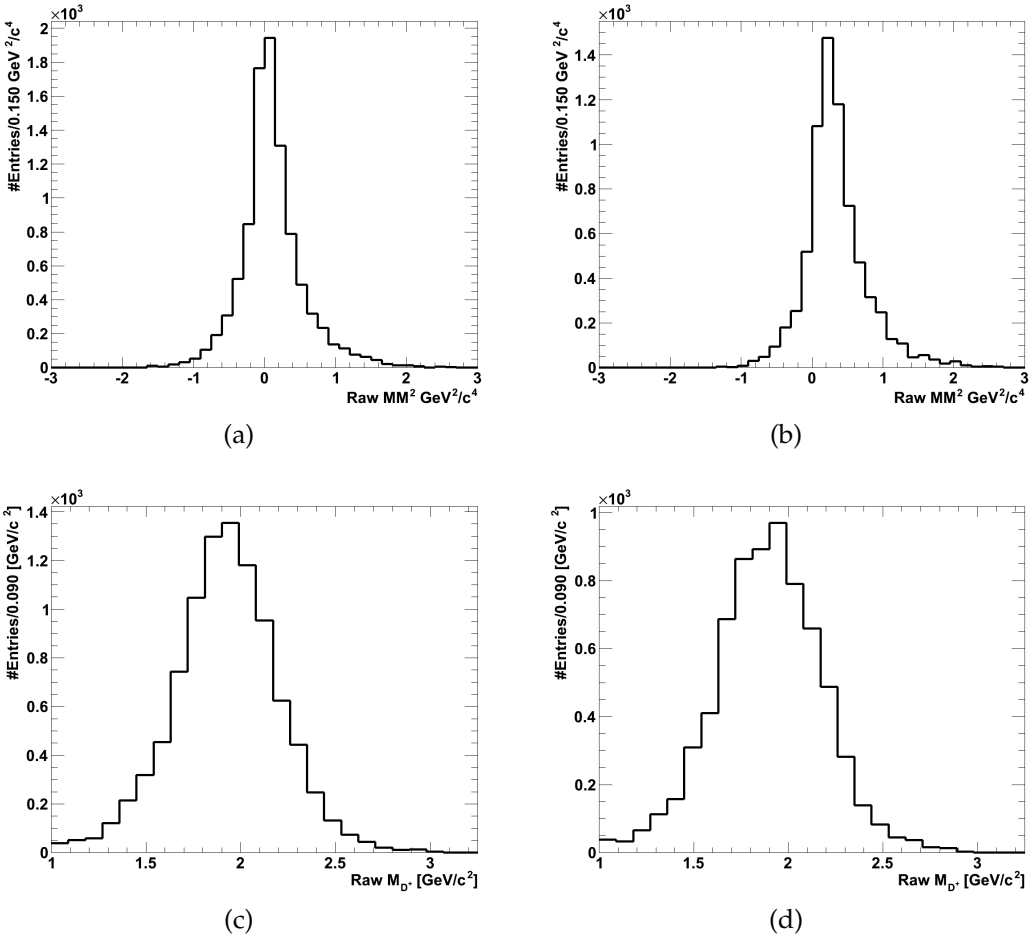

Figure 5.5: These plots show the raw MM^2 and raw M_{D^+} distributions for the reconstructed $D^+ \to \mu^+\nu$ and $D^+ \to \pi^+ K_L^0$ candidates after the preliminary selection cuts have been applied (and before the kinematic fit to the D^{*+} candidate). The plots in the left-hand column show distributions for the $D^+ \to \mu^+\nu$ mode and the plots in the right-hand column show distributions for the $D^+ \to \pi^+ K_L^0$ mode.

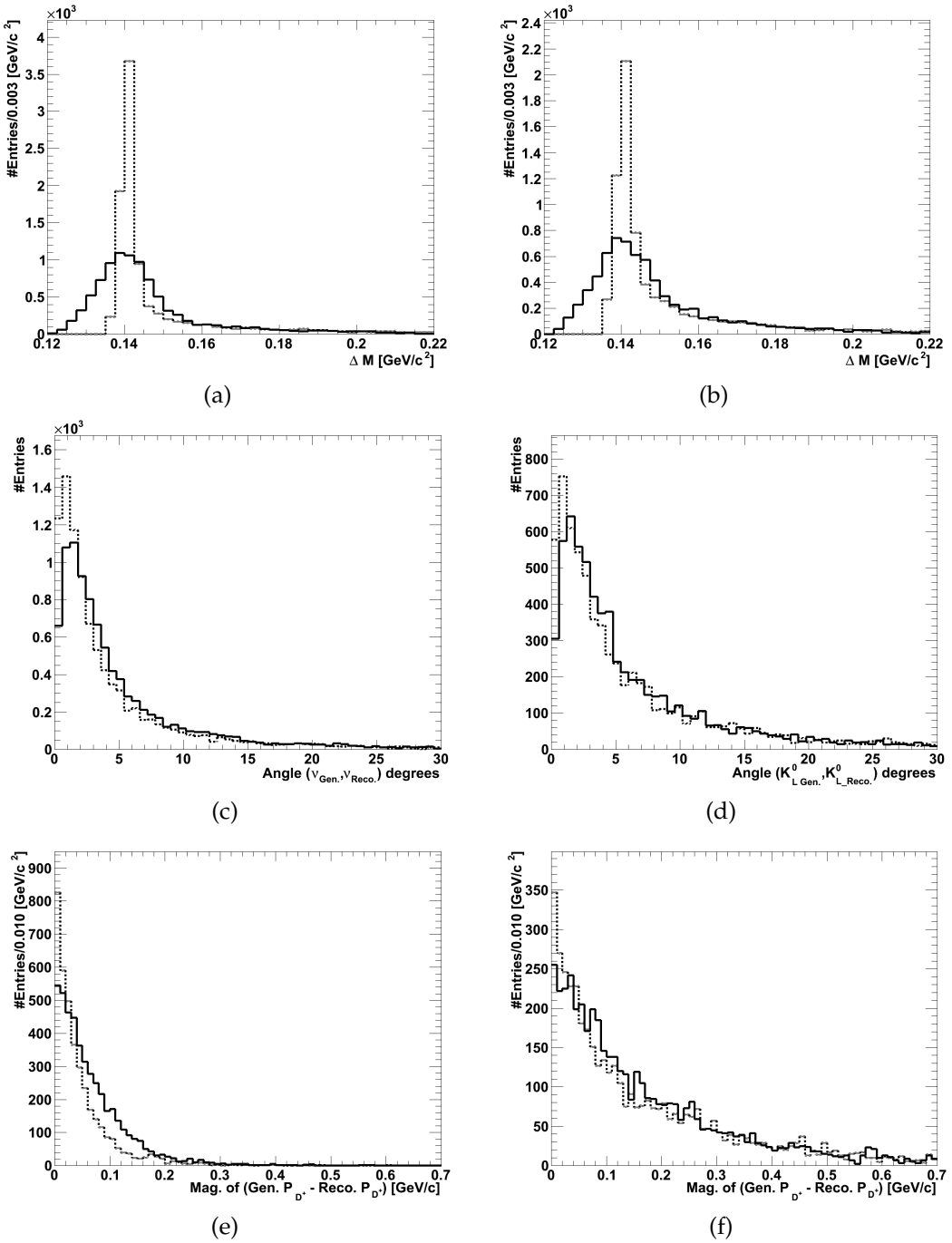

Figure 5.6: These distributions show several properties of the reconstructed $D^+ \to \mu^+\nu$ and $D^+ \to \pi^+ K_L^0$ candidates after the preliminary D^{*+} candidate selection cuts have been applied. In all cases the solid and dashed lines represent the distributions before and after the kinematic fit to the D^{*+} candidate. The plots in the left-hand column show distributions for $D^+ \to \mu^+\nu$ candidates and the plots in the right-hand column show distributions for $D^+ \to \pi^+ K_L^0$ candidates. The definition of each of the variables plotted is discussed in the text.

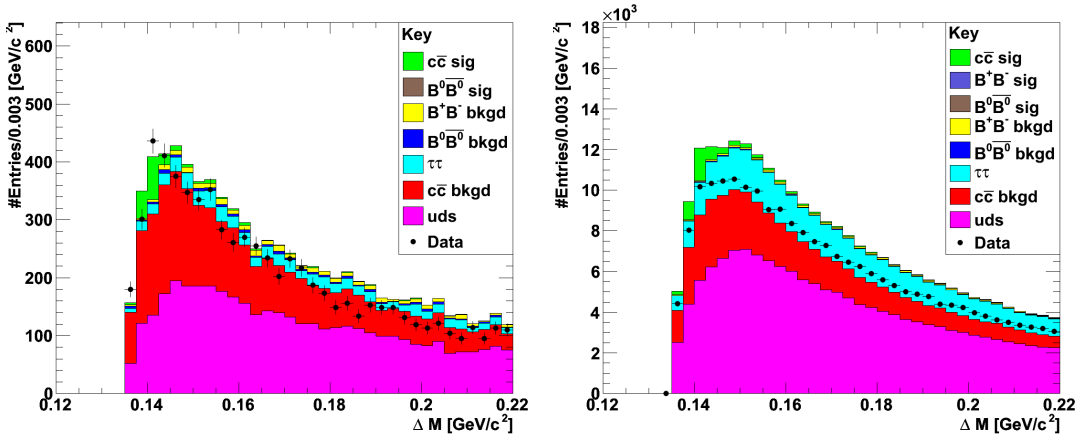

(a) (b)

Figure 5.7: The ΔM distributions for the signal and normalisation modes are shown in (a) and (b). The different colours indicate the contributions from the various generic MC samples. The points represent the data distribution.

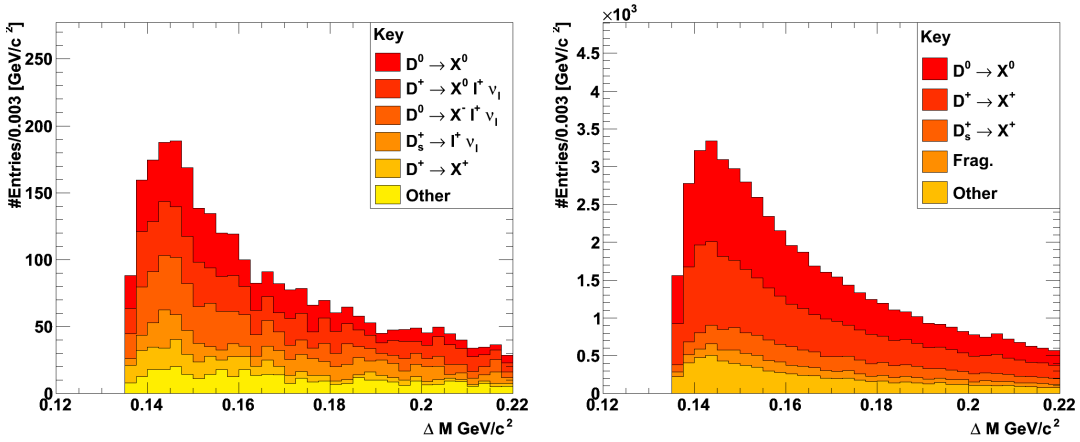

(a) (b)

Figure 5.8: The $c\bar{c}$ backgrounds for the signal and normalisation modes are shown in (a) and (b). In each case, they have been broken down into their various components. Here, $X^{\pm}$ and X^{0} represent sets of charged and neutral hadrons.

5.7 Additional Cuts

After preliminary selection, a total of 11 additional cuts were added. The values of some of the additional cuts were determined by using a simple optimisation procedure. (An optimization involving all of the cuts would have been too time consuming). In the optimization, a set of potential cut values was determined for each of the variables involved by inspecting their generic MC distributions. The optimization procedure involved a simple algorithm that tested every possible combination of cuts in the parameter space, and is described in more detail in section 5.8. The 11 variables and their values are listed in table 5.8. For the optimized variables, a set of tested cut values is given, and the ultimate cut values are shown in bold. A total of 576 different cut combinations were tried during the optimisation procedure. The numbers of charged tracks and neutral clusters in the event are represented by N_T and N_N. The cosines of the polar angles of the muon and neutrino candidates are given by $cos(\theta_{\mu^+})$ and $cos(\theta_\nu)$. The momentum of the π^0 candidate is given by $\mathbf{P}_{\pi^0}$. The ratio of the second Fox-Wolfram moment to the zeroth is represented by $R2$, which has been defined in 5.5. The momentum and mass of the D^+ candidate are given by $\mathbf{P}_{D^+}$ and M_{D^+}. The log of the probability of the χ^2 result of the fit is given by $log(P(\chi^2))$. The difference between the magnitudes of the neutrino candidate momentum before and after the fit is |Raw $\mathbf{P}_\nu$| $-$ |$\mathbf{P}_\nu$|. The momentum of the neutrino candidate is given by $\mathbf{P}_\nu$. All of the cuts that were frame dependent were applied in the cm frame, apart from |Raw $\mathbf{P}_\nu$| $-$ |$\mathbf{P}_\nu$|, which was applied in the D^{*+} frame of reference. For the cuts numbered 3, 5, 7 and 9, the minimum and maximum cut values were tested in pairs during the optimisation; referring to table 5.8, the first minimum cut value was paired with the first maximum cut value and the second minimum cut value was paired with the second maximum cut value. (For example, cut number 3 was tested twice; once using the range $(-0.90 < cos(\theta_\nu) < 0.90)$, and once using the range $(-0.80 < cos(\theta_\nu) < 0.80)$. Each additional cut can be seen on its *N-1* plot, which shows the distribution for the cut variable after all of the N cuts have been applied except the cut in question. The *N-1* distributions are shown in figures 5.9, 5.10, 5.11 and 5.12. In each of the figures, distributions for the signal mode are shown in the left-hand column and distributions for the normalisation mode are shown in the right-hand column. In every *N-1* distribution, the cut is indicated by either a single arrow or a pair of arrows. Figures 5.12e and 5.12f show *cut flow* distributions for the signal and normalisation modes. The

Cut Number	Cut Variable	Min. Value(s)	Max. Value(s)
0	N_T	3	-
1	N_N	-	11
2	Raw $cos(\theta_{\mu^+})$	-0.90	-0.90
3	Raw $cos(\theta_\nu)$	**-0.90**, -0.80	**0.90**, 0.80
4	Raw $\mathbf{P}_{\pi^0}$	0.15, **0.20**	-
5	$R2$	0.25, **0.30**	0.75, **0.70**
6	Raw $\mathbf{P}_{D^+}$ (GeV/c)	2.6, 2.9, **3.2**	-
7	Raw M_{D^+} (GeV/c^2)	1.25, **1.50**	2.75, **2.50**
8	$log(P(\chi^2))$	-5, -4, **-3**	-
9	$\lvert$Raw $\mathbf{P}_\nu\rvert - \lvert\mathbf{P}_\nu\rvert$ (GeV/c)	**-0.100**, -0.095	**0.200**, 0.195
10	$\mathbf{P}_\nu$ (GeV/c)	0.75, **1.00**	-

Table 5.8: Additional cuts applied to D^{*+} candidates for the $D^+ \to \mu^+\nu$ and $D^+ \to \pi^+ K^0_L$ decay modes. For most of the cuts, several minimum and maximum values were tested as part of the optimisation procedure. A total of 576 different cut combinations were tested, and optimised cut values are shown in bold.

cut flow distributions show the number of D^{*+} candidates that survived after each of the cuts given in table 5.8 was applied, one after the other.

5.8 Optimisation Procedure

For a given set of cuts, the resulting generic MC ΔM distribution was fitted with a model which comprised two histogram probability distribution functions (PDFs), one used to represent the signal shape and one used to represent the background shape. The PDF used to represent the signal shape was obtained from the dedicated $D^+ \to \mu^+\nu$ MC sample, while the PDF used to represent the background shape was constructed artificially. The generic MC background components were added to create a total generic MC background. To obtain the background PDF, a *fluctuated* distribution was created by varying the contents of each of the N bins in the total background histogram by $\sigma_i R_i$. Here, σ_i was the error on the i^{th} bin and R_i was a random number which was taken from a Gaussian with a mean of 0 and a standard deviation of 1.

The model was fitted to the ΔM distribution using a minimum χ^2 fit. The FOM chosen was $\sigma_{N_{sig}}/N_{sig}$, where N_{sig} was the number of fitted signal candidates and $\sigma_{N_{sig}}$ was the error on N_{sig}. In order to obtain a reasonable FOM estimate for each set of cuts tested, 1000 fit trials were performed. In each trial a different set of R_i values were used, and so the shape of the artificial background was different each time. Figure 5.13 shows, for a given set of cuts, several distributions related to the fitting procedure. Figure 5.13a

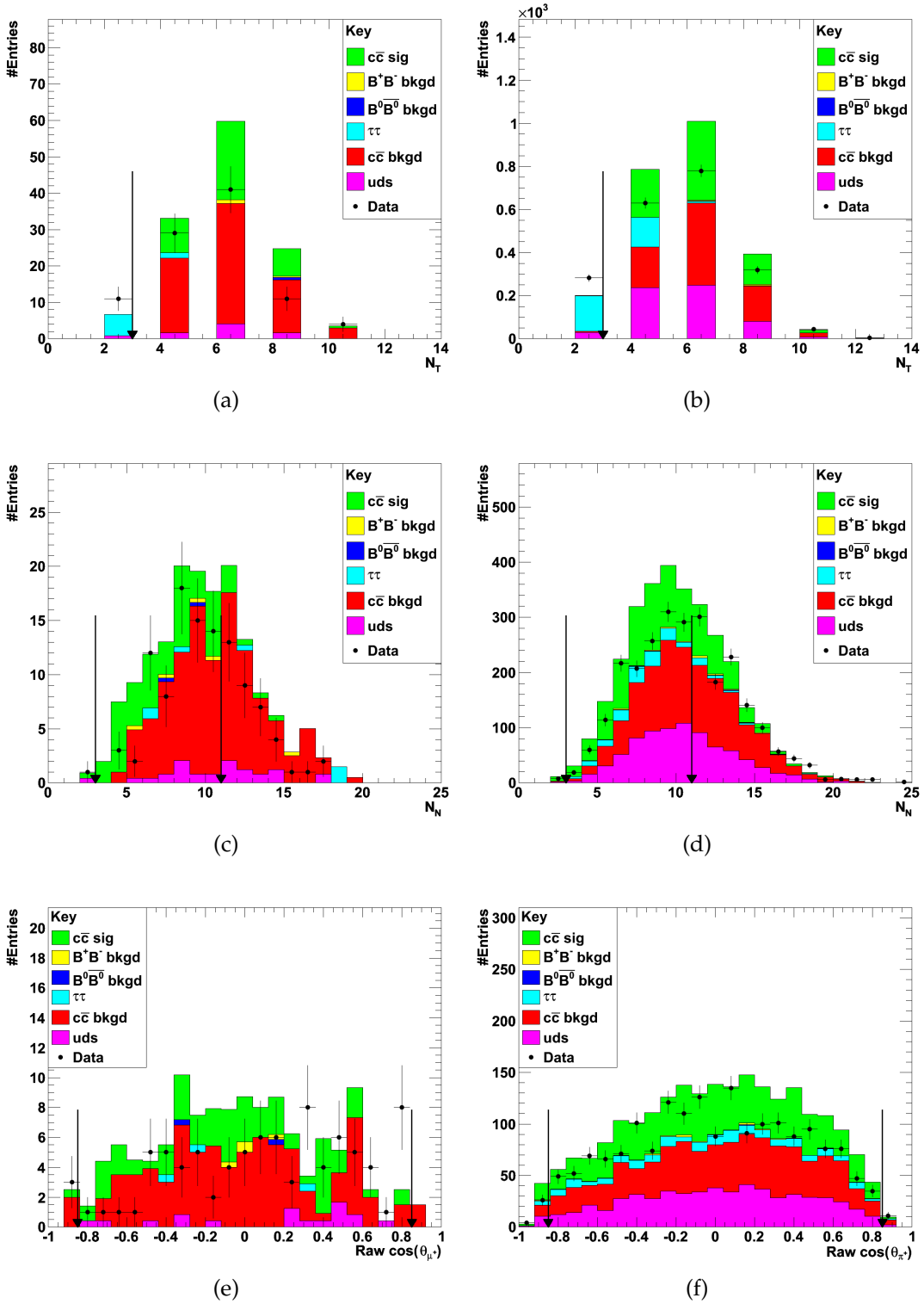

Figure 5.9: Distributions with arrows that show the cut value positions for three of the additional cuts: the number of charged tracks, N_T, the number of neutral clusters, N_N, and the cosine of the raw polar angle for both the signal mode muon candidate, Raw $cos(\theta_{\mu^+})$, and the normalisation mode pion candidate, Raw $cos(\theta_{\pi^+})$. The left- and right-hand columns show distributions the signal and normalisation modes, and each distribution is shown after all of the other additional cuts had been applied.

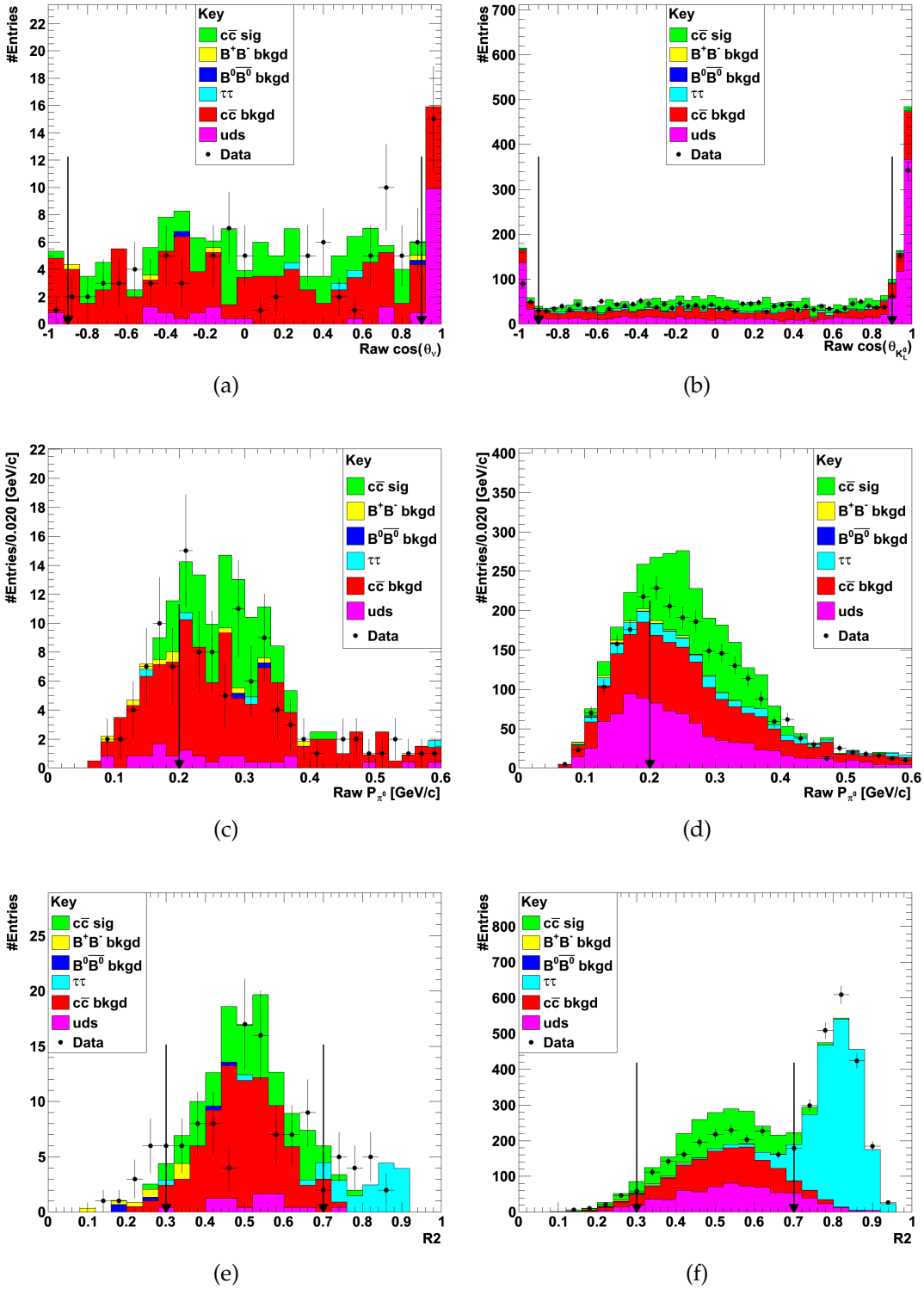

Figure 5.10: Distributions with arrows that show the cut value positions for three of the additional cuts: the cosine of the raw polar angle for both the signal mode neutrino candidate, Raw $cos(\theta_\nu)$, and the normalisation mode K^0_L candidate, Raw $cos(\theta_{K^0_L})$, the raw momentum of the π^0 candidate, Raw $\mathbf{p}_{\pi^0}$, and ratio of the second and zeroth Fow-Wolfram moments for the event, $R2$. The left- and right-hand columns show distributions for the signal and normalisation modes, and each distribution is shown after all of the other additional cuts had been applied.

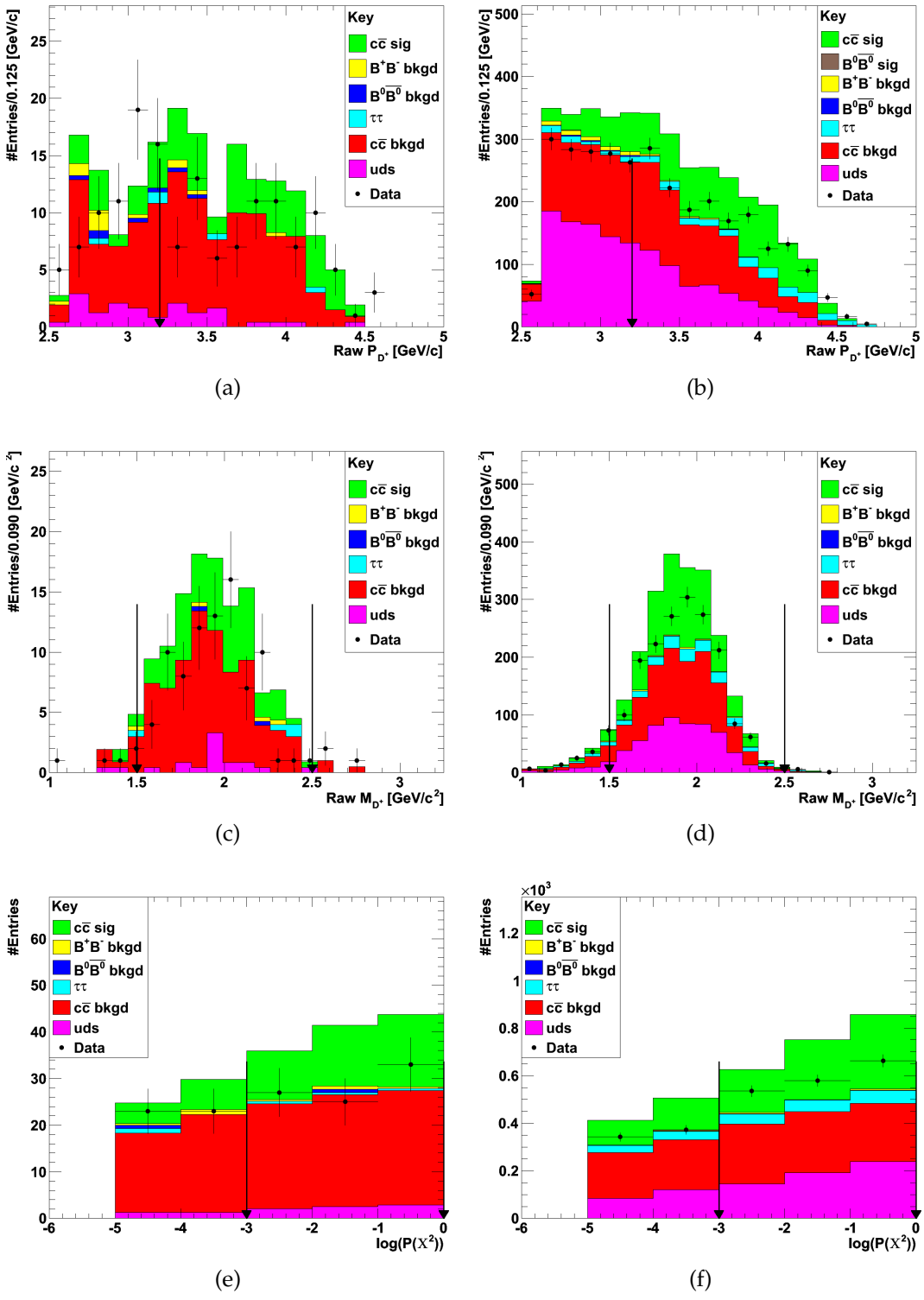

Figure 5.11: Distributions with arrows that show the cut value positions for three of the additional cuts: the raw momentum of the D^+ candidate, Raw $\mathbf{P}_{D^+}$, the raw mass of the D^+ candidate, Raw M_{D^+}, and the log of the probability of the χ^2 result for the D^{*+} candidate, $log(P(\chi^2))$. The left- and right-hand columns show distributions for the signal and normalisation modes, and each distribution is shown after all of the other additional cuts had been applied.

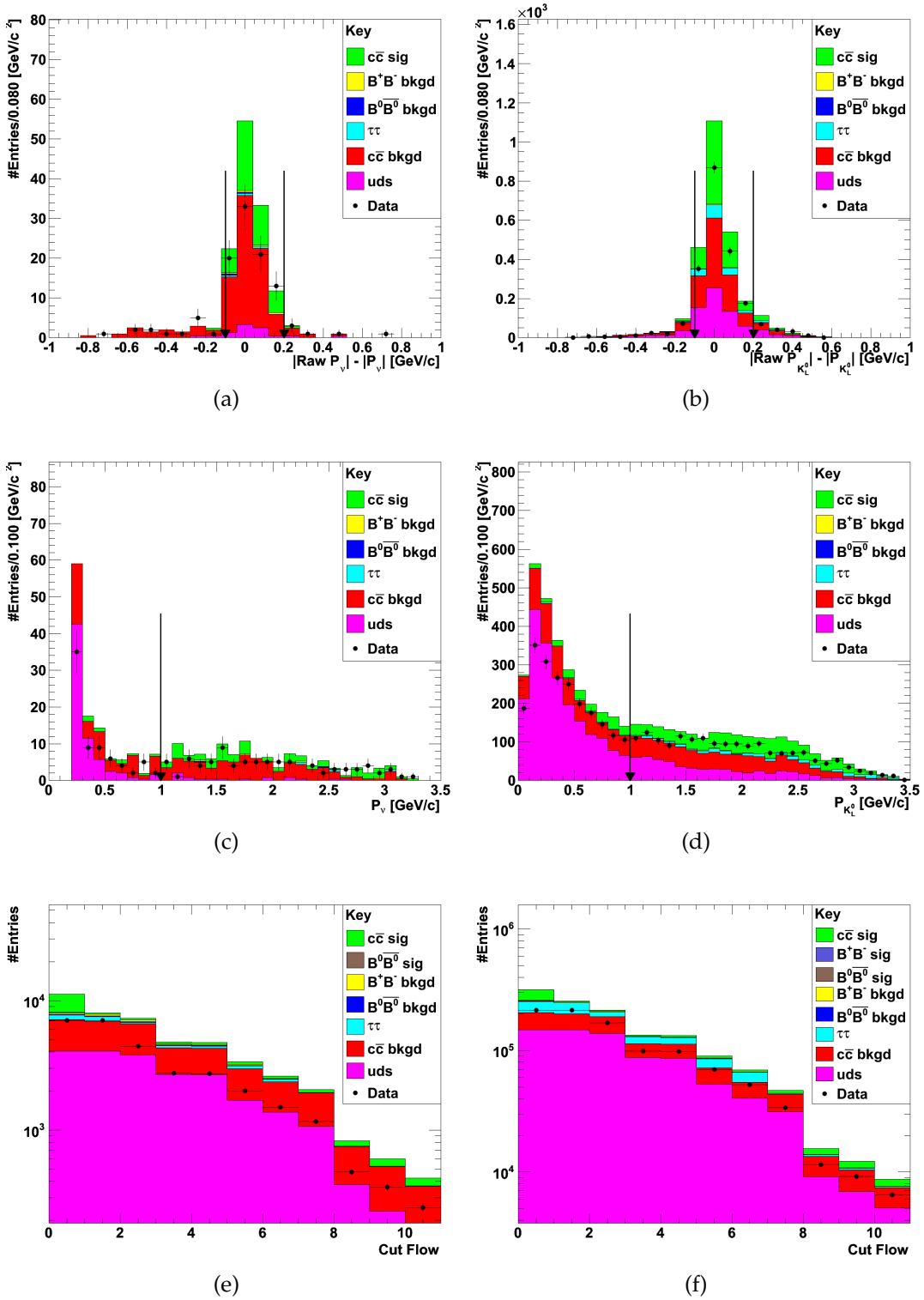

Figure 5.12: Distributions with arrows that show the cut value positions for two of the additional cuts: the difference between the magnitude of the momentum of the raw neutrino (K_L^0) candidate and the post-fit neutrino (K_L^0) candidate for the signal (normalisation) mode, $|\text{Raw } \mathbf{P}_\nu| - |\mathbf{P}_\nu|$ ($|\text{Raw } \mathbf{P}_{K_L^0}| - |\mathbf{P}_{K_L^0}|$), and the momentum of both the signal mode neutrino candidate, $\mathbf{P}_\nu$, and the normalisation mode K_L^0 candidate, $\mathbf{P}_{K_L^0}$. The *Cut Flow* plot shows the effect that each successive cut had on the number of D^{*+} candidates, where the number on the x-axis corresponds to the *Cut Number* of table 5.8. The left- and right-hand columns show distributions for the signal and normalisation modes, and each distribution is shown after all of the other additional cuts had been applied.

shows the signal PDF and 5.13b shows a typical artificial background PDF on top of the original total generic MC background histogram. The fit of the model to the generic MC distribution is shown in figure 5.13c, where the model shape is shown as the solid line, the background component of the model is shown as the dashed line, and the points with error bars represent the generic MC distribution. The $\sigma_{N_{sig}}/N_{sig}$ distribution, where each entry came from a different trial, is shown in figure 5.13d. The ultimate FOM estimate for a given set of cuts was obtained by using the mean value of the $\sigma_{N_{sig}}/N_{sig}$ distribution. Using the optimised (i.e. bold) set of cuts given in table 5.8, the FOM was found to be $\sigma_{N_{sig}}/N_{sig} = 0.085$.

5.9 ΔM Distributions After Optimisation

The ΔM distributions for the signal and normalisation decay modes are shown in figures 5.14a and 5.14b, after the optimised cuts have been applied. Like the figures of 5.7, the colours indicate the different contributions from the generic MC and the data points have been overlaid.

Of the events that contained either a true signal decay or a true normalisation mode decay, only candidate reconstructions of $c\bar{c}$ events survived the additional cuts. Those candidate reconstructions of $B^0\overline{B}^0$ and B^+B^- events that contained either a true signal decay or a true normalisation mode decay did not survive.

The only significant background that remained for the signal mode came from $c\bar{c}$ events that contained either leptonic or semi-leptonic D^+ and D_s^+ decays. The background candidates had very similar properties to signal candidates, and so these backgrounds were deemed to be irreducible. Figure 5.15a shows the various components of the $c\bar{c}$ background to the signal mode after optimization.

After the additional cuts were applied in the normalisation mode, a small fraction of candidates that came from reconstructed fragmentation particles in uds events remained. Most of the normalisation mode background candidates came from $c\bar{c}$ events that contained hadronic D^+ and D^0 decays. Again, the similarity of these candidates to those of the normalisation mode meant that these types of background were deemed to be irreducible. Figure 5.15b shows the various components of the $c\bar{c}$ background to the normalisation mode after optimization.

The final distributions of ΔM for the normalisation mode showed a large difference in the number of reconstructed $D^+ \to \pi^+ K^0_L$ events in data compared to MC. The reconstruction efficiency for $D^+ \to \pi^+ K^0_L$ events in MC looked to be approximately twice that of data. This discrepancy was attributed to poor simulation of K^0_L interactions with the detector. One possible explanation for this discrepancy is that less energy was deposited for simulated interactions between K^0_L mesons and the detector than for real interactions. The D^{*+} candidate reconstruction procedure, which assumed that the missing particle did not interact with the detector at all, would therefore result in a higher reconstruction efficiency for $D^+ \to \pi^+ K^0_L$ events in MC than in data. A measurement of the $D^+ \to \pi^+ K^0_L$ branching fraction was therefore not performed because the relative error on the final result would have been high due to the large uncertainty on the reconstruction efficiency for the normalisation mode.

5.10 D^{*+} Momentum Distribution for the Signal Mode

To test the reliability of the generated D^{*+} momentum spectrum, and the D^{*+} candidate reconstruction procedure, the momentum distribution of reconstructed D^{*+} candidates in data and dedicated signal MC events was investigated.

A program called JETSET [50] was used to simulate $q\bar{q}$ fragmentation and hadronisation in continuum events at *BABAR*. The momentum spectrum of such events was mainly governed by a function called the *Lund Symmetric Fragmentation Function*, $f(z)$, which described the probability that the q jet, moving along the z-axis, would receive a particular $+z$ value and that the $\bar{q}$ jet, also moving along the z-axis, would receive the corresponding $-z$ value. The function is shown in 5.7:

$$f(z) \sim \frac{1}{z}(1-z)^a exp\left(-\frac{bm_T^2}{z}\right) \tag{5.7}$$

where a and b are parameters which were determined empirically. At *BABAR*. a and b were 0.30 and $0.58\ GeV^{-2}$. The *transverse mass* of a hadron is represented by m_T and defined as $m_T^2 = m^2 + p_T^2$, where p_T is the component of the hadron's momentum which is in the plane transverse to the z-axis.

Figure 5.16 shows the momentum distribution for D^{*+} candidates, $P_{D^{*+}}$, in the laboratory frame for data and dedicated signal MC. Only those candidates in the signal

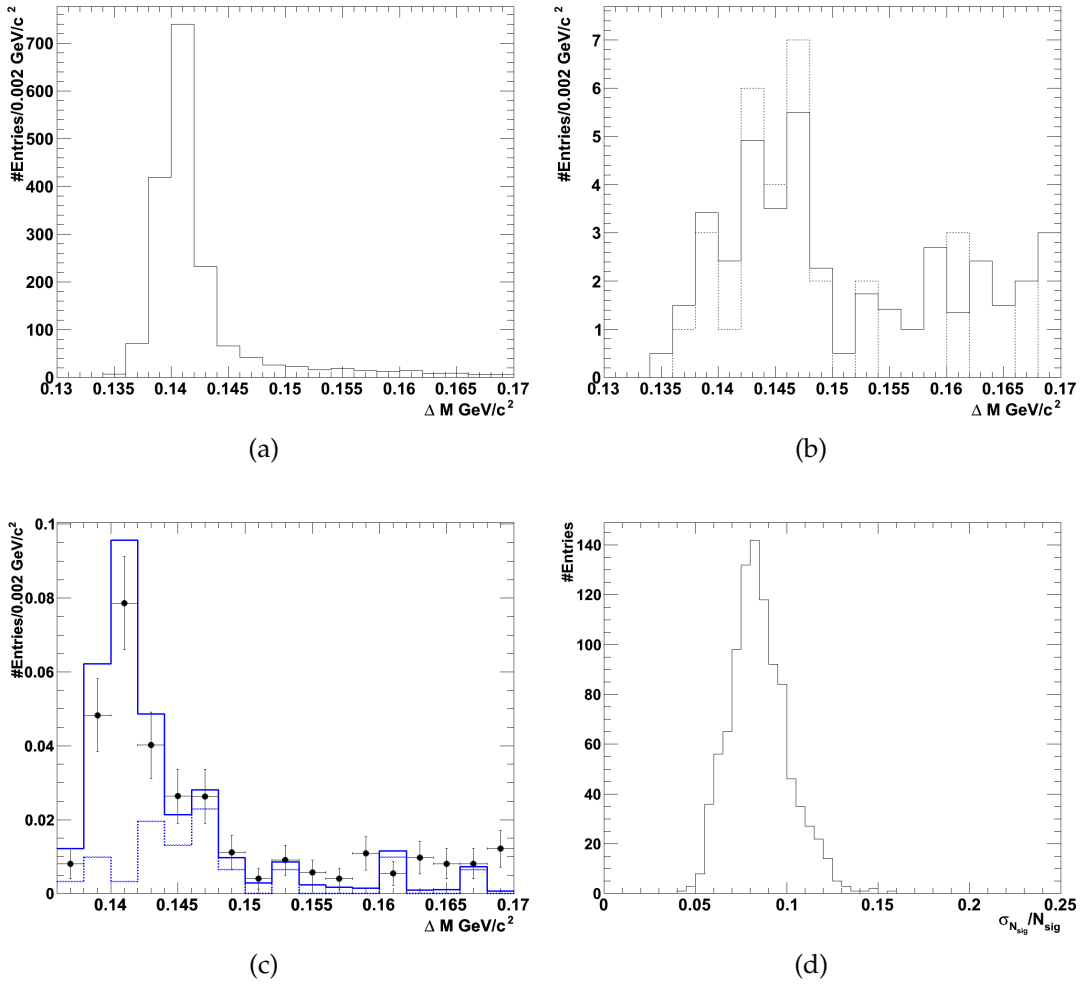

Figure 5.13: Typical optimisation output for a given set of cuts. Figures (a), (b) and (c) show distributions which relate to a single fit trial. The PDF for the dedicated signal MC sample is shown in (a). In (b), the total generic background MC shape is shown as a solid line and the fluctuated background PDF, which is represented by a dashed line, has been overlaid. The model, which comprised the signal and fluctuated background PDFs, was fitted to the ΔM distribution of the total generic MC. The fitted distribution is shown in (c), where the blue (solid) line represents the model, the dashed line shows the background component of the model and the points represent the total generic MC distribution. In (d), the $\sigma_{N_{sig}}/N_{sig}$ values (explained in the text) for the 1000 fit trials have been plotted.

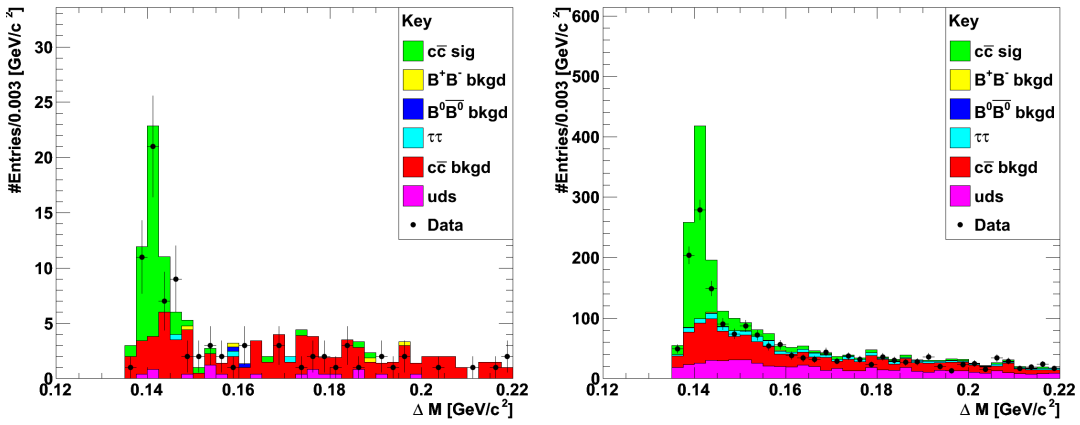

(a) (b)

Figure 5.14: The ΔM distributions for the signal and normalisation modes are shown in (a) and (b), after the ultimate set of cuts had been applied.

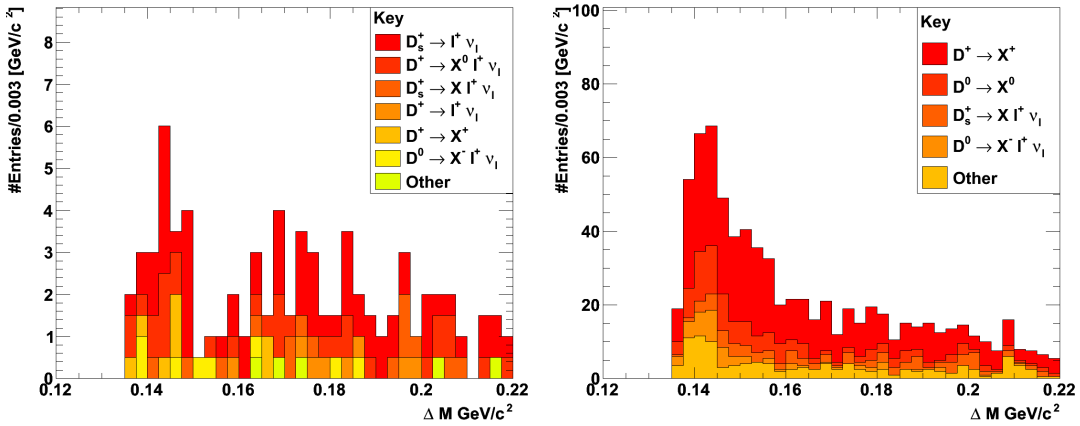

(a) (b)

Figure 5.15: The $c\bar{c}$ backgrounds for the signal and normalisation modes are shown in (a) and (b) after the optimised cuts listed in table 5.8 had been applied. In each case, they have been broken down into their various components. Here, $X^{\pm}$ and X^{0} represent sets of charged and neutral hadrons.

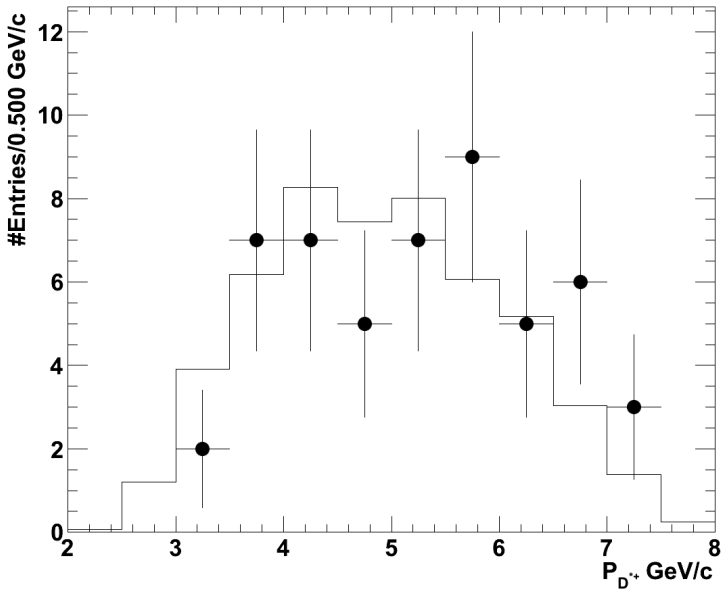

Figure 5.16: Momentum distribution for D^{*+} candidates in the laboratory frame. The distribution is shown after all selection criteria have been applied, and only for candidates with ΔM values below $0.15\ GeV/c^2$).

region of the ΔM distribution are shown (i.e. for candidates with ΔM values below $0.15\ GeV/c^2$). The area of the dedicated signal MC distribution has been normalised to that of data. The distributions show reasonable agreement, which helps to validate the fragmentation function used to generate the D^{*+} momentum spectrum as well as the D^{*+} candidate reconstruction procedure.

Chapter 6

Results

6.1 Overview

This chapter describes the fit procedure that was performed on the distribution of ΔM in data in order to obtain a value for the signal mode yield. The efficiency for reconstructing signal mode decays in signal MC events is found. A description of how this efficiency is corrected to account for known differences in particle reconstruction and particle identification between data and MC events is given. The method used to obtain a value for the branching fraction $BF(D^+ \to \mu^+\nu)$ is described and values for f_{D^+} and $(f_{D_s^+}/f_{D^+})$ are then calculated. The systematic errors associated with each of the results are discussed. Finally, values for $BF(D^+ \to \mu^+\nu)$, f_{D^+} and $(f_{D_s^+}/f_{D^+})$ are given, along with their respective statistical and systematic errors.

6.2 ΔM Fit

The signal mode ΔM distribution, shown in figure 5.14a, was fitted to obtain a signal yield using a model that contained a signal PDF and a background PDF. The shape of the signal PDF was taken from the dedicated MC and the shape of the background PDF was taken from the sum of the generic background MC components. The model was fitted to the data using an unbinned maximum likelihood fit. The result of the fit is shown in figure 6.1. The fitted number of signal events, N_{sig}, is $N_{sig} = 45.3 \pm 6.7$, where the error is statistical, only. Note that since the uncertainty on the unbinned maximum likelihood fit was approximately equal the statistical uncertainty on N_{sig}, no additional systematic

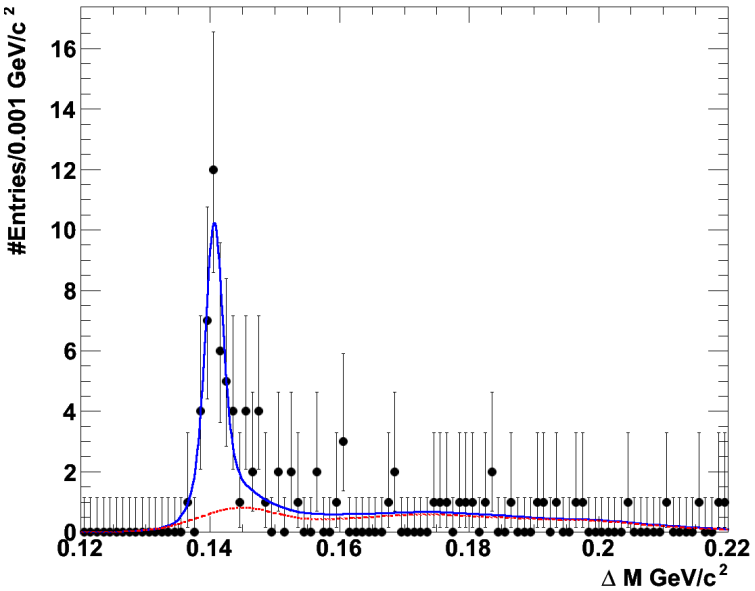

Figure 6.1: Fitted ΔM distribution for the signal mode. The fit model is shown as a solid blue line and the background component of the model is shown as a dashed red line. The points represent data.

was attributed to the fit procedure itself.

6.3 Monte Carlo Efficiency Corrections

Using the dedicated signal MC event sample, the signal mode reconstruction efficiency, ε_{MC}, was found to be $(1.09 \pm 0.03) \times 10^{-3}$, where the error is statistical, only. Three correction factors were applied to ε_{MC} in order to account for known differences in efficiency for particle identification, neutral particle reconstruction, and charged track reconstruction between data and MC events. Equation 6.1 shows how the estimated signal efficiency in data, ε, was related to ε_{MC}:

$$\varepsilon = \varepsilon_{MC}(C^{Trk})^{\bar{n}_{Trk}^{MC}} \prod_{i=1}^{2}(C_i^{PID})^{\bar{n}_i^{MC}} \prod_{j=1}^{2}(C_j^{Reco})^{\bar{n}_j^{MC}} \tag{6.1}$$

Here, C_i^{PID} represents the particle identification (PID) efficiency correction for the i^{th} particle type, where $i = 1$ represents the signal muon and $i = 2$ represents the K^+. The neutral particle reconstruction (Reco) efficiency correction for the j^{th} particle type is represented by C_j^{Reco}, where $j = 1$ represents the K_S^0 and $j = 2$ represents the π^0. The charged particle reconstruction (Trk) efficiency correction is represented by C^{Trk}. The indices, $\bar{n}_i^{MC}$ and $\bar{n}_j^{MC}$ represent the mean number of candidates for particle type i and j

Particle	C^{PID}	σ^{PID} (%)	C^{Reco}	σ^{Reco} (%)	$\bar{n}^{MC}$
μ^+_{sig}	1.02	1.00	-	-	1.00
K^+	0.99	1.00	-	-	0.74
π^+	-	-	-	-	3.64
K^0_S	-	-	0.97	0.01	0.18
π^0	-	-	0.98	0.03	1.34

Table 6.1: Data to MC efficiency correction factors, C^{PID} and C^{Reco}, and their associated errors, σ^{PID} and σ^{Reco}. The mean number of candidates per signal MC event, for each particle type, is represented by $\bar{n}^{MC}$. To obtain $\bar{n}^{MC}$, only events that contained D^{*+} candidates which satisfied all selection criteria were used. To remove contributions to $\bar{n}^{MC}$ from events which contained background candidates, an upper limit of $0.15\ GeV/c^2$ was imposed on the ΔM value of the D^{*+} candidates.

in signal MC events. The mean number of tracks in a signal MC event is represented by $\bar{n}^{MC}_{Trk}$. Only those signal MC events that contained D^{*+} candidates which satisfied all the selection criteria were used to obtain values for $\bar{n}^{MC}_i$, $\bar{n}^{MC}_j$ and $\bar{n}^{MC}_{Trk}$. The ΔM value of the D^{*+} candidate also had to be below $0.15\ GeV/c^2$ in order to prevent contributions to $\bar{n}^{MC}_i$, $\bar{n}^{MC}_j$ and $\bar{n}^{MC}_{Trk}$ from events that contained background D^{*+} candidates.

Only the five types of particle discussed above were considered in the product of equation 6.1; those particle types for which the mean number of candidates per event was small were not considered, as their contribution would have been negligible. Table 6.1 shows the efficiency correction factors for the particle types, along with their associated errors. The mean number of candidates per signal MC event is also given for each particle type. Distributions of the numbers of candidates per event, for each particle type, are shown in figure 6.2 for both data and signal MC. For all particle types, the signal MC distributions agree with those of data, which justifies the use of $\bar{n}^{MC}_i$, $\bar{n}^{MC}_j$ and $\bar{n}^{MC}_{Trk}$ in equation 6.1.

The particle identification efficiency corrections for signal muons and charged kaons were estimated using the results of control sample studies. The control sample used in the signal muon study contained muons from $e^+e^- \to \mu^+\mu^-\gamma$ events [51] [44]. For the charged kaon study, a control sample that contained decays of the form $D^{*+} \to D^0\pi^+$, $D^0 \to K^-\pi^+$ was used [52] [44]. No PID efficiency correction for charged pions was used because the pion mass hypothesis was not chosen based on the result of a selector, rather is was the default hypothesis, only given if a charged track did not satisfy the requirements of any of the particle selectors. An estimation of the K^0_S reconstruction

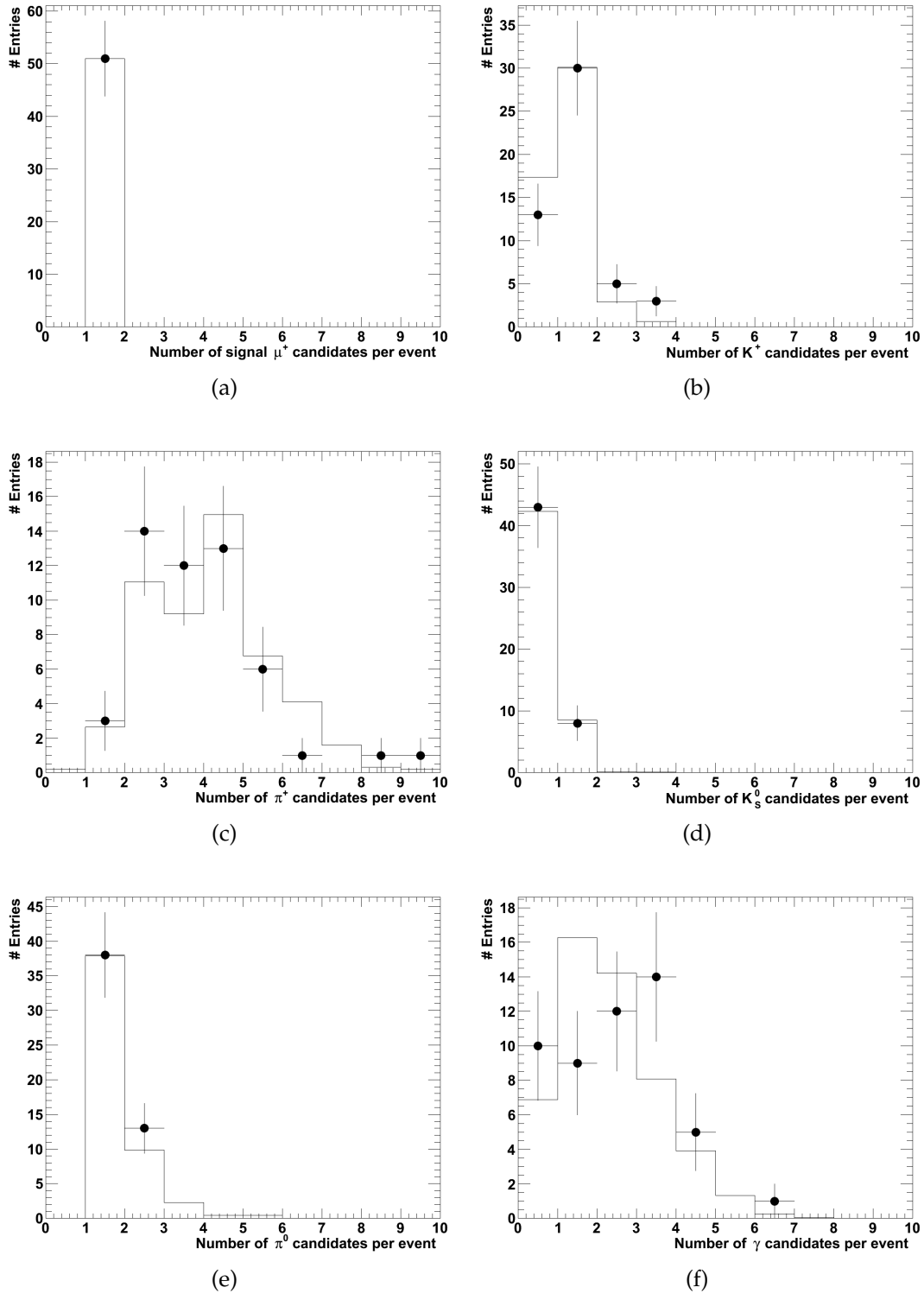

Figure 6.2: Data and signal MC distributions that show, for each particle type, the numbers of candidates that remained in an event. The signal MC distribution is represented by a solid line and the points represent data. The area of the signal MC distribution has been scaled to match the area of the data distribution. Distributions for those particle types which had either zero entries, or negligible multiplicities are not shown.

efficiency correction was taken from an analysis that measured the branching fraction, $B^0 \to \eta_c K^0$ [53]. The π^0 reconstruction efficiency correction was taken from a study which used $\tau^+ \to \pi^+ \bar{\nu}$ and $\tau^+ \to \rho^+ \bar{\nu}$ decays [54]. The track reconstruction efficiency was estimated using the results of a *BABAR* study of $\tau^+\tau^-$ decays, where one of the tau decays resulted in a single charged particle and the other resulted in three charged particles [55]. The mean number of charged tracks per signal MC event was found to be 5.74; thus the overall charged particle reconstruction efficiency correction was found to be $(C^{Trk})^{\bar{n}^{MC}_{Trk}} = (0.989 \pm 0.005)$.

After correcting ε_{MC} using equation 6.1, the signal efficiency for data was found to be $\varepsilon = (1.05 \pm 0.05) \times 10^{-3}$, where the error incorporates each of the particle reconstruction, particle identification and track reconstruction uncertainties, as well as the statistical uncertainty related to ε_{MC}.

6.4 $D^+ \to \mu^+\nu$ Branching Fraction

In order to calculate the signal mode branching fraction, a value for the inclusive production cross-section for D^{*+} mesons in data, $\sigma(e^+e^- \to D^{*+}X)$, at the energy scale of *BABAR* was needed, where X represents all other particles produced. A study by CLEO measured $\sigma(e^+e^- \to D^{*+}X)$ to be $(583 \pm 8 \pm 33 \pm 14)\ pb$ at a centre-of-mass energy of $10.5\ GeV$ [56]. The first two errors on $\sigma(e^+e^- \to D^{*+}X)$ are statistical and systematic, and the third error came from the uncertainty on the measured $D^0 \to K^-\pi^+$ branching ratio. In the CLEO study, the D^{*+} mesons were reconstructed using $D^{*+} \to D^0\pi^+$, $D^0 \to K^-\pi^+$ decays.

Using $\sigma(e^+e^- \to D^{*+}X)$, and the combined integrated luminosity of runs 1 to 6 at *BABAR* (see table 5.1), the total number of D^{*+} mesons produced, $N_{D^{*+}}$, was estimated to be $(278 \pm 17) \times 10^6$, where the uncertainty came from the combined error on the value for $\sigma(e^+e^- \to D^{*+}X)$. (Uncertainty on the integrated luminosity value was negligible.)

The branching fraction for $D^+ \to \mu^+\nu$ could then be calculated using equation 6.2:

$$BF(D^+ \to \mu^+\nu) = \frac{N_{sig}/\varepsilon}{N_{D^+}} \tag{6.2}$$

Here, N_{sig} was the number of fitted signal events, N_{D^+} was the total number of D^+ mesons that came from $D^{*+} \to D^+\pi^0$ decays and ε was the estimated efficiency for

signal mode events in data, taken from equation 6.1. The total number of D^+ mesons from $D^{*+} \to D^+\pi^0$ decays was given by:

$$N_{D^+} = N_{D^{*+}} BF(D^{*+} \to D^+\pi^0) \tag{6.3}$$

where the branching fraction for $D^{*+} \to D^+\pi^0$ was taken to be $(30.7 \pm 0.5) \times 10^{-2}$ [2]. Using equation 6.2, a value for the signal mode branching fraction was found:

$$BF(D^+ \to \mu^+\nu) = (5.06 \pm 0.74) \times 10^{-4} \tag{6.4}$$

where the uncertainty quoted comes from the statistical error on N_{sig}, only.

6.5 Determination of f_{D^+} and $(f_{D_s^+}/f_{D^+})$

The measured branching fraction was then used to obtain values for f_{D^+} and the ratio, $(f_{D_s^+}/f_{D^+})$. Equation 2.4 was used to calculate a value for f_{D^+}, where values for the Fermi constant and the muon and D^+ meson masses were taken from reference [2]. A value of 0.22529 ± 0.00077 was used for the matrix element V_{cd} [7]. The branching fraction for the signal decay mode was converted into a decay rate using equation 6.5:

$$\Gamma(D^+ \to \mu^+\nu) = \frac{BF(D^+ \to \mu^+\nu) \times \hbar}{\tau_{D^+}} \tag{6.5}$$

where the lifetime of the D^+ meson, τ_{D^+}, was taken from reference [2]. Resulting values for f_{D^+} and $(f_{D_s^+}/f_{D^+})$ are:

$$f_{D^+} = (237 \pm 18)\ MeV \tag{6.6}$$

$$f_{D_s^+}/f_{D^+} = (1.08 \pm 0.08) \tag{6.7}$$

where in both cases the quoted error came from the uncertainty on the branching fraction $BF(D^+ \to \mu^+\nu)$, only.

6.6 Systematic Errors

The dominant sources of systematic error are summarised in table 6.2. A combined error for the data to MC efficiency corrections for track reconstruction, neutral particle recon-

Source of Uncertainty	Uncertainty (%)
MC Efficiency Correction	4.9
D^{*+} production cross-section	6.3
$BF(D^{*+} \to D^+\pi^0)$	1.6
Total	8.1

Table 6.2: Sources of systematic uncertainty for the signal mode measurement.

struction and particle identification was included. The uncertainty in the production cross-section for D^{*+} mesons was taken to be equal to the errors on $\sigma(e^+e^- \to D^{*+}X)$ combined in quadrature. Another source of uncertainty came from the error on the $D^{*+} \to D^+\pi^0$ branching fraction. The total systematic uncertainty on the measured values for $BF(D^+ \to \mu^+\nu)$, f_{D^+} and $(f_{D_s^+}/f_{D^+})$ was found by combining the individual systematic errors in quadrature.

Uncertainty from the model used to fit the signal ΔM distribution was deemed to be negligible compared to the statistical error on the result of the fit, and so it was not included as a systematic error. The statistical error associated with the MC sample that was used to create the PDF for the background component of the fit model was also ignored, because it, too, was negligible in relation to the statistical error on the fit result.

6.7 Final Results

The final results for the $D^+ \to \mu^+\nu$ branching fraction and the D^+ meson decay constant are:

$$BF(D^+ \to \mu^+\nu) = (5.06 \pm 0.74 \pm 0.41) \times 10^{-4} \tag{6.8}$$

$$f_{D^+} = (237 \pm 18 \pm 10)\ MeV \tag{6.9}$$

where, for both values, the first error is statistical and the second is systematic. The final value of the decay constant ratio is:

$$(f_{D_s^+}/f_{D^+}) = (1.08 \pm 0.08 \pm 0.04 \pm 0.02) \tag{6.10}$$

where the first two errors are statistical followed by systematic, and the third error came from the uncertainty in the $f_{D_s^+}$ value.

Chapter 7

Conclusions

This thesis documents work that was carried out by the author, at the University of Manchester in the UK, and at the SLAC National Accelerator Laboratory in the US. The bulk of the thesis relates to a measurement of the decay constant for the D^+ meson, f_{D^+}, using $476\ fb^{-1}$ of integrated luminosity recorded using the *BABAR* detector. Part of the thesis discusses event selection work that was performed as part of a measurement of the decay constant for the D_s^+ meson, $f_{D_s^+}$.

The main aim behind the f_{D^+} measurement was to test the reliability of a result produced by a recent LQCD calculation [13]. The same calculation predicts a value for $f_{D_s^+}$ that differs from the Particle Data Group average by 2.4σ, a discrepancy that could be the result of new physics. (Note, however, that the results of the LQCD calculation have recently been updated, and the difference between the new $f_{D_s^+}$ prediction and the Particle Data Group average is now 1.4σ [15].)

A measurement of the $D^+ \to \mu^+\nu$ decay rate is currently the only viable means of obtaining a value for f_{D^+}, and at present the Particle Data Group recognises only a single measurement for $BF(D^+ \to \mu^+\nu)$ (and therefore for f_{D^+}), which was made by CLEO-c [5]. Thus, a secondary goal of the f_{D^+} analysis was to obtain a second viable measurement of $BF(D^+ \to \mu^+\nu)$. A measurement of f_{D^+} can also be used in the ratio $(f_{D_s^+}/f_{D^+})$, which is useful because for some theoretical models it has a smaller relative error than that of either $f_{D_s^+}$ or f_{D^+} [13].

This analysis obtained values for $BF(D^+ \to \mu^+\nu)$ and f_{D^+} by reconstructing the decay chain $D^{*+} \to D^+\pi^0$, $D^+ \to \mu^+\nu$. A *whole-event* method was used to reconstruct signal candidates, and the signal variable used was the mass difference between the re-

Result	This Analysis	PDG	LQCD
$BF(D^+ \to \mu^+\nu)$ $(\times 10^{-4})$	$5.06 \pm 0.74 \pm 0.41$	3.82 ± 0.33	-
f_{D^+} (MeV)	$237 \pm 18 \pm 10$	205.8 ± 8.9	207 ± 4
$(f_{D_s^+}/f_{D^+})$	$1.08 \pm 0.08 \pm 0.04$	1.257 ± 0.068	1.164 ± 0.011

Table 7.1: A summary of the results for this analysis, along with the corresponding Particle Data Group (PDG) results [5] [2]. The LQCD results from reference [13] are also shown. The errors on the values obtained by this analysis are statistical followed by systematic; the errors on all other results have been combined in quadrature.

constructed D^{*+} and D^+ meson candidates. To estimate the number of D^{*+} mesons that were present in data, a CLEO measurement of the cross-section for inclusive D^{*+} production from e^+e^- annihilation at $\sqrt{s} \approx 10.6\,GeV$ was used. The 6% relative error on this measurement had a relatively small impact on the final results of this analysis.

The results of this analysis are shown, along with the corresponding Particle Data Group values, in table 7.1. The results of the LQCD calculation mentioned above (and discussed in section 2.2) are also shown.

The measured branching fraction for $D^+ \to \mu^+\nu$ decay differed from the CLEO-c result by 1.4 standard deviations.

The relative error on the value for $BF(D^+ \to \mu^+\nu)$ is around twice as large as that of CLEO-c, and therefore the CLEO-c result remains the most precise. However, it is also around four times smaller than the second best $BF(D^+ \to \mu^+\nu)$ measurement [31] (see section 2.9.2):

$$BF(D^+ \to \mu^+\nu_\mu) = (0.122^{+0.111}_{-0.053} \pm 0.010) \times 10^{-2} \tag{7.1}$$

The measured f_{D^+} and $(f_{D_s^+}/f_{D^+})$ results are 1.39 and 1.58 standard deviations from the Particle Data Group values. While the sensitivity of the f_{D^+} value obtained in this analysis is below that of CLEO-c, it does represent a vast improvement on the second best experimental determination of f_{D^+}:

$$f_{D^+} = (371^{+129}_{-119} \pm 25)\ MeV \tag{7.2}$$

which was derived from 7.1, above.

The dominant source of error on the f_{D^+} measurement came from the limited statistics of the data sample after all selection criteria had been applied. Such statistical limitations should not be an issue for the detectors of future B-factories, like the proposed

detectors *Super KEKB* [57] and *SuperB* [58]. The peak instantaneous luminosity of SuperB is expected to be, $\approx 2.5 \times 10^{36}\ cm^{-2}s^{-1}$, i.e. around 100 times that of *BABAR*. Over a 10 year lifespan, the detector is expected to receive a delivered luminosity above $150ab^{-1}$. This would correspond to a dataset which was around 300 times the size of the *BABAR* dataset. Thus, if this analysis procedure were carried out at SuperB (and the signal mode reconstruction efficiency was the same), the resulting statistical error on the f_{D^+} result would be around 30 times smaller.

A. The invariant mass range of the ($\mu^+\pi^0$) and ($\pi^+\pi^0$) systems

The invariant mass of a system, M_{inv}, that contains N particles, and where E_i and $\mathbf{P_i}$ are the energy and momentum of the i^{th} particle, is given by:

$$M_{inv}^2 = \left(\sum_{i=0}^{N} E_i\right)^2 - \left(\sum_{i=0}^{N} \mathbf{P_i}\right)^2 \tag{3}$$

To find the invariant mass of the ($\mu^+\pi^0$) system, the energies and momenta of the μ^+ and π^0 are needed, all in the same frame of reference. The energy of the π^0, E_{π^0}, in the D^{*+} frame of reference is given by:

$$E_{\pi^0} = \frac{M_{D^{*+}}^2 - m_{D^+}^2 + m_{\pi^0}^2}{2M_{D^{*+}}}$$

Here, M_D^{*+}, m_D^+ and M_{π^0} are the masses of the D^{*+}, D^+ and π^0 mesons. Using particle masses from [2], the energy of the π^0 is found to be $E_{\pi^0} = 139.7\ MeV$. The momentum of the π^0 (and therefore the D^+, too) in the D^{*+} frame of reference is $38\ MeV/c$ [2].

For the muon energy, E_{μ^+}, we have:

$$E_{\mu^+} = \frac{M_{D^+}^2 + m_{\mu^+}^2}{2M_{D^+}}$$

Here, m_{μ^+}, is the mass of the μ^+ and the neutrino mass has been neglected. Using particle masses from [2], the energy of the μ^+ is found to be $E_{\mu^+} = 938.0\ MeV$. The PDG gives the momentum of the μ as $932\ MeV/c$.

Now, E_{π^0} and $\mathbf{P_{\pi^0}}$ are known in the D^{*+} frame, and E_μ^+ and $\mathbf{P}_{\mu^+}$ are known in the D^+ frame. In order to proceed with the calculation, either the π^0 four-momentum should be lorentz boosted into the frame of reference of the D^+, or the μ^+ four-momentum should be lorentz boosted into the frame of reference of the D^{*+}. To see if a boost is required, the usual factors of $\gamma = (1-\beta^2)^{-\frac{1}{2}}$ and $\beta = \mathbf{P}/E$ need to be found. Taking the boost to be from the D^{*+} frame of reference to that of the D^+, β is given by, $\beta = \mathbf{P_D}/E_D = 0.02$. Using this value for β, γ is found to be, $\gamma = (1-0.02^2)^{-\frac{1}{2}} = 1.0002$, and so β and γ can be rounded to 0 and 1, meaning that the D^+ and D^{*+} frames of reference can be considered to be identical for the purpose of this calculation. The energies and momenta can now be inserted into equation 3, with the invariant mass range being given by the

minimum and maximum angles between the momenta of the μ^+ and the π^0. Thus, the kinematically allowed range of the invariant mass of the ($\mu^+\pi^0$) system is given by:

$$(E_{\pi^0} + E_\mu)^2 - (P_{\pi^0} + P_\mu)^2 < M^2_{(\mu^+\pi^0)} < (E_{\pi^0} + E_\mu)^2 - (P_{\pi^0} - P_\mu)^2$$

When the relevant energies and momenta are inserted into the above relation, we find: $(469.5 < M^2_{(\mu^+\pi^0)} < 601.8)\ MeV/c^2$. Using an analogous method, the range for the ($\pi^+\pi^0$) is found to be: $(464.3 < M^2_{(\pi^+\pi^0)} < 588.8)\ MeV/c^2$.

Bibliography

[1] J. L. Rosner, preprint arXiv:1002.1655v2 [hep-ex] (2010).

[2] K. Nakamura *et al.*, J. Phys. G **37**, 075021 (2010).

[3] *D. Griffiths, Introduction to Elementary Particles, Wiley-VCH (2008).*

[4] *F. Halzen and A. D. Martin, Quarks and Leptons, Wiley (1984).*

[5] B. I. Eisenstein *et al.*, Phys. Rev. D **78**, 052003 (2008).

[6] M. Kobayashi and T. Maskawa, Prog. Theor. Phys. **49**, 652 (1973).

[7] CKMfitter global fit results as of ICHEP 10, `http://ckmfitter.in2p3.fr//plots_ICHEP10/ckmEval_results_ICHEP10.html` (retrieved Sept. 2010).

[8] P. Colangelo and F. De Fazio and G. nardulli, Phys. Lett. B **372**, 331 (1996).

[9] G. Burdman and T. Goldman and D. Wyler, Phys. Rev. D **51**, 111 (1995).

[10] C. Lü, and G. Song, Phys. Lett. B **562**, 75 (2003).

[11] G. Sterman *et al.*, Rev. Mod. Phys. **67**, 157 (1995).

[12] K. G. Wilson, Phys. Rev. D **10**, 2445 (1974).

[13] E. Follana and C. T. H. Davies and G. P. Lepage and J. Shigemitsu, Phys. Rev. Lett. **100**, 062002 (2008).

[14] M. Artuso *et al.* (Cleo Collaboration), Phys. Rev. Lett. **99**, 071802 (2007).

[15] C. T H. Davies, preprint arXiv:1008.4018v1 [hep-lat] (2010).

[16] *J. F. Gunion and H. E. Haber and G. Kane and S. Dawson, The Higgs Hunter's Guide, Persius Publishing (1990).*

[17] A. G. Akeroyd and C. H. Chen, Phys. Rev. D **75**, 075004 (2007).

[18] B. A. Dobrescu and A. S. kronfeld, preprint arXiv:0803.0512v2 [hep-ph] (2008).

[19] *D. Perkins, Introduction to High Energy Physics, Cambridge University Press (2008).*

[20] J. L. Hewett, preprint arXiv:9505246v1 [hep-ph] (1995).

[21] A. Bazavov, preprint arXiv:0912.5221v1 [hep-lat] (2009).

[22] B. Blossier *et. al.*, preprint arXiv:0904.0954v2 [hep-lat] (2009).

[23] A. Ali Khan, Phys. Lett. B **652**, 150 (2007).

[24] T. Chiu *et al.*, Phys. Lett. B **624**, 31 (2005).

[25] L. Lellouch and C. lin, Phys. Rev. D **64**, 094501 (2001).

[26] D. Becirevic, Phys. Rev. D **60**, 074501 (1999).

[27] J. Bordes and J. Peñarrocha, preprint arXiv:0507241v1 [hep-ph] (2007).

[28] S. Narison, preprint arXiv:0202200v1 [hep-ph] (2002).

[29] A. M. Badalian and B. L. G. Bakker and Yu. A. Simonov, Phys. Rev. D **75**, 116001 (2007).

[30] C. W. Hwang, preprint arXiv:0910.0145v2 [hep-ph] (2009).

[31] M. Ablikim *et al.* (BES Collaboration), phys. lett. b **610**, 183 (2005).

[32] P. F. Harrison, ed. *et al.*, The BABAR physics book, SLAC-R-0504, 1997.

[33] B. Aubert *et al.* (*BABAR* Collaboration), Nucl. Instrum. Methods Phys. Res., Sect. A **479**, 1 (2002).

[34] M. Sullivan, B-Factory Interaction Region Design, SLAC-PUB-7563, (1997).

[35] Letter of intent for the study of CP violation and heavy flavour physics at PEP-ii, (*BABAR* Collaboration), SLAC Report SLAC-443, (1994).

[36] M. Andreotti, A barrel IFR instrumented with limited streamer tubes for BABAR experiment, SLAC-PUB-12205, (2005).

[37] Widhalm, L. et al. (Belle Collaboration), Phys. Rev. Lett. **100**, 241801 (2008).

[38] B. Aubert *et al.* (*BABAR* Collaboration), Phys. Rev. Lett. **98**, 141801 (2007).

[39] J. F. Benitez *et al.*, *BABAR* Analysis Document **2170**, Absolute Measurements of the Leptonic Branching Fractions $\mathcal{B}(d_s^+ \to \mu\nu)$, $\mathcal{B}(d_s^+ \to e\nu)$ and $\mathcal{B}(d_s^+ \to \tau\nu)$ Using Charm-Tagged Events and a Determination of $f_{D_s^+}$ (2010).

[40] P. Sanches *et al.*, preprint arXiv:1008.4080v2 [hep-ex] (2010).

[41] I. Narsky, Rare Leptonic Decays of the D Meson and Tau Lepton, Ph.D. Thesis, Southern Methodist University (2001).

[42] M. Chada *et. al.* (CLEO Collaboration), Phys. Rev. D **58**, 032002 (1998).

[43] I. Narsky, preprint arXiv:physics/0507157v1 [physics.data-an] (2005).

[44] Inventory of PidSelectors for ï24c; `http://www.slac.stanford.edu/BFROOT/www/Physics/Tools/Pid/Selectors/r24c/selectors.html` (retrieved sept. 2010).

[45] T. G. Dietterich and G. Bakiri, journal of artificial intelligence research **2**, 263 (1995).

[46] A. Gaz and K. Mishra and P. Ongmongkolkul and A. Telnov, *BABAR* Analysis Document **2199**, Particle Identification Using Error Correcting Output Code Multiclass Classifier (2009).

[47] BtaCandidate Lists, `http://www.slac.stanford.edu/BFROOT/www/doc/workbook/eventinfo/BtaCandInfo/CandLists.html` (retrieved Sept, 2010).

[48] A. Khan and K. Schofield and D. Wright, IEEE Nuclear Science Symposium Conference Record, Vol. 2, (2005).

[49] G. C. Fox and S. Wolfram, Phys. Rev. Lett. **41**, 1581 (1978).

[50] T. Sjostrand, preprint arXiv:9508391v1 [hep-ph] (1995).

[51] K. Flood and A. Telnov and C. Vuosalo, *BABAR* Analysis Document **1853**, Muon Identification Using Decision Trees (2010).

[52] A. Telnov, *BABAR* Analysis Document **1500**, Detailed Track-Level $\mathrm{d}e/\mathrm{d}x$ Calibration for the *BABAR* Drift Chamber and Silicon Vertex Tracker (2007).

[53] B. Aubert *et al.* (*BABAR* Collaboration), Phys. Rev. d **76**, 092004 (2007).

[54] M. T. Allen and M. T. Naisbit and A. Roodman, *BABAR* Analysis Document **870**, A Measurement of π^0 Efficiency Using $\tau \to \rho\nu$ and $\tau \to \pi\nu$ Decays (2004).

[55] Tracking Efficiency for Run 1 - Run 7 in R24, `http://www.slac.stanford.edu/BFROOT/www/Physics/TrackEfficTaskForce/TrackingTaskForce-2009-R24.html-Jun10-10` (retrieved sept. 2010).

[56] M. Artuso *et al.* (CLEO Collaboration), Phys. Rev. D **70**, 112001 (2004).

[57] B. Golob, preprint arXiv:1006.4208v1 [hep-ex] (2010).

[58] SuperB Collaboration, preprint arXiv:0709.0451v2 [hep-ex] (2007).